Alma Mater Studiorum - Università di Bologna

DOTTORATO DI RICERCA IN
AUTOMOTIVE PER UNA MOBILITÀ INTELLIGENTE

Ciclo 34

Settore Concorsuale: 01/B1 - INFORMATICA

Settore Scientifico Disciplinare: INF/01 - INFORMATICA

BIG DATA ANALYTICS FOR PROACTIVE AND PREDICTIVE MAINTENANCE IN ELECTRIC CAR BATTERY PACKS

Presentata da: Carlo Falcomer

Coordinatore Dottorato
Nicolò Cavina

Supervisore
Giovanni Pau

Esame finale anno 2022

Abstract

The idea behind the project is to develop a methodology for analyzing and developing techniques for the diagnosis and the prediction of the state of charge and health of lithium-ion batteries for automotive applications. For lithium-ion batteries, residual functionality is measured in terms of state of health; however, this value cannot be directly associated with a measurable value, so it must be estimated. The development of the algorithms is based on the identification of the causes of battery degradation, in order to model and predict the trend. Therefore, models have been developed that are able to predict the electrical, thermal and aging behavior. In addition to the model, it was necessary to develop algorithms capable of monitoring the state of the battery, online and offline. This was possible with the use of algorithms based on Kalman filters, which allow the estimation of the system status in real time. Through machine learning algorithms, which allow offline analysis of battery deterioration using a statistical approach, it is possible to analyze information from the entire fleet of vehicles. Both systems work in synergy in order to achieve the best performance. Validation was performed with laboratory tests on different batteries and under different conditions. The development of the model allowed to reduce the time of the experimental tests. Some specific phenomena were tested in the laboratory, and the other cases were artificially generated.

Contents

List of Figures

Introduction

Motivation

One of the causes of climate change is certainly to be found in mobility. An alternative to traditional diesel and gasoline engines is certainly the use of other fuels such as LPG and methane, which allow to reduce CO2 emissions; however, currently the only way to bring to zero such emissions is represented by electric mobility. The electric car market is increasing year after year, with record sales all over the world, thanks to the awareness of the various aspects of environmental protection and thanks to an aggressive campaign of incentives.

Today we are witnessing a global diffusion of applications based on the use of Li-Ion batteries; for many of them the life cycle of the device is limited by the life of the battery, as we can see in portable devices such as cell phones or computers. In the case of electric vehicles, reaching 80% of nominal capacity is to be considered the end of battery life, however the battery can still be used on stationary applications where such high energy density is not required. For this reason, it is important to have a Battery Management System (BMS) that can monitor the battery, to extend its life as much as possible, and that can estimate its status accurately, so that it can be reused in other applications.

An electric vehicle usually has an installed energy of tens of kWh (they can also reach hundreds of kWh), to reach such high energy values while maintaining the weight and volume contained, the current technology is based on lithium. Currently the cell format that guarantees the highest value of energy density is the cylindrical format. The most common formats are, 18650, (18 mm radius) and (65 mm height), and 21700, (21 mm

radius) and (70 mm height), the latter being the most recent format that in the next years.

Cylindrical cells, despite reaching energy densities of 250 Wh/kg, have low energy values per cell, around 12 Wh for 18650 and 18 Wh for 21700.

This immediately highlights the problem: the number of cells required by a battery pack exceeds thousands. The Tesla model S 75kWh, for example, has approximately 7000 cells. An aspect to be taken into consideration is certainly related to the safety of these vehicles, it is especially due to the great reactivity of lithium.

There is a Safety Operation Area (SOA), defined by the manufacturer, within which the battery pack must work. If the battery works out of this area of operation, irreversible processes of degradation are triggered, leading to a decrease in reliability and power availability; in the worst cases, fires or even explosions can occur. The BMS is a system present in every battery pack composed of lithium cells and is responsible for monitoring the battery to ensure proper operation and prevent possible malfunctions. The BMS, therefore, plays a key role in ensuring a good level of safety, also allowing to maximize battery performance.

Original Contribute

Considering the aspects reported above, the purpose of this work is to develop a BMS functionality capable of monitoring the battery working zone, to keep it in the SOA. At the same time, the BMS will evaluate the state of the battery in terms of State of Charge (SOC), State of Health (SOH), etc.

The existing literature provides important results regarding the estimation of battery states, however most of them regard *SOC*. In contrast, for *SOH* there is little information about it and, currently, there is no single definition. The objective of this work is to analyze different algorithms to estimate *SOH*, based on the internal resistance of the cell. *SOH* is among the most important parameters to monitor in lithium-ion batteries (LIBs) because it serves to know their residual functionality of the battery.

In addition to the state estimation, another fundamental aspect to ensure the maximization of a battery performance is related to the modelling; being able to have an accurate

model of the battery, in fact, allows to analyze its behavior in every possible operating condition, challenging it to the limit of its potentiality.

The Equivalent Electrical Circuit Model (ECM) allows to obtain excellent performance while maintaining reduced complexity with concentrated parameters. The thesis will illustrate the most popular models in the literature, aiming to analyze the methods to obtain the parameters starting from experimental tests, also using ad hoc tests developed over the years. The models developed will be compared with data from laboratory tests to verify the validity in various configurations.

Thesis Outline

Chapter 1 contains a general introduction on the state of the art, starting with a quick description of the context in which this work is inserted and briefly describing the issue of electric mobility. In the following paragraphs, LIBs and the differences between the various batteries on the market will be introduced, and finally the BMS will be analyzed, describing its main functions. Subsequently, the topic of battery modelling will be introduced, leaving to the next chapter a more detailed discussion and the description of the models most used in the literature. In the last two paragraphs, the possible states that can be identified for a battery will be described, presenting the most common methodologies for their determination.

Chapter 2 will go into the details of battery modelling, starting with a description of the test system that has been used for the realization of laboratory tests. The second paragraph will explain in detail how it is possible to derive the parameters of the equivalent electrical model starting from the laboratory tests. These same parameters will then be used in the following paragraphs for the realization of the battery model. In this chapter, three possible implementations will be presented that have been realized for three dissimilar purposes, in three different programming environments. The results obtained in comparison with real tests will then be examined.

Chapter 3 will describe the methods investigated over the years for parameter estimation. An introduction of the theory behind each method will be made, and then the

application to the battery world will be shown.

Finally, the results of the comparison between the tests and the model analyzed in the previous chapter will be presented. In this chapter a lot of space will be dedicated to the estimation methods based on Kalman Filters, as they have shown excellent effectiveness in estimating the state of the battery, therefore being recognized in the literature as the state of the art for the *SOC* estimation.

1 State of The Art

1.1 Electric Mobility

Climate change is a central topic nowadays and among the points of the 2030 agenda of the European Commission there is the fight against climate change. The transition to more sustainable technologies can not only help to solve the problem of climate change, but also allow to reduce polluting emissions and thus improve the quality of life of people already in the short term. In this ambitious program, mobility plays a fundamental role; in fact, a large part of pollution is caused by the transport of goods and people. In Emilia-Romagna 41% of CO2 emissions are produced by road transport.

Thanks to recent regulations, registered thermal vehicles must comply with increasingly stringent constraints on pollutant emissions. The transition to zero-emission vehicles can also take place using vehicles powered by fuels with a lower environmental impact, such as LPG and methane gas, although, due to their very nature, emissions can never be equal to 0. For this reason, the transition to electric vehicles is currently the only solution. Market forecasts indicate that electric vehicles are becoming more and more widespread; it is estimated that they could cover 30% of the car market in 2030 [16].

Electric mobility uses one or more electric motors for propulsion, energy is stored on board in a variety of ways, the most common being: Hydrogen tanks, the hydrogen being then converted through fuel-cells into electricity, and batteries, which store chemical energy, which is converted back into electricity through chemical reactions and then used by the engines. Currently, electric mobility is spreading across all sectors [2]. Starting with micro-mobility, i.e., those low-weight vehicles used for small trips such as bicycles,

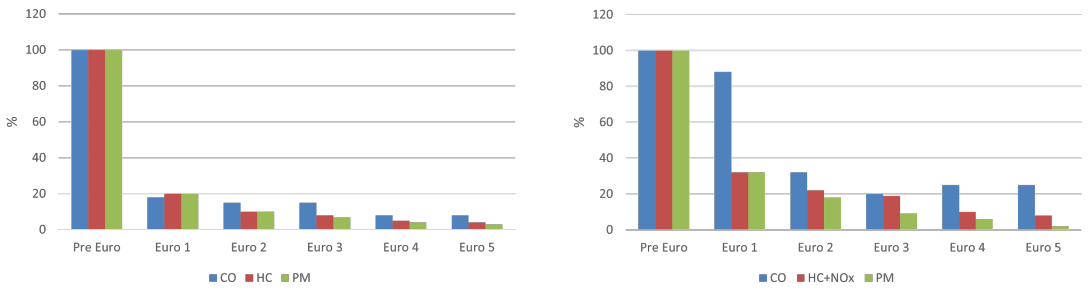

(a) (b)

Figure 1.1: Emission values imposed by regulations depending on the "Euro" class of registration, gasoline (a), diesel (b)

Figure 1.2: Citymood 12e Electric bus, developed by Industria italiana autobus, presented on November 29

scooters, and electric scooters. In private mobility, electric cars are becoming increasingly popular with a massive increase in recent years, also thanks to incentives proposed by the state and regions.

The focus has also been on sustainable public transport, where, for example, the Emilia Romagna region has recently presented the new "Citymood 12e electric bus Fig. 1.2", [5]. Electric motors can be coupled to traditional internal combustion engines, where it is not possible to support the demand for power and energy as in the case of agriculture [6].

The choice to use electric mobility is linked to the best use of energy, considering that in traditional internal combustion vehicle, 84% of the energy used is dispersed in the form

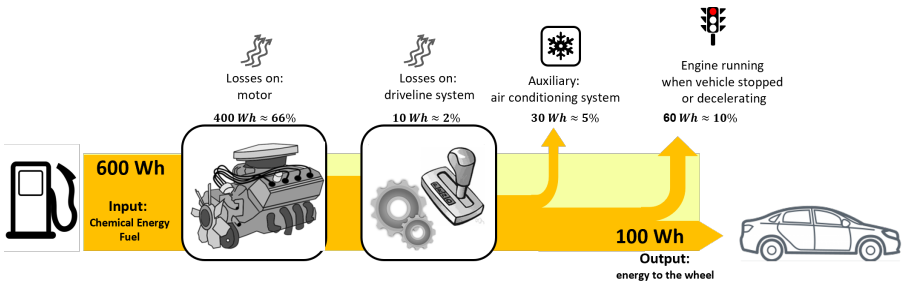

(a)

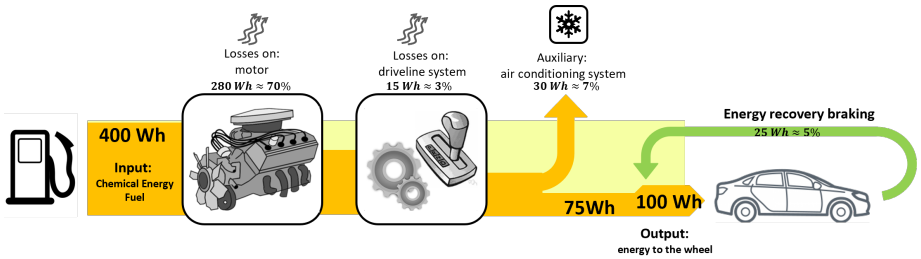

(b)

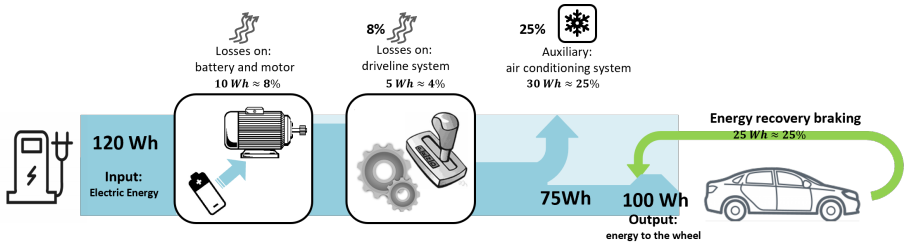

(c)

Figure 1.3: Comparison of the efficiency of various vehicles, (a) internal combustion engine (ICE), (b) hybrid electric vehicle (HEV), (c) battery electric vehicle (BEV)

of heat, consequently only 16% is used to propel the vehicle. For electric vehicles the efficiency is much higher and 83% of the energy is converted into motion. In Fig. 1.3, the waste contributions broken down by vehicle type are shown.

The high efficiency of electric vehicles can be attributed to the absence of an internal combustion engine, which by its very nature has a very low efficiency, but is also linked to the possibility of recovering energy when braking and to the practically zero consumption in stationary phases of driving, such as, for example, at traffic lights.

Despite the advantages of the transition to electric vehicles, this transition it is not taking place rapidly, the cause of which is to be found in various factors that limit its

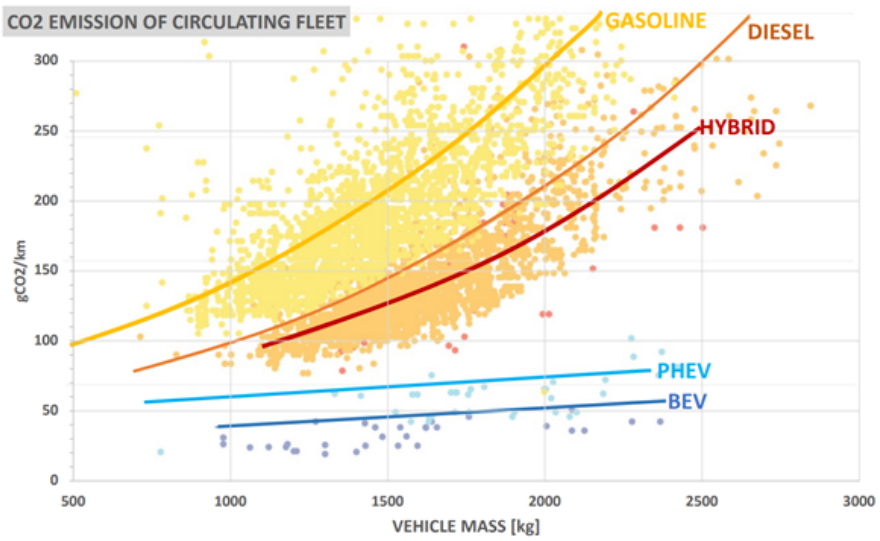

Figure 1.5: Comparison of CO2 emissions by vehicle type, with reference to mass

diffusion.

Electric vehicles, unlike traditional vehicles, can store less energy on board, due to their low energy density; in fact, the energy density of gasoline is ten times greater than that of batteries, and this has repercussions on a shorter range. Recharging times are also different: to fill the tank of a thermal vehicle can take approximately 5 minutes, to recharge a battery vehicle can take more than 2 h.

For this reason, the transition must also take place through a change in the mentality of users, and this must affect the use of vehicles that require a smaller amount of energy to move.

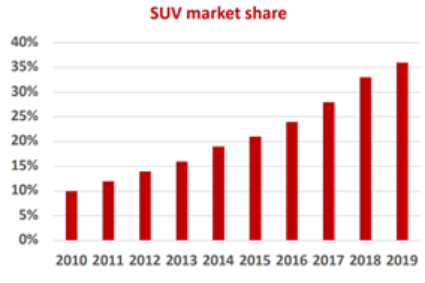

Figure 1.4: SUV Market share

The market, however, shows an opposite trend, with an inincreasing diffusion of "SUVs", the vehicles with a high mass. The graph in Fig. 1.4 shows that the number of these vehicles has tripled, from 10% in 2010 to 35% in 2019. The increase in the mass of these vehicles increases consumption and consequently has a huge impact on the increase in emissions. In Fig. 1.5 you can see as the increase of vehicle mass affects CO2 emissions.

It can also be seen that this trend is less pronounced for electric vehicles, which, thanks

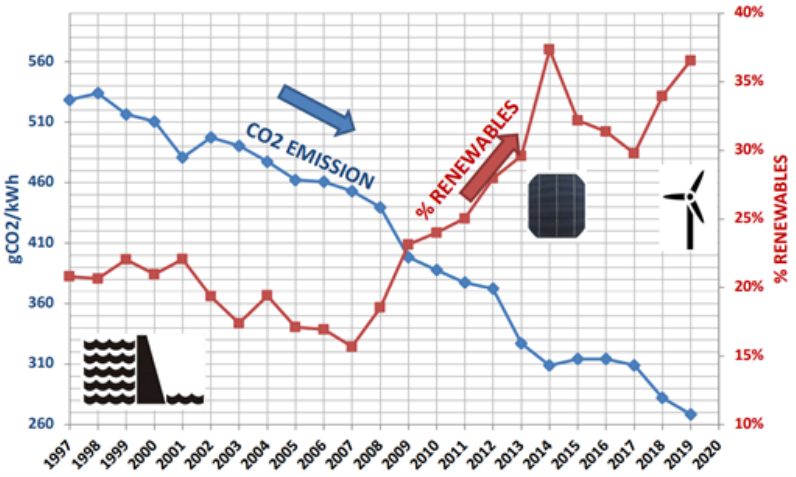

Figure 1.6: Trend of energy production from renewable resources in Italy, trend of corresponding CO2 emissions

to recovery during braking, are able to disperse less energy. A further aspect related to the high consumption by vehicles is to be attributed to the speed: in fact reducing speed from 130 Kph to 120 kph leads to 14% consumption reduction. What has been said shows how the transition towards BEVs or PHEVs can only take place with a change in the mentality of users. The last aspect that limits the diffusion of electric vehicles is their high cost if compared to the cost of traditional vehicles.

Talking about electric mobility it is necessary to analyze the way in which the energy that is used in vehicles is produced. Europe is still a long way from achieving climate neutrality Fig. 1.8, [4]. In Italy, the production of energy from renewable sources is growing and currently stands at around 35%. However, in Italy a lot of energy is generated using natural gas, which produces high values of CO2. Moreover, due to the nature of renewable sources, they are not constant over time, and therefore energy storage systems are necessary, in order to meet the energy needs when renewable sources are not sufficient.

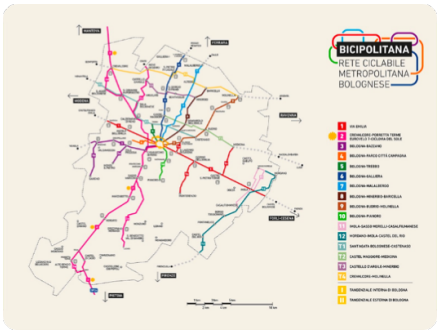

Figure 1.7: Bike lanes in the city of Bologna

The investments being made to combat climate change are having enormous results.

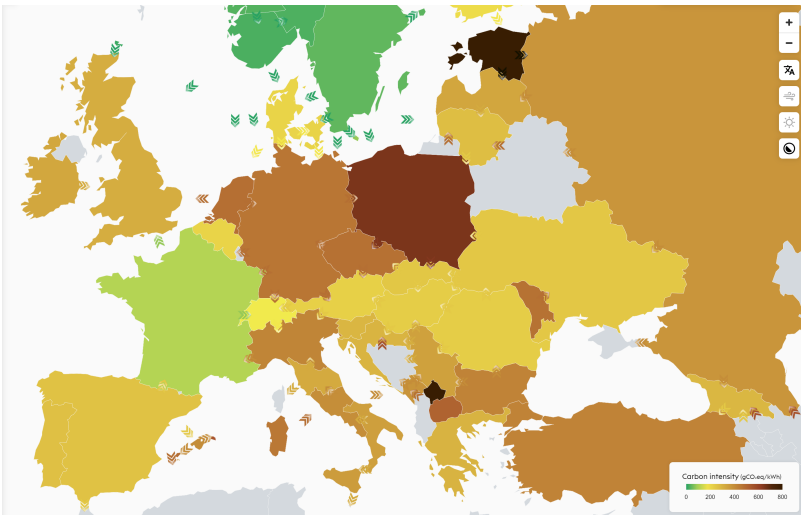

Figure 1.8: CO2 emissions by used energy, divided by states, [4]

In the city of Bologna, 500 km of cycle paths have already been created to encourage the use of more sustainable vehicles such as bicycles and scooters.

The recharging infrastructure is expanding enormously, and more and more parking spaces are being reserved for recharging electric cars.

Finally, more and more is going to be invested in research on higher performance batteries, given the great demand for electric vehicles and their greater autonomy. Currently, batteries with an energy density of 280 Wh/kg can be found at a price that is more and more decreasing.

1.2 Lithium Ion Battery

In this section will analyze some of the main characteristics of the batteries that are commonly used. The first part will introduce the principle of operation of the battery in general, the second will discuss the formats in which batteries can be found, and in the last part will be shown a comparison between the various types of lithium-based chemicals in the market.

1.2.1 History of Battery

Research in lithium batteries began in 1912 under G.N. Lewis, but the breakthrough came in 1958 when Harris noticed the stability of Li-metal in several non-aqueous electrolytes such as fused salts. The formation of a passivation layer that prevents the direct chemical reaction between lithium metal and the electrolyte but still allows for ionic transport is at the origin of the stability of lithium batteries [38].

This type of batteries uses electrode materials intercalation which allow to accumulate and release lithium ions, in a reversible process. This phenomenon is defined as host-guest, the electrode structures accepting lithium ions inside and then releasing them at the next cycle to the other electrode. The components of the electrodes must be good electrical conductors, and good ionic conductors.

Although initially batteries were produced with cathodes composed of an acceptor material of Li ions and an anode of lithium metal, the use of the latter was later abandoned, as the high reactivity of Lithium provoked very intense corrosive phenomena at the interface causing both the degradation of the device and safety problems, up to extreme cases of self-combustion of batteries. For this reason, lithium-ion batteries were introduced to overcome the safety issues carried by lithium metal batteries.

The major components of LIBs are the negative and positive electrodes, electrolyte, and separator Fig. 1.9. The negative and positive electrodes correspond to the anode and cathode, respectively, during discharge, and vice-versa in charge phase.

To avoid contact between the electrodes, which could produce very violent reactions, a membrane is interposed to act as a separator. The separator allows the passage of ions

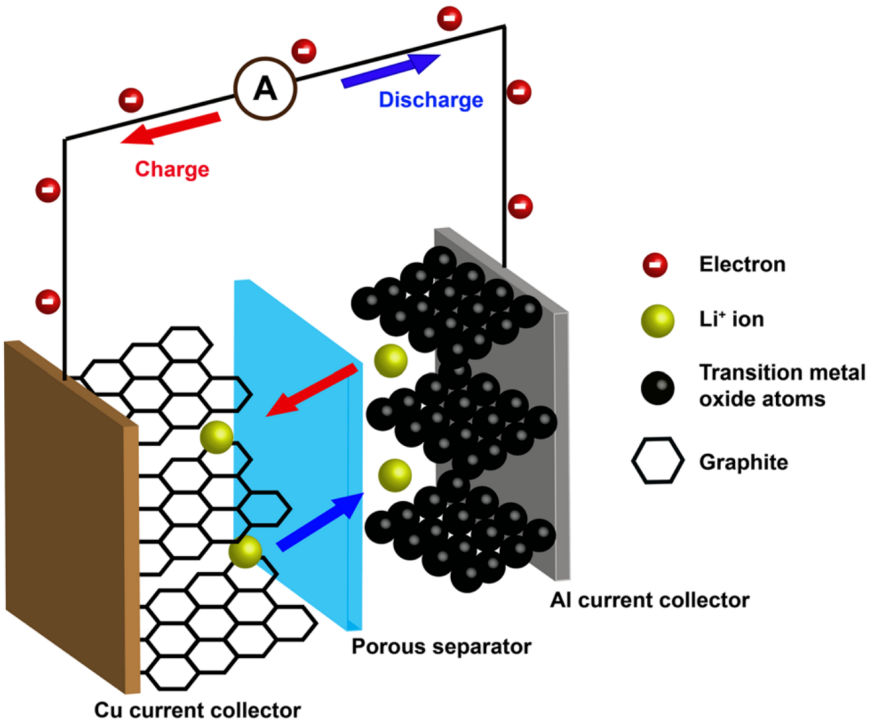

Figure 1.9: Major components and operating mechanism of LiBs

but prevents electrical contact.

The cathodes are typically oxides of Mn, Ni and Co, thanks to the crystalline structure make easily insert the lithium ions. For the anode is widely used graphite together with lithium titanates deposited on copper foil. The layered structure of graphite is composed of strongly bound atoms and arranged in hexagonal structures with the various planes held together by weaker bonds.

For safety reason, aqueous electrolytes are not usable, so organic solvent are used. Due to a high potentials stability the battery can operate in high voltage ranges During the first charge, the electrolyte decomposes, a passivation film is so created in the anode-electrolyte interface. This thin layer is insulating for electrons but very conductive for ions. This layer is called Solid Electrolyte Interface (SEI). The SEI prevents the formation of the dendrites structure, which would lead to damage of the separator, and subsequently make short circuit between the electrodes.

During discharge when the battery is connected to a load, as shown in Fig. 1.9, lithium

ions are deintercalated from the negative electrode, flowing into the electrolyte through a separator due to the diffusion and migration processes. Finally intercalated into the positive electrode. The process is reversed during charging [39].

The materials used for electrodes are typically:

- materials with a lamellar structure;
- materials with interstitial sites, where the ions can stay;
- amorphous materials.

1.2.2 Type of battery

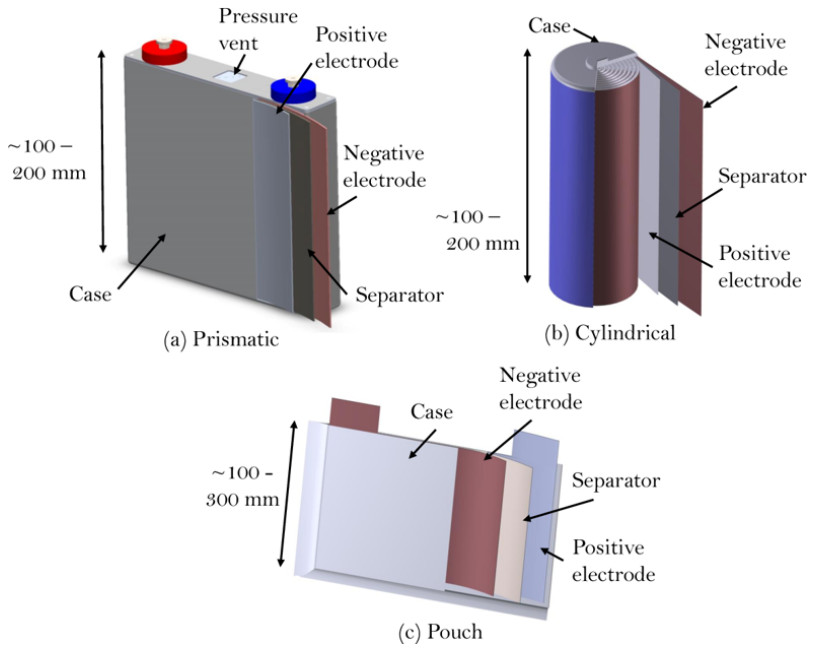

Figure 1.10: Comparison between different type of cell

Lithium-ion cells are available in 3 formats, prismatic, cylindrical and pouch Fig. 1.10, each format has its pros and cons. The cylindrical format reduces the expansion effects due to chemical reactions, but the integration process is complicated. The prismatic format, on the other hand, makes the integration process much easier, but it is the format that presents the lowest energy density for the same chemistry. There are many parameters to consider

when choosing the chemistry of a cell. The following are the characteristics of the most common cells, with a brief description of each.

Prismatic The prismatic format Fig. 1.10(a) allows for easy integration and optimal use of space. Also, for this type of cell there is a vent valve for the gases produced inside.

There are multiple sizes of these cells, to be used in different applications a big advantage for this format is the presence of the screw connectors for the poles, which make integration much easier. However also because of the external housing these cells have a low specific density. However, they are also used in electric vehicles as they have higher capacities and nominal energies than the cylindrical format.

Cylindrical Is the most widely used format Fig. 1.10(b). The cylindrical design has advantages from a constructional point of view as it is easy to manufacture and has mechanical stability, since the cylindrical shape can withstand high pressure. However, due to its nature, there is a loss of space in the integration and consequently battery packs composed of these cells have a large volumetric footprint. A further disadvantage of this format is due to the low capacity of the cell, and consequently the number of elements to be integrated is much higher than with other types.

Many cylindrical cells have a device that can release the pressure generated inside, so as not to trigger explosions.

Cylindrical cells are mainly used for power tools, electric bicycles. This format is used by Tesla for some of its vehicles. The most common format is 18650, but currently other formats such as 21700 are gaining ground, thanks to a higher energy rating. Tesla currently plans to produce its own cylindrical format 46800, with the aim of reducing the cost of production and integration.

Pouch These cells Fig. 1.10(c) are made with conductive layers to which electrodes are soldered. The integration of these cells is a middle ground between prismatic and cylindrical formats, in fact they have nominal energies like cylindrical cells, and require a soldering process, but they can be stacked without loss of space like prismatic cells, also they need to be kept under pressure to avoid swelling during use. This type of cell

together with the cylindrical cell are the ones with the highest specific energy density, and the highest specific power density. On the other hand, these cells have a strong swelling effect mainly during the recharge phases, due to the gas that is produced inside the cell, which can cause a delamination of the layers and therefore a loss of capacity. A further disadvantage is the low mechanical stiffness, so the design of the external case must be more robust than other formats.

As for the prismatic cells the format is not standard, but it is made to measure of the application. Typically, these cells are used in model aircraft or drones due to their high power density, and high currents they can deliver. This type of cell is also used in electric vehicles, especially in hybrid vehicles where the currents are high.

1.2.3 Battery Chemistry

Table 1.1: Comparative table of different types of lithium batteries

Name	Positive eletrcode	Negative eletrcode	Nominal voltage [V]	Energy density		Cycle	Thermal stability	Thermal runaway [°C]
				Gravimetric [Wh/kg]	Volumetric [Wh/l]			
ICR-LCO	LiCoO2	Grafite	3,7	150-200	420	500-1000	Low	150
IMR-LMO	LiMn2O4	Grafite	3,9	100-150	350	300-700	Good	265
INR-NMC	LiNiMnCo2O2	Grafite	3,6	205-250	580	500-2000	Good	210
NCA	LiNiCoAlO2	Grafite	3,6	220-260	600	500	Good	160
IFR-LFP	LiFePO4	Grafite	3,2	90-130	330	1000-2000	Excellent	310
LTO	LiMn2O4-LiNiCoAlO2	Li2TiO3	2.4	50-80	180	3000-7000	Excellent	

LCO Lithium-Cobalt

Their high specific energy makes them the most common choice for consumer electronics. The disadvantage of this type is a relatively short lifetime, low thermal stability, and limited load capacity (low specific power). LCO's, due to poor thermal stability, are not to perform charge-discharge cycles at currents higher than their C-rating.

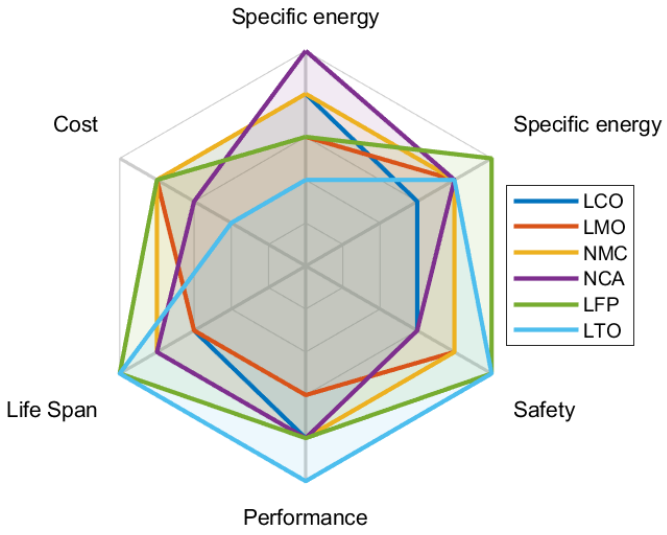

Figure 1.11: Battery Chemistry Comparison

IMR-LMO Lithium-Manganese

The architecture forms a structure called "three-dimensional spinel structure" which allows to improve the ionic flux on the electrode. This leads to lower internal resistance and to easier thermal management. The structure offers high thermal stability and therefore a greater safety, allowing to perform charge and discharge cycles with high C-rates while maintaining low temperatures. The disadvantages of this type of cells are a reduced number of cycle and a low specific energy value.

INR-NMC Lithium-Nickel-Manganese-Cobalt

One of the most successful lithium-ion systems is the cathodic combination of nickel manganese and cobalt. Like LMOs, this cell type can be used as either a "High Energy" and "High Power" cells. The combination of these elements, produces the strength of LCO and LMO; in fact, nickel is known for its high specific energy density but has poor thermal stability, while manganese has the advantage of having a structure with low internal resistance but a low specific energy. The cathode combination is typically one-third nickel,

a third manganese and a third cobalt. Since the three elements are easily combined these batteries can be adapted to a wide range of automotive and energy storage applications that require a high number of cycles.

NCA Lithium-Nickel-Aluminium-Cobalt

This cell type shares similarities with NCM but without the benefit of manganese. They tend to withstand lower discharge currents but compensate by offering high specific energy and reasonably good power. The addition of aluminum gives the chemistry greater stability. The disadvantages are certainly a high cost and a poor safety.

LFP Lithium-Iron-Phosphate

Lithium phosphate offers good electrochemical performance with low resistance, allowing high currents and a very high number of cycles, good thermal stability, and therefore greater safety. As a compromise, it has a lower nominal voltage compared to other chemistry, lower specific energy compared to LCOs, and present a higher self-discharge rate which causes equalization problems.

LTO - Lithium Titanate

The lithium titanate anode replaces the graphite anode of a typical lithium-ion cell. The cathode can be either LMO or NCM type. LTO cells have a nominal voltage of about of 2.4 V, can be charged quickly and provide a high discharge current over a wide temperature range. This type of cells has excellent characteristics of durability, safety, and power. However, they are very expensive and have a low specific energy density.

1.2.4 Ageing Phenomena

Aging in a battery is a physical-chemical decay involving the different components of the cell: electrodes, electrolyte, collectors, additives. This leads to a decrease in battery capacity and maximum available power. The main degradation mechanisms involve the electrodes and are different from each other over time. Aging leads to a change in struc-

tural properties, a change in available active material caused by dissolution of the material in the electrolyte. Most negative electrodes use graphite, carbon, or titanate. Graphite is the most widely used because of its better characteristics, particularly about safety, as shown in Tab. 1.1. The main mechanism to consider is related to the formation of Solid Electrolyte Interface (SEI) on the graphite negative electrode [53]. This solid interface is formed when the battery is first charged, and its purpose is to protect the electrode from possible corrosive effects and to avoid electrolyte reduction. This phenomenon occurs mainly at the beginning of the cycle and changes with time, causing a continuous loss of lithium ions and a decomposition of the electrolyte. In the short term this does not lead to a large loss of capacity, but over time it leads to a decrease in the active time and to a decrease of active surface, increasing the electrode impedance. The positive electrode is subject to low alterations in time, leading to the formation of SEI, which is more difficult to detect given the high voltages present on this electrode.

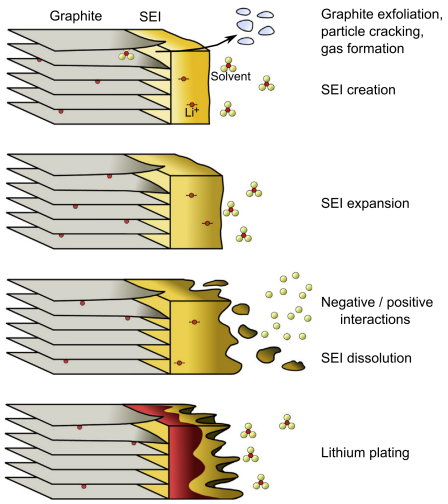

Figure 1.12: Illustration of ageing effects on battery negative electrode: the capacity fade and the SEI growth [53]

These phenomena occur both with the battery in use and with the battery at rest and there is an influence of the state of charge. In fact, a high *SOC* (>80%) can cause an acceleration of this phenomenon given the high potential difference between the electrode surface and the electrolyte. In addition, other factors such as high temperatures, overcharging or short circuits aggravate the process. At high temperatures the SEI can dissolve and create less permeable lithium ions by increasing the impedance of the negative electrode. Conversely, low temperatures lead to a decrease in lithium diffusion between SEI and graphite, which can lead to the formation of lithium plaques, causing a loss of battery capacity. In the worst cases the SEI can perforate the insulation between the two electrodes creating an internal short circuit, which inevitably leads to cell rupture. The consequences of aging can be identified in loss of capacity and increase of

internal impedance. Both phenomena have chemical causes but with different origins.

The consequences of these mechanisms in lithium-ion cells are:

- The decrease in available lithium over the various cycles increases the cell imbalance, and this occurs on both electrodes due to the formation of SEI by the decomposition of the electrolyte;
- The loss of active material on the electrode resulting in delamination;
- Increased cell resistance due to the formation of passive films on the active surface.

Battery aging can be divided into two processes: one type of deterioration by calendar and one due to duty cycles. The former corresponds to a situation in which the battery is in a state of storage without being used, while the latter describes the consequences of several charge and discharge cycles [47].

Calendar aging

Thus, calendar aging results in a loss of capacity that can be rapid depending on the conditions under which the battery is being stored. The main cause of an accelerated self-discharge is the temperature at which the battery operates. In fact, at high temperatures secondary phenomena such as internal corrosion or loss of active lithium are facilitated.

It is necessary, however, a compromise from the point of view of temperatures since even too low temperatures limit the diffusion. The other aspect affecting calendar aging occurs in the case of several cells connected in series, in case of different *SOC* between the various cells, even at moderate temperatures different aging phenomena occur.

The *SOC* represents the proportion of ions present on the electrodes. This means that for high levels of *SOC* there will be a large potential imbalance at the electrode-electrolyte interface. Most studies on the calendar life of batteries see *SOC* as dependent on the temperatures during storage. These quantities result in a nonlinear alteration of the capacity and resistance

Working cycle aging

Cycle aging happens when the battery is being charged or discharged. Temperature and current at which battery are used play a central role in this type of aging.

In addition to these factors, the ΔSOC, which represents the change in discharge during the cycle is also critical and influences the health of the battery. Studies conducted by Bloom et. al. [76] show a loss of deliverable energy from the battery for high ΔSOC levels.

This phenomenon is mainly caused by degradation at the positive electrode and SEI formation enhanced by discharges and charges. Another factor that affects aging is the voltage range at which the cell is operated. Exceeding the range declared by the manufacturer causes a greater deterioration of the cell; for example, discharging a battery at a voltage of 0.1 V lower than that provided by the manufacturer, halves the life of the cell. This phenomenon greatly affects the life of the cell, is bringing much more critical aging than an increase in operating temperature of $15°C$ [53].

1.3 BMS

In industrial applications, a single cell cannot provide adequate power for the application. Therefore, it is necessary to connect several cells in series and parallel to each other to create a battery that is industrially useful. However, the realization of a battery composed of many elements, usually in the order of thousands for electric vehicles, brings with it many critical issues. Consequently, it is necessary to use a device that monitors the various elements to ensure proper operation, this type of device is called battery management system (BMS) [40]. Currently, there is still no unanimous consensus on the final definition of BMS and what BMS does. According to [8], the BMS is the device that takes care and manages the battery.

The BMS is composed of mechanical and electronic components and can be either software or hardware, while the battery can be a single cell, a battery module or a battery pack [55].

The BMS has the task of monitoring parameters such as voltage, current and temperature of the individual cells and ensure that they remain within the range provided by the manufacturer.

For electric vehicles the cost of the battery contributes about 50% of the vehicle, for this reason, to lower costs typically BMS systems are made with cheap microprocessors and limited computational power. This therefore reduces the possibility of using powerful algorithms on the vehicle, but sometime the calculations are decentralized on the cloud, with edge computing architectures based.

1.3.1 BMS architecture

Usually BMS systems are very complex, and are replaced by many subsystems that cooperate with each other. The architecture of the BMS can be of different types: a concentrated architecture with a single BMS that controls the entire battery pack, or a distributed one, with more elements that take the name of slave, and only one master. The single-element architecture is popular for low-power applications, or in general where the number of cells in series is small. The Master-Slave architecture is the one used in vehicles.

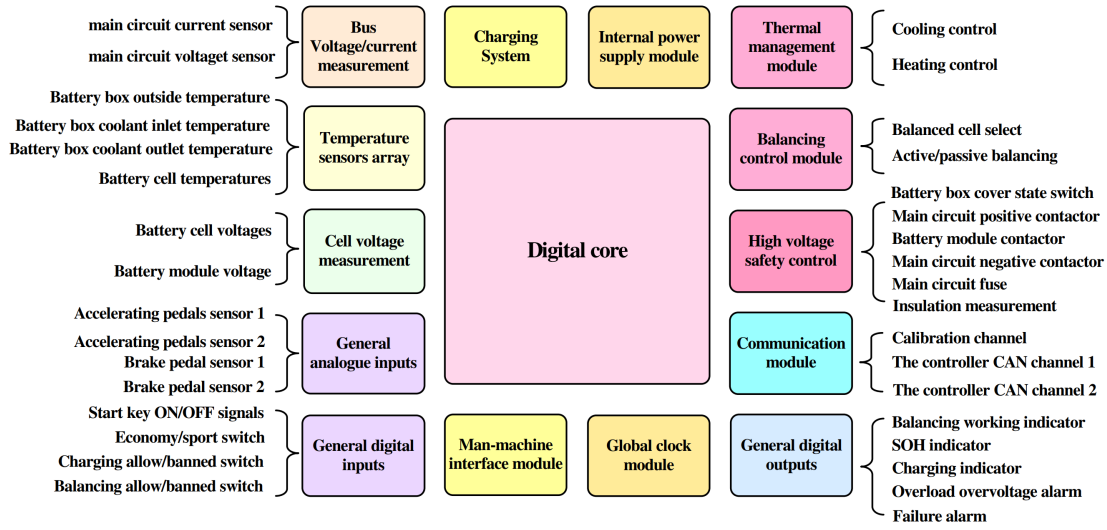

Figure 1.13: Basic framework of software and hardware of BMS in vehicle [55]

In the Master-Slave architecture, each slave is responsible for acquiring information only related to a subset of cells that takes the name of the module, then communicates it to the Master. The single slave is responsible for the equalization of its cells. The Master on the other hand collects all information received from the Slaves and takes care of the actual management of the battery pack and then communicates to each slave the information related to equalization. An example of this architecture is shown in Fig. 1.14.

When the number of integrated cells and modules grows, it may be appropriate to create multiple layers. This has been done within the LIBER project. In the LIBER battery pack Fig. 1.15, there are several "Bricks" composed by a fixed number of cells, and they are monitored by a BMS that is called "BMS-Brick".

The Brick are then connected in series between them to form a module. The "BMS-Module" is responsible for receiving information from the Brick and monitor all the elements in the module. Modules are connected to form a package, the "BMS-Pack", interfaces only with the "BMS-Module", and manage it as if they were individual cells connected in series.

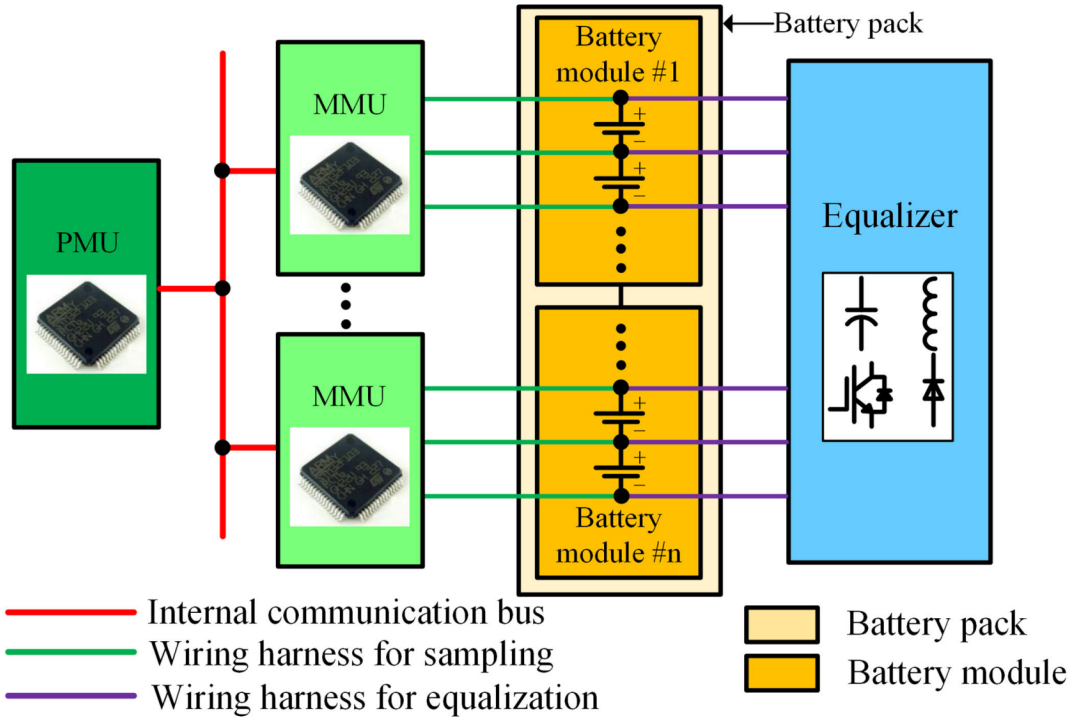

Figure 1.14: Structure of a two-level conventional BMS [20]

1.3.2 Data I/O

The BMS has inputs, which can be either analog or digital signals. Analog such as: current, voltage and temperature. Current sensor to measure the current of the battery pack, voltage sensor to measure the voltage of the cells connected in series, temperature sensors to measure the temperature of the cells, the ambient temperature, and if liquid cooling is installed, also the temperature of the liquid at the inlet and outlet of the pack.

Digital sensors such as sensors for power relay status, equalization status, or charging status. It is necessary to measure the voltage of each element connected in series, while for current, unless there are more modules connected in parallel, only one measurement is needed. For the temperature measurement there are more methodologies that are currently adopted, the most widely used is the spot measurement, which consists of measuring the temperature in particular areas of the battery pack, typically the most critical ones. In these years it is being developed a project within the LEMAD laboratory, in which the temperature is measured in each element, which constitutes the battery pack, and is measured the

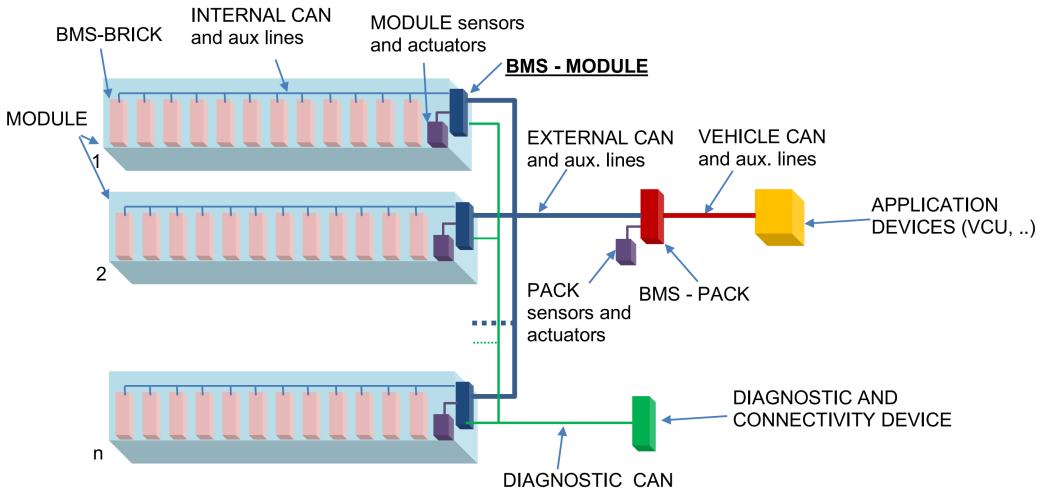

Figure 1.15: LiBER BMS, Multiple modules battery pack configuration

temperature on both poles.

Depending on the measured quantity, the sampling frequency is different so as not to over-sample variables that vary at a low frequency such as temperature, leading to a waste of BMS resources. Voltage and current are sampled with high frequencies, in range of kHz, while temperature can be sampled with frequencies in range of Hz.

The accuracy of the voltage measurement must be as high as possible, typically around mV, which is achieved with the use of low-cost sensors available on the market. The temperature measurement is easy, and a high accuracy is not always a requirement: typical value is around $1°C$. The current measurement is more complicated, for BEV applications, where the current is more than hundreds of Amperes, the task is more difficult, and hall effect sensors are used. Sometimes more than one current sensor can be used at the same time, with different full scales so it is possible to decide which one to use depending on the current value.

The BMS can have digital or PWM output: digital type, such as the command to close or open the power relay, or the equalization control, while the PWM outputs, can be used for thermal management to heat or cool the battery, or to give visual indications to the user, such as charging indication.

Usually, the BMS is also equipped with a real time clock.

1.3.3 BMS Functionality

Battery Protection

The protection functions are used to ensure that the limits provided by the manufacturer are respected. The limits provided by the manufacturer specify a work area within which the battery must work, it is defined as Safety Operation Area (SOA). The BMS therefore compares the values set with those measured, and if the SOA is exited, the BMS must warn the user to re-enter the safety zone. Typically, CAN-Bus protocol is the used protocol between the BMS and the battery user.

State estimation

This includes State of Charge (*SOC*) or Depth of Discharge (*DOD*), State of Health (*SOH*), etc.. For the definition of these state indicators, refer to chapter 1.5.

Battery Control Charge

The battery charger controller is the part of the BMS software in charge to manage the charging phase, this process is very delicate and allows to optimize the charging process. The most common method is called Constant Current Constant Voltage (CC-CV) shown in Fig. 1.16, which allows to reduce recharge times, remaining within the SOA. This charging process is divided into two areas, the first at constant current, in which the voltage of the pack increases, while in the second at constant voltage, the current is decreased to keep the voltage constant so as not to exceed the battery limit values.

Battery Equalization

Since the cells are not all identical, there can be differences that cause different voltages during use.

This phenomenon leads to a non-optimal use of the battery. In the charging phase, the cell with the higher voltage will stop charging, and consequently the battery can no longer store the maximum energy. In the discharge phase, the cell with the lower voltage causes

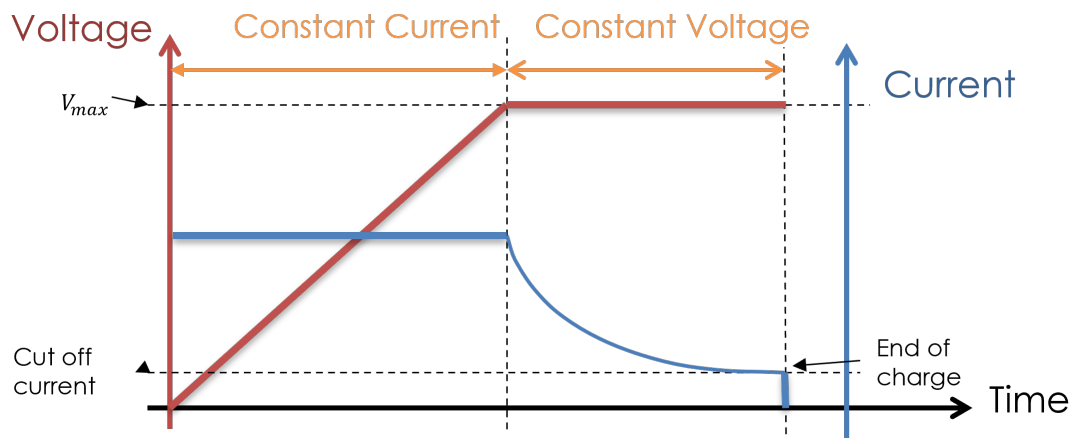

Figure 1.16: Typical charging curve

the interruption of the discharge, and consequently all the energy stored inside the battery cannot be used.

To bring the cells back to the same voltage the battery must be equalized. There are two different categories of equalization, active and passive equalization.

Passive equalization, Fig. 1.17(a) consists in discharging the most charged cell, through an external circuit, on a resistance. The discharge will be faster the lower the resistance value will be. This type is the most used thanks to its simplicity of integration, however it is a process that wastes energy in the battery.

Active equalization, Fig. 1.17(b) on the other hand, allows energy to be transferred from the most charged cells to the most discharged cells, so there is no energy loss. However, this type is the one that presents a greater complexity, and consequently is rarely used. Passive equalization, by its nature is activated only during the charging process. The BMS activates the equalization command, going to close a switch to insert in parallel to the cell the equalization resistance R_{eq}. The equalization resistor cannot be as low as desired because the currents that would be flowing would grow enormously, and consequently the power to be dissipated, would be too high.

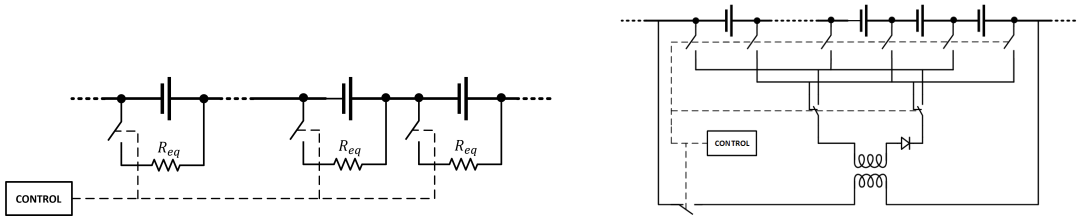

(a) Passive equalization scheme (b) Active equalization scheme

Figure 1.17: Comparison between active and passive equalization strategy

On-board diagnostics (OBD)

According to Wikipedia [9], On-board diagnostics (OBD) is an automotive term that refers to the self-diagnostic and reporting capability of a vehicle. OBD systems give the vehicle owner or repair technician access to the status of various vehicle subsystems. Modern OBD implementations use a standardized digital communication port to provide real-time data in addition to a standardized set of diagnostic trouble codes, or DTCs, that allow a person to quickly identify and remedy vehicle malfunctions. Some of the faults that can affect batteries are: sensor faults, grid fault, overvoltage (overload), undervoltage (overdischarge), overcurrent in charge or discharge direction, high temperature, low temperature, insulation fault.

1.4 Battery model description

Nowadays, lithium-ion batteries are widely used, for example in mobile devices such as smartphones and smartwatches, but also in traction applications where electric cars are becoming popular.

In the process of designing a battery-powered system, it is critical to use a model that can simulate behavior of the battery with high accuracy. The models can be used for several purposes such as battery characterization and comparisons, state of charge estimation and health conditions, optimization, and design of BMS. For these reasons and many more, there is not just one method of modeling a battery but many, so you can choose the best method each time as needed.

In literature it is possible to find three main model typologies, the electrochemical model, the equivalent circuit model and the Data driven or empirical model.

in any case the accuracy of the model is strongly influenced by the quality of the tests used for the realization of the model.

The Electrochemical It is called electrochemical model because it considers electrochemical kinetics and the charge transfer process, and therefore describes the inner reactions inside the battery. Electrochemical models are based on a number of physical laws, such as the coupling of conservation of mass, charge, and energy, as well as electrochemical kinetics [29]. The models are composed of nonlinear Partial Differential Equations (PDEs), and can only be solved by numerical methods such as the integral approximation, the Pade approximation, the Ritz method, the finite element method, and the finite difference method [25]. Due to the complexity of these models and the deep chemical representation, these models cannot be generalized.

Regarding the cylindrical cell it is possible to consider another method to modelized the behavior. It's possible to simplify the model going from 3D to 2d model under two assumptions: first, insulated conditions for the energy flux are prescribed at the top and bottom surface of the battery, and second as a first approximation, it is assumed that the air temperature is constant around the battery, whence the temperature difference [60].

Equivalent circuit model (ECM) It is called equivalent circuit model because represents the behavior of the cell through electric equivalent circuit components such as resistance and capacitance, [30, 64, 67]. It is therefore not related to the electrochemical processes that take place inside the cell.

The advantage of these models is that since they consist of circuit components, it is possible to treat the battery as an electrical circuit and therefore use all the tools applicable to circuits. Using this approach is also possible to represent the thermal behavior of the battery. This model allows to represent with a good approximation the behavior of the cell. Compared to other methods it shows a lower accuracy in describing the phenomena, because it is not based on the physics of the process, on the other hand it has a lower computational cost.

Data Driven It is called data drive because is based on big data. Completely independent of the phenomena happening in the battery and based on available data. These models can improve their accuracy in real time. On the other hand, the amount of data needed to develop an accurate model is high, and therefore the main problem is the poor amount of data. It is possible therefore to combine the use of the ECM with the Data Driven method, to generate the artificial data to train the neural network in case the number of tests available turns out insufficient.

In this chapter the equivalent electrical models will be proposed, starting from the simplest to the most complex ones. To build a model needs starting from the observation of phenomena and describing them using equivalent electrical elements. it is possible to add complexity depending on the error you wish to obtain. The error can be reduced at will, until the results do not meet expectations. Battery equivalent models have been studied especially for the purpose of vehicle power management control and battery management system development [48]. Several models have been introduced in literature, but the most common ones will be highlighted. All the models' equations are presented in both continuous and discrete time.

1.4.1 Open Circuit Voltage model

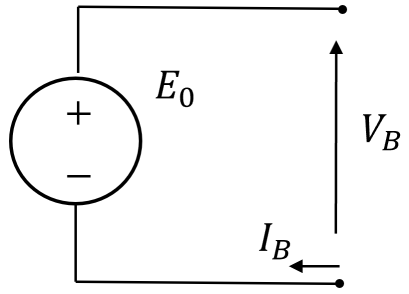

Figure 1.18: Open circuit model

The fundamental behavior of the battery is the open circuit voltage, in fact if you measure the voltage of a cell this value is different from zero. The model use an ideal voltage generator Fig. 1.18, to represent the open circuit voltage phenomena. Obviously this model is static and does not consider current dependence, but it is a good starting point.

$$v(t) = E_0 \tag{1.1}$$

1.4.2 State of Charge dependence

The open-circuit voltage of a charged and an empty battery are different. It is possible to improve to the model to consider this phenomenon. To do this, it is necessary to introduce the concept of *SOC* for a battery. It is defined that *SOC* 1 or 100% is equivalent to fully charged, and *SOC* 0 or 0% is equivalent to fully discharged.

The state of charge (1.2) represents the capacity still present in the battery, as a percentage of the total charge, this value is also called nominal capacity C_{nom}. The *SOC* equation is based on the generator convention, where the current supply by the battery is considered positive, while the current flowing in the battery is negative.

$$SOC(t) = SOC(t_0) - \int_{t_0}^{t} \frac{i_B(t)}{C_{nom}} dt \tag{1.2}$$

The *SOC* equation can be written also in discrete time domain, in this domain the sampling time is defined as Δt, that is the time lapse to measure. Using this definition $t_0 = k\Delta t$ and $t = (k+1)\Delta t$. The equation (1.2) becomes (1.3), and the $DOD_k = 1 - SOC_k$.

$$SOC_{k+1} = SOC_k - \frac{i_{B_k} \times \Delta t}{C_{nom}} \tag{1.3}$$

Back to the model, different battery chemistries present different open circuit voltage as function of the *SOC*, in Fig. 1.19 is possible to see a comparison between five different

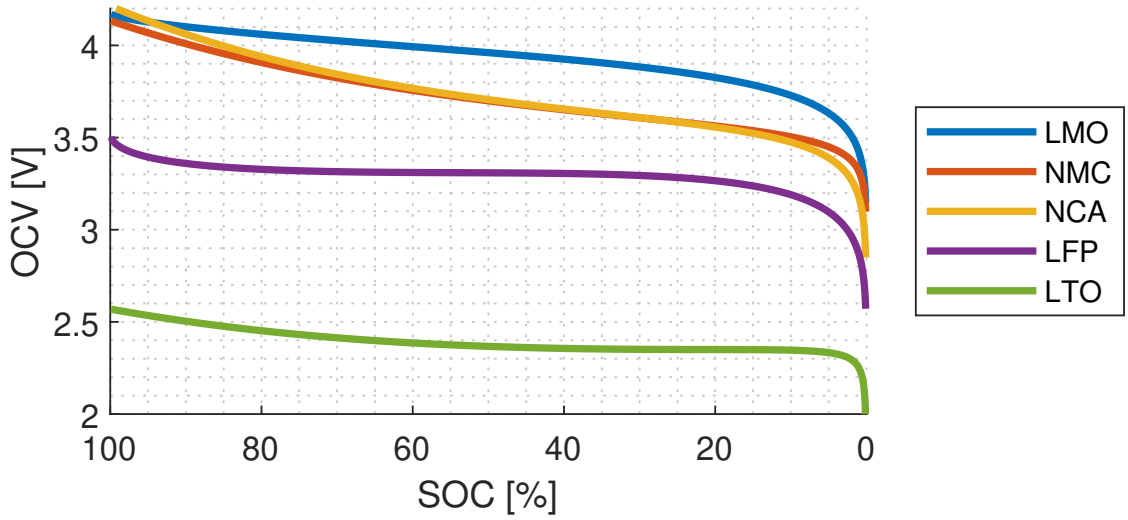

Figure 1.19: Different chemistry OCV comparison

type of battery chemistry.

1.4.3 Equivalent Series resistance

Until now the model is not function of the load, but in the real battery there is a voltage drop, when the current starts flowing form the battery, below the open-circuit voltage, and the terminal voltage rises above the open-circuit voltage when the battery is being charged. To represent this phenomena the equivalent series resistance model (ESR) is introduced, consisting of a voltage generator with a resistance in series Fig. 1.20. In literature it is possible to find this model also under the name of Thevenin's model, this because it refers to the Thevenin's equivalent circuit.

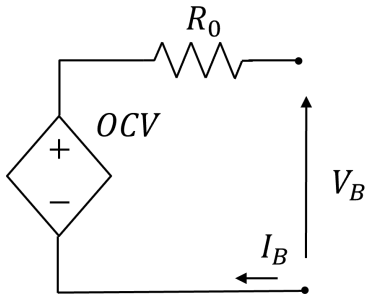

Figure 1.20: ESR model

The voltage at the poles of the battery v_B can be written as a function of SOC and i_B, in the eq. (1.4).

$$V_B(t) = OCV(SOC) - R_0(SOC) \times i_B(t) \tag{1.4}$$

By introducing a resistor in the battery model, the concept of Joule losses is auto-

matically introduced. These losses in fact represent the heat that is generated inside the battery.

$$P_{loss}(t) = R_0 \times i_B^2(t) \tag{1.5}$$

All the equations written before can be rewritten in discrete time, so the equation (1.4) and (1.5), and the state of charge (1.2) become.

$$V_{B_k} = OCV(SOC) - R_0(SOC) \times i_{B_k} \tag{1.6}$$

$$P_{loss_k} = R_0 \times i_{B_k}^2 \tag{1.7}$$

$$SOC_{k+1} = SOC_k - \frac{i_{B_k} \times \Delta t}{C_{nom}} \tag{1.8}$$

1.4.4 Single polarization model

Until now the battery voltage is not directly affected by the battery history, it is only partially affected if one considers the dependence of the open circuit voltage on the *SOC*. But when analyzing the real battery behavior, it is possible to realize that the voltage is a function of the past, in fact if the current is 0 the voltage presents a transient until the open circuit voltage is reached. By analyzing the electrochemical behavior it's possible to associate this effect to the diffusion voltage. To model this aspect a resistance R_1 that model the charge transfer and the double layer capacitance C_1, then the circuit becomes Fig. 1.21.

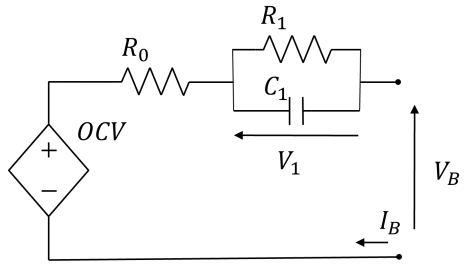

Figure 1.21: Single polarization model

the equation that describes the circuit can be written as follow:

$$V_B(t) = OCV(SOC) - R_0(SOC) \times i_B(t) - V_1(t) \tag{1.9}$$

$$\frac{dV_1(t)}{dt} = \frac{i_B(t)}{C_1} - \frac{V_1(t)}{\tau_1} \tag{1.10}$$

Where $\tau_1 = R_1 \times C_1$. By introducing a component with memory, the system is no longer

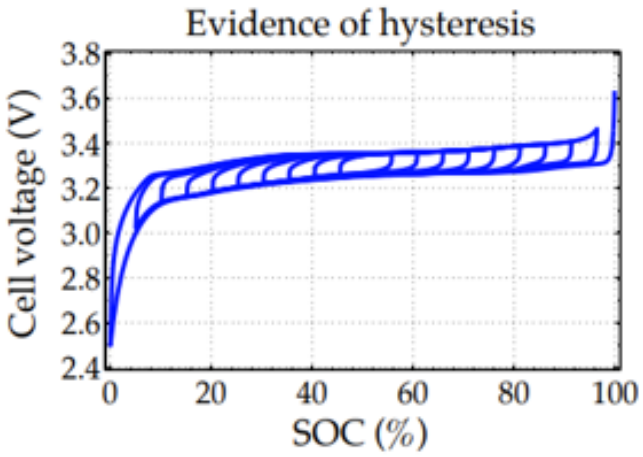

Figure 1.23: LiFePo4 hysteresis characteristic

linear but must be described by differential equations. A possible solution of this circuit can be found by solving the differential equation, after knowing the initial conditions.

$$V_1(t) = V_1(t_0) \times (e^{-(t/\tau_1)}) + R_1 \times i_B(t) \times (1 - e^{-(t/\tau_1)}) \tag{1.11}$$

The power losses for this model can be easily calculated as $P_{loss} = R_0 \times i_B^2 + \frac{V_1^2}{R_1}$.

The solution of the differential equation (1.11) can be rewritten in discrete form as follow:

$$V_{1_{k+1}} = V_{1_k} \times (e^{-(\Delta t/\tau_1)}) + R_1 \times i_{B_k} \times (1 - e^{-(\Delta t/\tau_1)}) \tag{1.12}$$

1.4.5 Hysteresis voltage

For some battery types such as lifepo4, [52] the $OVC - SOC$ characteristic is flat, so to model it, a very accurate measurements must be done. Another fundamental aspect that should also be considered is the hysteresis effect on the open circuit voltage, in fact the open circuit voltage is not only a function of the state of charge, but also the direction of the current.

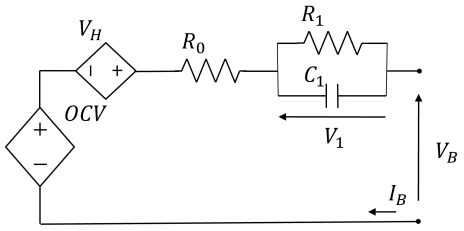

Figure 1.22: LiFePo4 hysteresis model

The OCV obtained during a pulsed discharge is different from OCV obtained from a

pulsed recharge test. Furthermore, if the discharges are not complete, minor loops are obtained. The minor loops curves are "attracted" towards the bounds set by the major discharge/charge loop, but the attraction is completed only after a sort of "delay" in charge, after which the OCV values are almost indistinguishable from experiment to experiment. In other words, the upper and lower bounds are reached only with a "charge delay" after the point in which the charge or discharge process is inverted. The way to model this phenomenon is the same as that used to model the $OCV - SOC$ relationship, namely by means of an equation of state.

$$V_b(t) = OCV(SOC) + V_H - R_0(SOC) \times i_B(t) - V_1(t) \tag{1.13}$$

1.4.6 Firs-order RC model

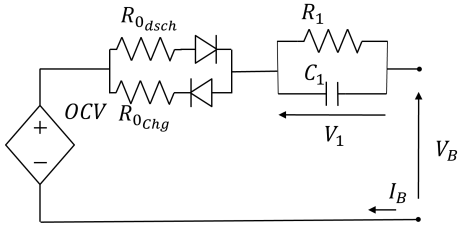

Figure 1.24: First-order RC model

A model widely used in the literature [58, 27], is the first-order RC model, or even where it is necessary to model the hysteresis in the OCV, the firs-order RC model with one state hysteresis. these models are accurate and have a reduced degree of complexity. For these models the resistance is a function of the current, to model this behavior two ideal diodes are inserted (voltage drop equal to 0) to allow the current to flow only in one direction. These two values of internal resistance must be modeled individually, making a pulsed discharge for the parameter $R_{0_{dsch}}$ a pulsed recharge for the parameter $R_{0_{chg}}$.

$$V_b(t) = OCV(SOC) - R_0(SOC, i_B) \times i_B(t) - V_1(t) \tag{1.14}$$

1.4.7 Dual polarization model

Going deeper into the chemical behavior of the cell it is possible to find that there are two phenomena that influence the voltage trend at its poles.

It is possible to identify the contribution due to the migration voltage, caused by the rapid discharge of the double layer capacitance when the ions move away from the electrode surface, and the diffusion voltage caused by the circulation of the redistribution of the ions inside the electrolyte.

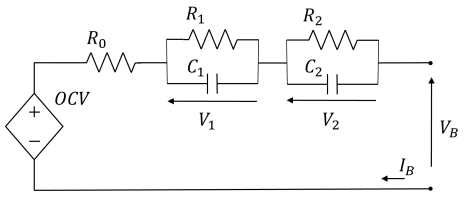

Figure 1.25: Dual polarization model

Therefore, it is logical to imagine an equivalent model that has two-time constants representing these two phenomena. So was born the model called dual polarization, shown in Fig. 1.25.

The equation for this circuit is very similar to that seen for the single polarization model with the only difference that an additional differential equation is added, due to the presence of two-time constants.

$$V_b(t) = OCV(SOC) - R_0(SOC) \times i_B(t) - V_1(t) - V_2(t) \tag{1.15}$$

$$\frac{dV_1(t)}{dt} = \frac{i_B(t)}{C_1} - \frac{V_1(t)}{\tau_1} \tag{1.16}$$

$$\frac{dV_2(t)}{dt} = \frac{i_B(t)}{C_2} - \frac{V_2(t)}{\tau_2} \tag{1.17}$$

Where $\tau_1 = R_1 \times C_1$, and $\tau_2 = R_2 \times C_2$. The accuracy that can be achieved with this circuit is very high, however this circuit is less used than others because the complexity of the system is high too.

All the equation written before can be rewritten in discrete time, so the equation becomes.

$$V_{B_k} = OCV(SOC) - R_0(SOC) \times i_{B_k} - V_{1_{k+1}} - V_{2_{k+1}} \tag{1.18}$$

$$\frac{V_{1_{k+1}} - V_{1_k}}{\Delta t} = \frac{i_{B_k}}{C_1} - \frac{V_{1_k}}{\tau_1} \tag{1.19}$$

$$\frac{V_{2_{k+1}} - V_{2_k}}{\Delta t} = \frac{i_{B_k}}{C_2} - \frac{V_{2_k}}{\tau_2} \tag{1.20}$$

1.5 Battery state

A battery is a very complex system in which chemical reactions, voltage and current, and heat coexist. Consequently, the battery management system must be able to monitor all the phenomena that occur in a battery. An advanced BMS system must not only be able to monitor the fundamental parameters but must also give indications on the state of the battery. For this reason, multiple battery status indicators have been defined in the literature. Fig. 1.26 shows the possible states that can be used. They are: State of Charge (*SOC*),State of Energy (*SOE*), State of Health (*SOH*), State of Power (*SOP*),State of Temperature (*SOT*), and State of Safety (*SOS*).

Some of these such as *SOC*, *SOE*, *SOP* change very rapidly over time, and must be calculated very quickly while others such as the *SOH*, vary slowly over time. This chapter will analyze in detail the various definitions of these parameters that can be found in the literature.

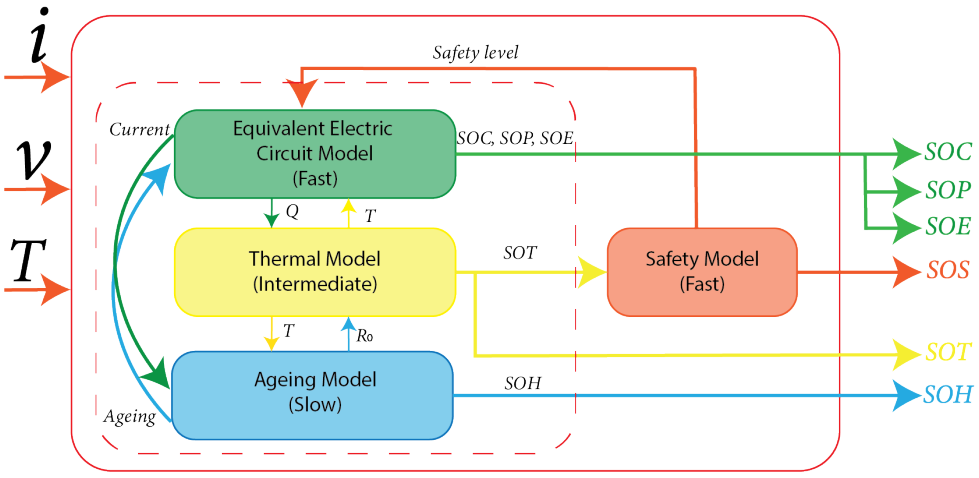

Figure 1.26: Battery state and model architecture [18]

1.5.1 State of Charge

The state of charge represents the residual capacity for a given battery, it is usually expressed as a percentage. It is possible to make an analogy with a car tank, the *SOC* represents how much fuel is still present in the tank compared to how much fuel can be in all the

tank. Is the first indicator that is considered and implemented, the meaning is intuitively recognized. In any electronic device powered by batteries, there is always an indication of the *SOC*, its precision depending on the application, sometimes it is indicated by LEDs that turn off as the *SOC* decreases. Other times the battery voltage is indicated, which in a very approximate way gives information about the *SOC*.

The most used definition is the ratio between the available capacity and the nominal capacity of the battery expressed as a percentage. The battery is considered as a generator, the positive current is delivered from the battery while it is negative when recharging the battery.

It is possible to write this definition, in form of equation as:

$$SOC(t) = SOC(t_0) - \int_{t_0}^{t} \frac{i_B}{C_{nom}} dt \tag{1.21}$$

Where $SOC(t)$, $SOC(t_0)$ represent the *SOC* at the time t and at initial time t_0 respectively. To calculate the *SOC* an integration of the current is made, for this reason if there are errors in the current measurement there is an integration of the error too, for this reason the current measurement must be very precise. In some applications, such as BEVs, where currents have a very large range, two sensors with different ranges can be used, to have a good accuracy for both low and high current values.

Besides, from the perspective of battery electrochemistry, *SOC* refers to the charge contained in both anode and cathode electrode particles. Specifically, the *SOC* variation reflects the distribution of lithium concentration in the electrode particles. Because the amount of available charge is highly dependent on the amount of lithium stored in the electrodes, *SOC* can be directly calculated in terms of mean lithium concentration $\bar{C}_s$ [18].

$$SOC(t) = \frac{\bar{C}_s(t) - C_{s,min}}{C_{s,max} - C_{s,min}} \tag{1.22}$$

where $C_{s,max}$ and $C_{s,min}$ represent the surface lithium-ion concentration when the battery is fully charged and fully discharged. However, this method is not very practical, and it is very complicated to use in real applications, so when refers to the *SOC*, is always used the first definition.

Another indicator for the *SOC* it's called Depth of Discharge (DOD), which indicates

how much the battery has been discharged compared to the maximum charge. It is the complementary of the *SOC*.

$$DOD = 1 - SOC \tag{1.23}$$

It's always possible to complicate the *SOC* model, adding non-idealises to take into account various aspects. The first that is introduced is related to the non-ideality of the chemical reactions, which is called Coulombic efficiency [46]. Coulombic efficiency η_C in a typical lithium-ion cell is around 99 % or higher and is equal to $Q_{discharge}/Q_{charge}$.

$$\frac{Q_{dsc}}{Q_{chg}} \times 100 = \frac{\eta_{c_{chg}}}{\eta_{c_{dsc}}} \triangleq \eta_C \tag{1.24}$$

By definition is considered the discharge efficiency $\eta_{c_{dsc}} = 1$ and the charge efficiency $\eta_{c_{chg}} < 1$

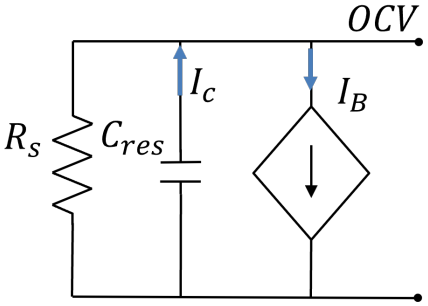

Figure 1.27: Battery state model

Can be calculated as ratio between the capacity [Ah] provided to the accumulator during a charge and the capacity drained from it during the "adjacent" discharge. To correctly model the charge state, the self-recharge phenomenon must be considered, i.e., after long periods of inactivity of the battery, the *SOC* is lower than when it was left. This phenomenon a self discharge resistance is defined R_S.

Another aspect to consider is related to the loss of capacity due to aging, for this reason the normalization should not be done for the nominal capacity but for the residual capacity. Referring to a fuel tank, it is as if the tank of the car reduces its volume over the years, and therefore can hold less fuel.

In Fig. 1.27 is shown the equivalent electric model representing the charge state

$$SOC(t) = SOC(t_0) - \int_{t_0}^{t} \frac{\eta_c i_B + \frac{OCV(SOC)}{R_s}}{C_{res}(SOH)} dt \tag{1.25}$$

1.5.2 State of Energy

Most battery chemistries characterize a pronounced voltage decline during the discharge process, an equal charge throughput at different *SOC* levels provides discrepant energy amounts, especially when approaching both end regions of voltage as shown in Fig. 1.28. High discharge rates may lead to significant internal energy losses in comparison to negligible capacity shrinks.

The generic index of *SOC* can only represent the residual capacity in therms of Amper hour rather than the available energetic reserve in watt hour. Therefore, in some applications it could be convenient to provide the SOE instead of the generic *SOC* index that represents only the residual capacity [Ah], which gives information about the residual energy [Wh].

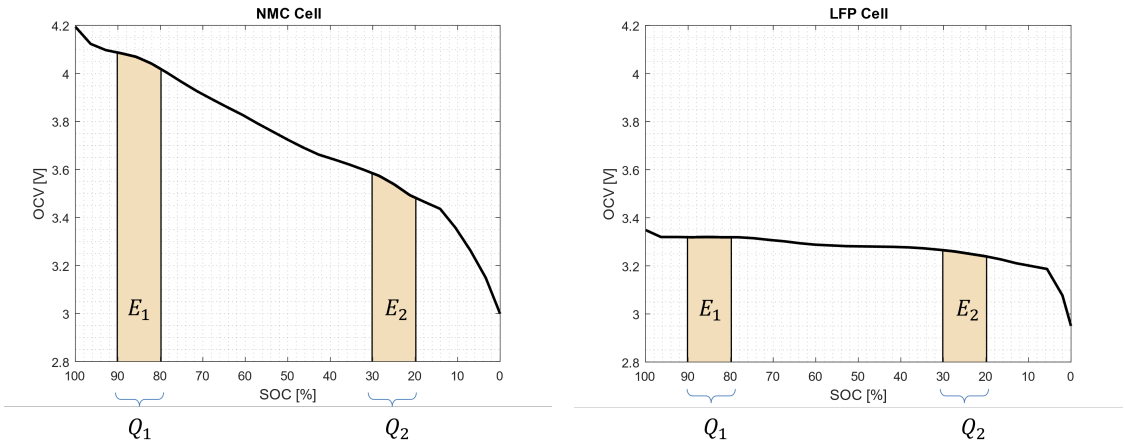

(a) OCV for NMC cell

(b) OCV for LFP cell

Figure 1.28: State of energy comparison between two different chemistries

$$SOE(t) = SOE(t_0) - \int_{t_0}^{t} \frac{\eta_e P_B}{E_{nom}} dt \tag{1.26}$$

Where $SOE(t)$, $SOE(t_0)$ represent the SOE at the time t and at initial time t_0 respectively. P_B is the battery power calculated as $v_B \times i_B$. As with the *SOC*, current integration is performed, so the measurement must have a high accuracy. Energy efficiency η_e is closer to 95 % and is equal to $E_{discharge}/E_{charge}$. Energy is lost in resistive heating on both charge and discharge.

In Fig. 1.28 it is possible to see how different chemistries present more or less marked differences between SOE and *SOC*. For example for cells at LFP, with the same $\Delta SOC = 10\%$ $E_1 \approx E_2$, while for the NMC cell the $E_2 >> E_1$. This means that for the NMC when the battery is discharged at low *SOC* value, the energy available will be much lower than when the battery is charged, at the same ΔSOC.

$$\frac{E_{discharge}}{E_{charge}} \times 100 = \frac{\eta_{e_{chg}}}{\eta_{edsc}} \triangleq \eta_e \tag{1.27}$$

By definition the discharge efficiency is considered $\eta_{e_{dsc}} = 1$ and the charge efficiency $\eta_{e_{chg}} < 1$

The energy available in a battery is related to many factors, and not all the stored energy is usable. In fact, it possible to identify two different contributions that reduce the available energy. The first contribution is related to losses, while the second contribution is the energy that is not usable, due to the internal voltage drop. All the energy stored in the cell is easily calculated as:

$$\int (OCV) dAh \tag{1.28}$$

while the energy delivered net of losses is:

$$\int (V_B) dAh \tag{1.29}$$

the difference between these two curves represents the battery losses

$$\int (OCV - v_B) dAh \tag{1.30}$$

The unreachable energy is caused by the internal voltage drop, which causes the end of discharge, due to reaching the cut-off voltage before the cell is discharged. For these two reasons on the market there are two types of cells, the high energy Fig. 1.29(a) and the High power Fig. 1.29(b). The first has a higher energy density, while the second has a lower internal resistance. For applications where the currents involved are low < 2C, it may make sense to focus more on the installed energy density such as BEVs. While in applications where the current delivered is high > 2C it is preferable to penalize the energy in favor of a reduction of losses and a greater use of energy, for example HEV.

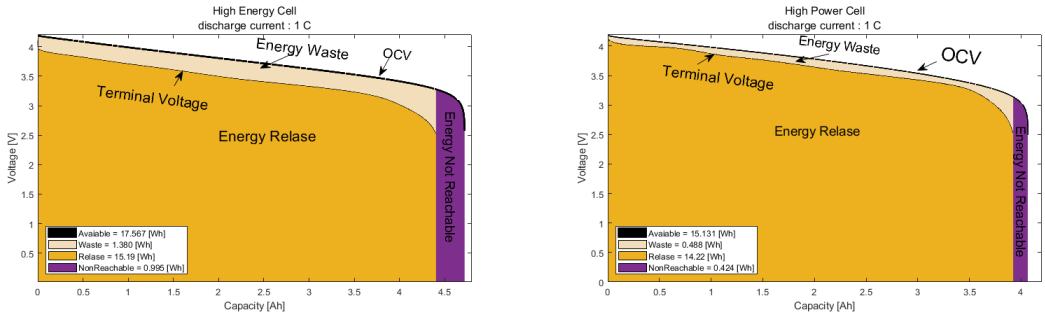

(a) Energy on High Energy Cell

(b) Energy on High Power Cell

Figure 1.29: Energy efficiency comparison between two different cell chemistries

In Fig. 1.29 it is possible to see a comparison between two cells, the first with a nominal energy of 18 Wh and the second with a nominal energy of 15.1 Wh. The figure shows a comparison made with the same C-rate, the losses for the High energy cell are almost 3 times greater, and the energy not reachable is twice as high. Overall then the cells can deliver almost the same energy.

1.5.3 State of Health

Electrochemical batteries inevitably experience gradual performance degradation during their service life, owing to side reactions. This leads to the so-called aging phenomenon that causes losses of lithium inventory and active materials [18].

currently there are two ways to represent in a mathematical way the battery ageing [23], the first one is related to the capacity fade and the second one is related to the internal resistance [62, 23].

$$SOH(t) = \frac{C_{res}}{C_{rated}} \times 100 \tag{1.31}$$

$$SOH(t) = \frac{R_{act} - R_{new}}{R_{new}} \times 100 \tag{1.32}$$

Where the C_{res} and C_{rated} denote the residual and rated capacity values, respectively and R_{act} and R_{new} denote the actual and the new internal resistance respectively.

Usually a capacity fade of 20% is considered as End-of-Life (EOL). As far as the

internal resistance is concerned, currently there is not only one way to define the EOL, but this parameter depends also on the application in which the battery is being used. Some authors propose an increment of 33% but commonly it is considered end-of-life when the internal resistance becomes twice the initial value [17, 18].

Unlike the state of charge, at the moment there aren't sensors that can that can measure the state of health, given the complexity in defining the problem and because it is not represented by a measurable quantity.

1.5.4 State of Power

The Power status (SOP) is another key parameter that the BMS must be able to provide, commonly referred to as the availability of power that the battery is capable of delivering The prediction of the maximum power that the battery can supply in discharging or charging phase is a challenging tasks of battery management systems. In large lithium-ion battery packs due to many factors, such as temperature distribution, cell-to-cell deviations regarding the actual battery impedance or capacity either in initial or aged state, the use of efficient and reliable methods for battery state estimation is required.

The power state can be seen as the product between the actual voltage, and maximum positive or negative current for discharge or charge phase. Mathematically it can be described as (1.33).

$$\begin{aligned} SOP^{charge} &= min(|P_{max}^{charge}|, |v \times i_{max}^{charge}|) \\ SOP^{discharge} &= min(P_{max}^{discharge}, v \times i_{max}^{discharge}) \end{aligned} \tag{1.33}$$

The power that the battery can deliver is a function of the state of charge, in fact if the battery is charged (*SOC* high) the charging current will be limited due to the voltage, similarly if the battery is discharged (*SOC* low) the discharge current will be limited by the voltage. In Fig. 1.30 it is possible to see the trend of voltage and current in four different conditions. [37]

- Fig. 1.30(a) applying constant charge current (Icharge < Imax) while battery voltage is the limiting factor (high SOC);

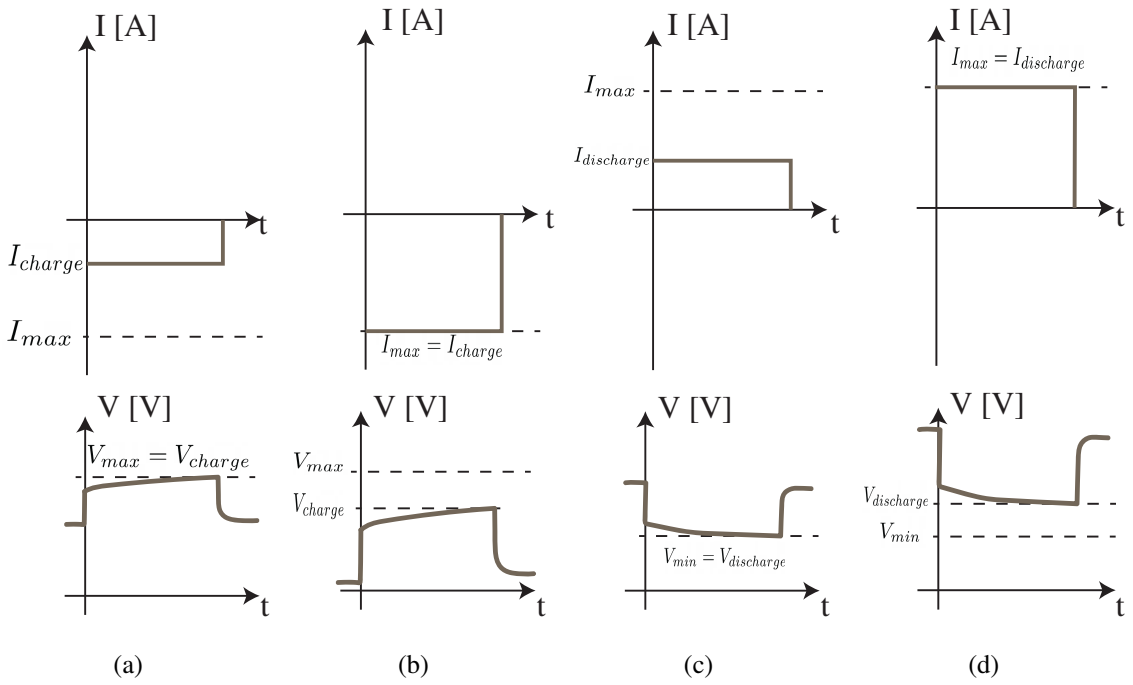

Figure 1.30: Illustration of four cases for limiting available battery power in charging or discharging conditions

- Fig. 1.30(b) applying constant charge current (Icharge = Imax) while current is the limiting factor;
- Fig. 1.30(c) applying constant discharge current (Idischarge > Imin) while battery voltage is the limiting factor (low SOC);
- Fig. 1.30(d) applying constant discharge current (Idischarge = Imin) while current is the limiting factor.

The temperature is a crucial aspect to consider when talking about power output, since the battery works on the basis of electrochemical reactions, at lower temperatures they occur more slowly and for this reason at lower temperatures the performance is lower.

The power that can be delivered by the battery is conditioned by the state of charge. Consequently, the regeneration phase will not be allowed when the cell is fully charged, and the traction phase will be limited when the cell is discharged. Due to thermal problems, aging also causes variations in the power output. In fact the more the *SOH* decreases the more the internal resistance increases and consequently also the losses that it generates,

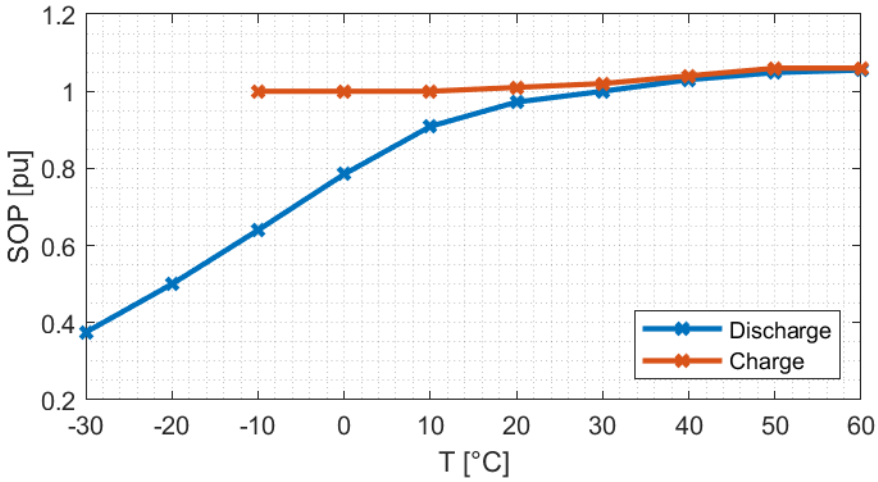

Figure 1.31: Power capability for a LFP lithium ion battery, in charge and discharge conditions vs temperature

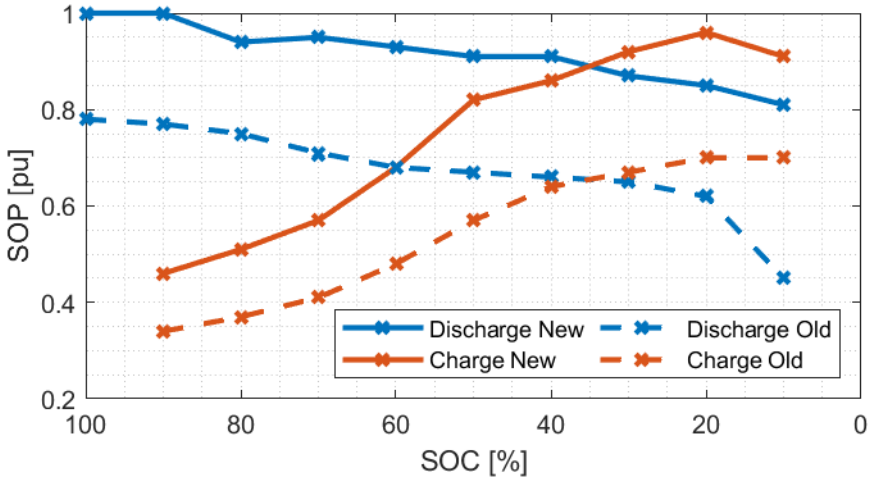

Figure 1.32: Power capability for a LTO lithium ion battery pack in BEV, in charge and discharge in different ageing conditions

and therefore the cooling system is no longer able to dissipate the heat. For this reason, as the battery ages, the power that it can deliver decreases, Fig. 1.32 shows an example of power derating for an LTO cell for BEV application.

1.5.5 State of Temperature

Thermal dynamics of a battery are manifested macroscopically by temperature distribution, which arises from heat generation and dissipation inside a battery cell during normal operations. The heat dissipation is composed of heat conduction, convection, and radiation, the temperature distribution can be represented by Fourier equation.

$$\rho C_p \frac{dT}{dt} = \dot{Q} + hA(T_\infty - T) \tag{1.34}$$

where ρ, C_p, h are the density and specific heat capacity and heat convective coefficient, T_∞, T are ambient temperature and cell temperature, A is the surface area, and Q is the total heat generation rate. For batteries composed of many cells there are often large thermal gradients, and the determination of temperature on each element is very complex and requires three-dimensional models that need a lot of computational power.

For instance, the thermal dynamics of a battery are represented by its bulk temperature in a lumped-mass model.

$$C_s \dot{T}_s = \dot{Q} + \frac{T_s - T_c}{R_c} \tag{1.35}$$

Fourier equation can be represented using an equivalent electrical circuit, where capacitors and resistors are used as thermal storage and heat transfer, respectively. while a current generator is used to represent the heat source. To represent the thermal behavior of a battery, several equivalent electrical circuits can be chosen, with various levels of complexity [65]. Considering only the effect of heat transferred from the radial surface the simpler model shown by Fig. 1.33(b) can be used, while to represent also the heat removed from the poles the more complex model of Fig. 1.33(a) should be used. Regarding the heat transfer the three modes coexist (conduction, convection, and radiation) so they can be represented with different resistances in parallel.

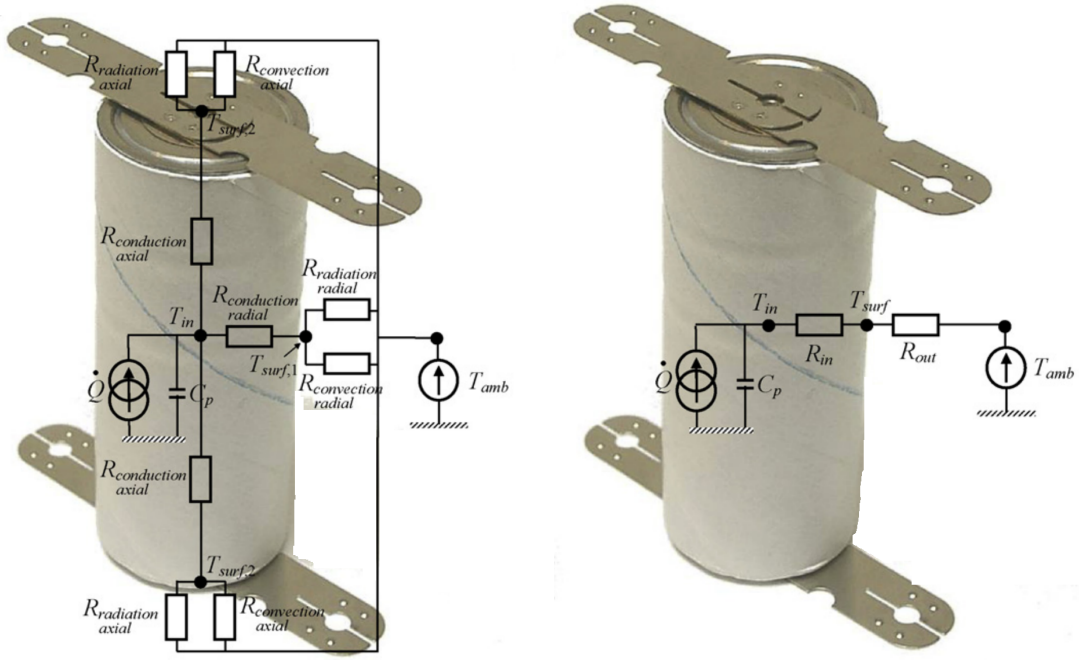

(a) (b)

Figure 1.33: Lumped models (a) complete model and (b) radial model [65]

1.5.6 State of Safety

The state of safety represents how safe a battery is, and is represented with a number ranging from 0 to 1, where 0 means not safe at all, while 1 means safe[18]. Currently, it is not yet unambiguously defined how to define SOS, so there are multiple ways to indicate the safety of a battery. The most common way is based on the concept of hazard risk, the lower the risk the safer the battery is. The hazard risk was defined as product of the hazard severity times the likelihood.

$$H_r = H_s \times H_l \tag{1.36}$$

Another way to define the SOS can be as the reciprocal of a probability function for possible abuses, including voltage, temperature, charging and discharging currents, internal impedance, battery expansion, and battery deformation.

$$f_{SOS}(x) = \frac{1}{f_{abuse}(x)} \tag{1.37}$$

where the $f_{SOS}(x)$ and $f_{abuse}(x)$ are the safety functions and the abuse functions respec-

tively, and x is the state of the system in terms of Voltage, Current, Temperature etc.

It is possible to define a safety operation area (SOA) inside which the battery can operate with a very low risk. The zone is identified by voltage and temperature. In Fig. 1.34 is shown an example, and it shows which are the hazard risks based on the point outside the SOA [55].

SOS is influenced by multiple factors,

- **Temperature**: If surface or internal temperature exceed an upper value, the SEI layer and the active material will start decomposing, resulting in exothermic reactions and possibility of thermal runaway;
- **Current**: Is associated with Joule heat generation, that causes the battery to overheat triggering thermal issues;
- **Voltage**: Over-voltage results in decomposition of the positive electrode and the electrolyte. Under-voltage results on a dissolution of the copper current collector;
- **State of charge**: The higher the energy that could be released as heat or fire during a catastrophic event, the higher the hazard severity in case of event;
- **State of health**: An aged battery may already contain damage on the electrodes, the separator;
- **Internal impedance**: A larger impedance in the negative electrode typically indicates growth of the SEI layer;
- **Mechanical**: Deformation of the battery with respect to the initial dimensions. due to aging or gas formation.

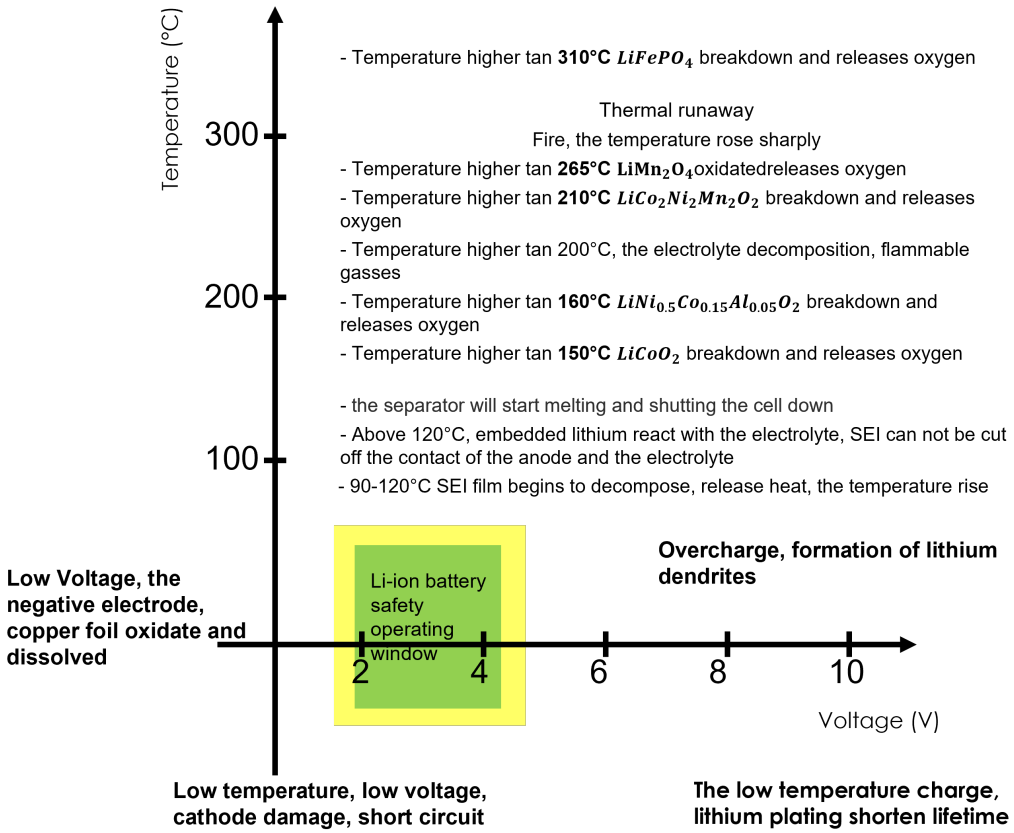

Figure 1.34: Safety operation area for lithium ion battery [55]

1.6 State Estimation Methods

Battery state estimation is a challenging task for the BMS, moreover an accurate estimation can ensure the safe and reliable operation of the battery. The battery state cannot be directly obtained from measurable variables such as voltage and current, but it is also related to other factors such as operating conditions and usage time. In this chapter the main techniques that are used for *SOC* and *SOH* estimation will be presented and some of them will be analyzed for online estimation. The literature review presented here is mostly characterized by an explanation and comparison of the strengths and weaknesses of different online state estimation applications for applications such as PHEVs and BEVs.

Even if the requirements are the same, monitoring algorithms can be designed with different tasks, which are shown in Fig. 1.35. In fact, in the Battery Management System (BMS) several monitor algorithms are co-working since they must estimate different variables and states. Some of them might be necessarily checked online in real time, while others might be offline and checked less often.

Moreover, in PHEVs and BEVs issues related to safety, usage and performance are becoming more and more important. Therefore, a system able to monitor and to act against them is needed. When an abnormal condition is detected by the measurement sensors, battery management system (BMS) must be notified to execute preventive actions.

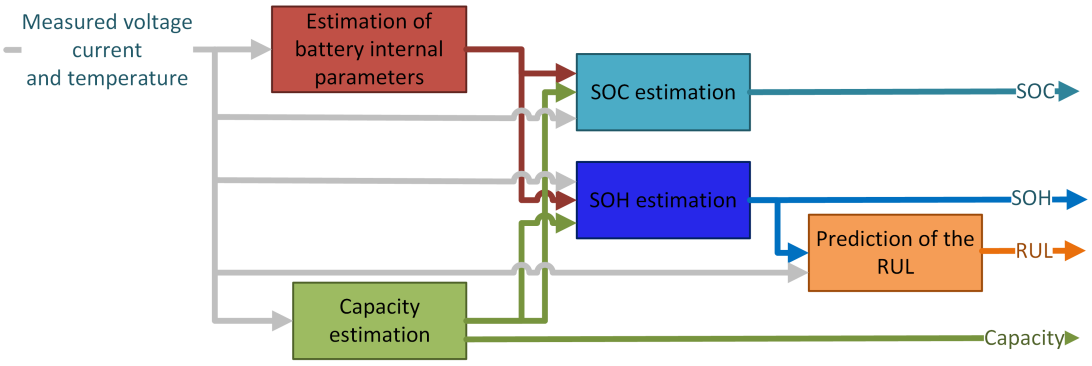

Figure 1.35: State estimation task subdivision

1.6.1 State of Charge

As seen before the state of charge is defined as the remaining capacity of a battery. A correct estimation of the *SOC* plays a fundamental role in the energy management of a vehicle, as an incorrect incorrect estimation of the *SOC* could lead to under-discharge or over-discharge phenomena, which in the long run lead to a greater deterioration of the battery, and therefore to a decrease of its useful life.

Therefore, it is quite difficult to accurately estimate the *SOC* as it is a hidden state. The battery *SOC* estimation methods could be divided into three categories and are presented in Fig. 1.36.

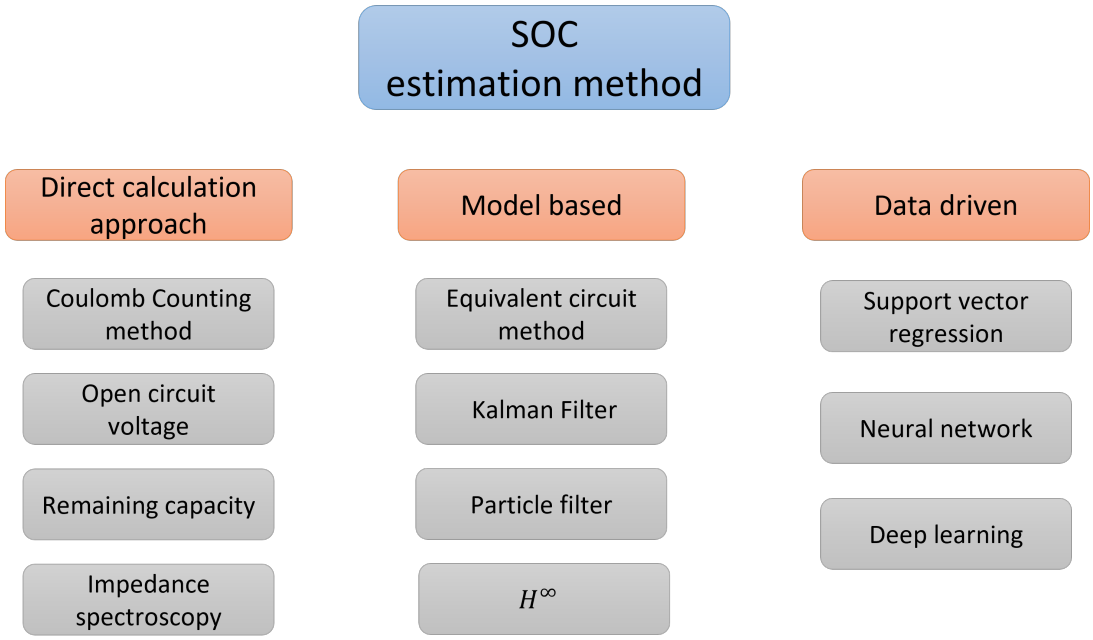

Figure 1.36: SOC estimation methods

Direct calculation approach

This category is made up of those methods that are based on the use of data and parameter characteristics that have been obtained offline and then through the calculation of these parameters online can be traced back to the state of charge. The application of this method is strongly influenced by the stability of the relationship between the parameters and the

SOC.

The most common of these methods, is based on the definition of state of charge, is limited to integrate the current in time, going to normalize this value for the capacity of the battery at that time. Although this is the most common method, it carries out some critical issues. Even though the ampere-hour integral method is classical and widely used method for *SOC* estimation, it has the following three major defects.

- The method requires accurate current measurement. However, the accuracy is usually affected by noise, temperature drift;
- In integral calculation, the random noise is accumulated;
- The deterioration of the battery affects the *SOC* estimation accuracy due to the capacity reduction.

For each type of battery and therefore of chemistry the $OCV - SOC$ relationship is well known and fixed, and for this reason the state of charge can be obtained directly from the open circuit voltage. Typically, this method is used in combination with Coulomb Counting to compensate to current integration error. This procedure is not always trivial:

- For some chemistry such as "LFP" or "LTO" the $OCV - SOC$ curve is very flat and therefore it is necessary to measure the voltage very precisely;
- The method requires accurate voltage measurement. However the accuracy can be affected by voltage drops on electrical connections and also due to the residual inductance;
- It cannot be used alone due to the electrical transients, so the open circuit voltage measurement can be done only after a long inactivity period.

The remaining capacity can be obtained in test experiment through a constant current discharge; however, it is difficult to determine the available capacity with this specific test during actual driving.

The method based on the spectroscopy, to measure the electrochemical impedance needs a very complex methodology to obtain a map between SOC and parameters in function of frequency, therefore it is difficult to get online the impedance values.

Model based

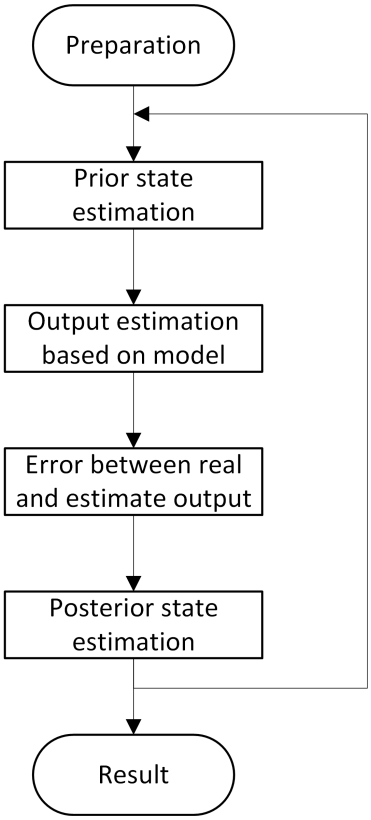

Figure 1.37: Filter-based algorithm flowchart

This method is based on using an equivalent model to determine the state of charge. Therefore, the key point of this method is to build an accurate and reliable model. The ECM based, is the easiest to implement and the one that requires the least computational effort; however, the parameters are affected by many external factors such as *SOC* temperature and *SOH*. The methods based on the filters, such as Kalman Filter (KF) [49, 51] are based on the execution in sequence of the steps shown in the flowchart of Fig. 1.37

1. Based on the previous state and the input value, the current state is estimated;
2. With the current state and input value, through the use of the model, the output is estimated;
3. By measuring the actual output and comparing it with the estimated one, the difference can be obtained;
4. The current state can be estimated again using gain to compensate for the error.

Data driven

Is based on the availability of a large amount of data, which is used to train a model, through a process called training. Once the model has been trained, it is tested with a portion of the data that was not used in the first phase. In this way the accuracy of the model is verified and the last phase consists in testing the model in a new situation not present in the initial dataset. If the model not reach the expected accuracy the whole process is repeated.

1.6.2 State of Health

The definition of *SOH* is based on the residual capacitance or internal resistance, which indicate the energy capacity and power capacity, respectively. *SOH* estimation methods can be grouped into three categories: direct calculation approach, model-based methods and data driven. A schematic representation of most of the possible method to estimate the state of health is shown in Fig. 1.38.

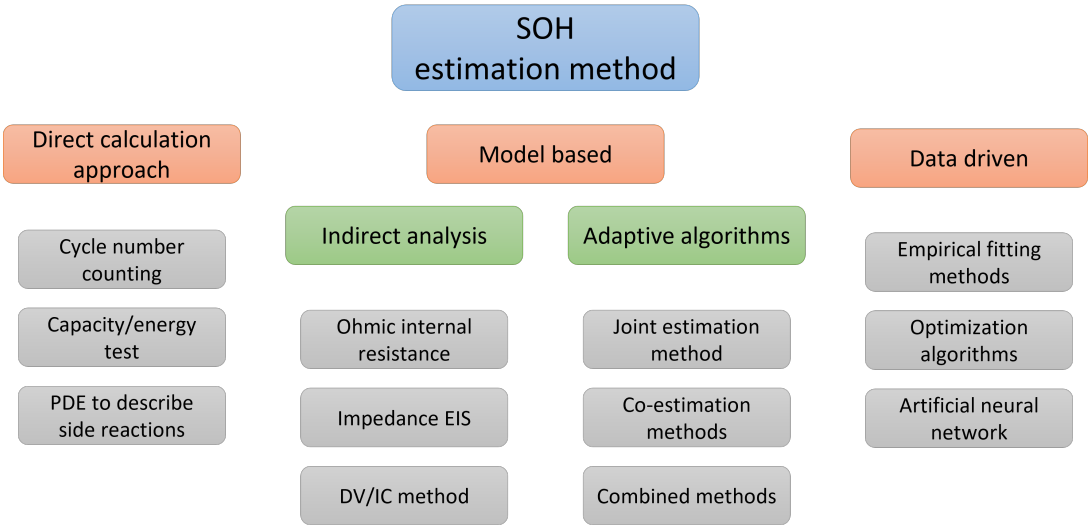

Figure 1.38: SOH estimation methods

Direct calculation approach

The most used method to evaluate the age of a specific battery is based on a simple counter that considers the number of cycles that the battery does in its life. This method is the easiest to implement, however it has a very low accuracy compared to the other methods, as it does not take into account the type and conditions of use.

Capacity and energy testing is based on an estimate of the remaining capacity or energy: for example, by monitoring the remaining capacity it is possible to estimate the remaining life of the battery

Physics-based models use partial differential equations to describe the dynamics of chemical reactions. These models are very accurate, and can be used to estimate collateral reactions, through which battery aging can be assessed.

Model based method

Model-based methods can in turn be divided into two main categories: indirect analysis and adaptive algorithms.

The indirect analysis is divided into two steps, it does not directly calculate the internal capacitance or resistance but goes back to the *SOH* by measuring some parameters that are affected by the change in internal resistance or capacitance.

The incremental capacitance (IC) or differential voltage (DV) curve method analyzes the battery aging process using the IC curve and the DV curve. The IC and DV curves can be obtained from constant current charge-discharge data. The IC curve describes the relationship between dQ/dV and voltage. DV curve describes the relationship between dV/dQ and Q [17]. Recently, incremental capacity analysis (IC) emerges as an effective tool for *SOH* estimation.

Based on ECM, the adaptive algorithms generally identify the model parameters to estimate the *SOH*. These methods are based on closed-loop control or feedback loop, which can adaptively estimate the state based on voltage measurement. Adaptive algorithms include joint estimation method and co-estimation method.

The joint estimation method estimates the model parameters and *SOC* simultaneously, for which two or more filters/observers are used. The model parameters to be identified mainly include internal resistance or impedance As the battery *SOC* is closely related to its capacity, the battery capacity can be determined after the relatively accurate *SOC* value is obtained.

The co-estimation method realizes the simultaneous online estimation of model parameters and *SOC*. Compared to the joint estimation method, the capacity is listed as an additional item of model parameters.

Data-driven

Empirical models are based on the collection of experimental data, to understand the performance of the battery under operating conditions. They typically have a high computational efficiency, and have a good accuracy, if the operating conditions are like the test

conditions. However, obtaining the empirical models requires numerous aging tests that are often time consuming and lab intensive.

Another approach is based on the use of optimization algorithms, which allow to determine the global minimum of a given problem. It is possible, to apply these types of algorithms to determine the *SOH* of a given battery by approaching the problem as if it were an optimization problem.

Also, for *SOH*, data-driven methods such as artificial neural networks are processed due to their model-free features. Specialized battery tests in which *SOH* change are required and must be conducted to train the model. incorporating all *SOH* influencing factors are first conducted. However, the cons of these methods are always the small amount of data available, and the derived model is also often computationally heavy.

2 | Battery Modeling

2.1 Test Equipment

A test platform has been developed for battery testing. The test platform can perform tests on single cells and low-voltage battery packs with a maximum voltage of 60 V and a maximum power of ± 20 kW. Through the experimental tests, and through the processing of collected data, it is possible to obtain the parameters necessary for the battery modeling or to perform comparative tests between batteries of different manufacturers.

The main requirements for the test bench are:

- capability to either charge and discharge the storage system under test;
- capability to control the test temperature;
- capability to measure and store several quantities (voltages, current and some temperatures) and store all the data for post-processing.

An additional aspect to be considered is related to the duration of the test, which may last from a couple of hours up to tens days or even months for aging tests, and therefore it is necessary to create an autonomous system that runs on a real-time basis. The test bench has been equipped with a PC that allows, through an user interface, to visualize the progress of the test and the measured quantities.

The scheme of the hardware architecture of the test bench is shown in the Fig. 2.1. The Tab. 2.1 shows all the specifications of the components used. The image of the test bench is shown in Fig. 2.9

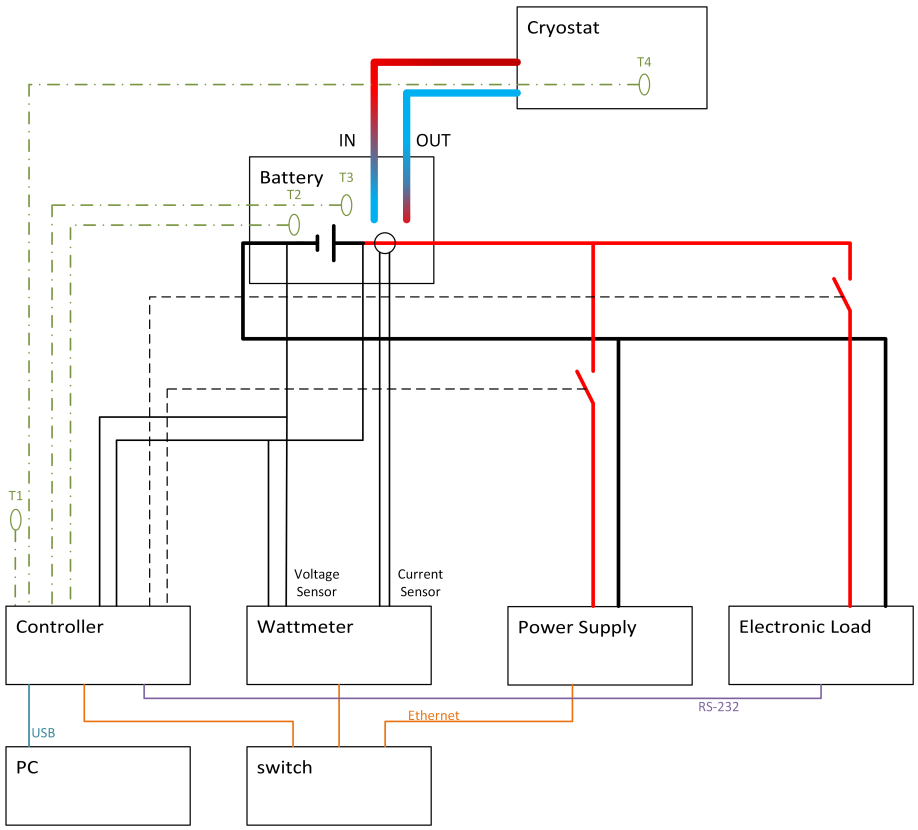

Figure 2.1: Test bench hardware scheme

Table 2.1: Test banach equipment specifications

Power Supply	TDK-Lambda GEN60-40
Electronic Load	BK Precision 8514
Wattmeter	Yokogawa WT310EH
Cryostat	Jeio Tech RW3-0525P
Controller	NI cRIO-9066

Testing battery The test bench can perform tests on individual cells or battery packs. For single cell testing a holder is used, which allows for four-wire voltage sensing. For battery pack tests the voltage is measured by the BMS and is transmitted to the test bench through the CAN-Bus communication protocol.

To test the models, a prototype battery pack with an included BMS was built for the test purpose. The battery is composed of Panasonic 18650GA cells, in 10p12S configuration. with a current sensor and two temperature sensors, while the equalization is passive and managed by the BMS.

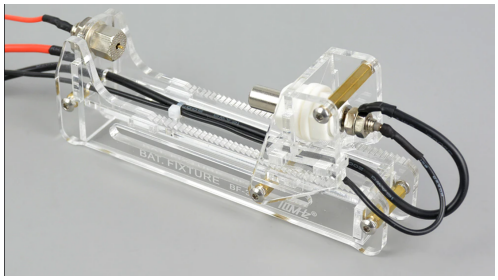

(a) Cell holder

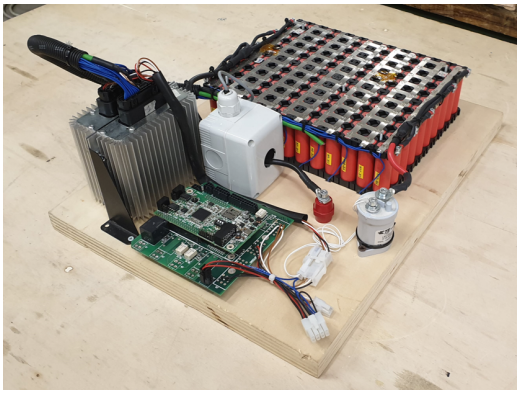

(b) Battery prototype

Figure 2.2: Testing battery

Electronic Load The electronic load, shown in Fig. 2.3 is a BK PRECISION 8514. This device is equipped with two terminals to which the power source is connected, which in this case is the battery to test. This device allows to simulate different discharge profile from the battery and is capable to drain programmable currents values, which can be set either through the keys or through commands sent via RS-232 protocol.

Power Supply The power supply shown in Fig. 2.4, is a TDK lambda Genesys GEN60-40, that supplies current to the battery and allows allows to simulate the battery charger. The charging current is sent via an Ethernet cable from the controller.

Power-meter The power-meter used is a Yokogawa WT310EH Power Analyzer, shown in Fig. 2.5 is an instrument that allows measurement of quantities in a single phase system.

Figure 2.3: Electronic load

Figure 2.4: Power supply

Its task in the test bench is to measure the voltage and current of the battery under test. The power-meter guarantee that all the measurements are certified.

Figure 2.5: Power-meter

Cryostat Refrigerating & Heating Bath Circulator, shown in Fig. 2.6, is capable to control the temperature of a fluid, which in turn is used to set the battery temperature, in particular there are two pipes one for the outflow and one for the inflow of the liquid and a reserve tank. A support has been created for testing cylindrical cells that is able to maintain the cell at the desired temperature. This device, is able to heat or cool the liquid,

and consequently it is possible to make tests both at higher and lower temperature than the environment.

Figure 2.6: Refrigerating & heating bath circulator

Figure 2.7: Riello UPS (uninterruptible power supply)

UPS An UPS Fig. 2.8 has been added to guarantee the continuation of the tests in case of momentary interruption of the power supply. The UPS is capable of supplying a power

of 3 kVA at 230 V, and can communicate with the measurement system through the RS232 protocol.

Controller The CompactRIO 9066, shown in Fig. 2.8, is a platform developed by NATIONAL INSTRUMENTS^{TM} that allows the easy creation of real-time control programs, which can be developed using the LABVIEW^{TM} programming language. This device is also equipped with an FPGA.

This device manages all the elements of the test bench and handles all the tests. The controller is connected:

- to the switch through an Ethernet port to communicate with the power supply and power-meter;
- to the electronic load through RS232 serial port;
- to the PC through the USB port.

The log files containing the data of the tests carried out are automatically saved in a USB flash drive on site, so as to facilitate the management of the tests. USB flash drive on site, in order to facilitate the use in case a PC is not available nearby once the available in the vicinity once the tests have been completed.

Figure 2.8: CompactRIO

It is possible to enable up to four temperature sensors for each type of test. Setting a safety temperature threshold it is possible to automatically stop the test if the temperature

limit is reached. For each type of test there is a time limit, at the end of which the test is interrupted regardless of whether or not the other end-of-test conditions have been reached.

The tests executable from the test bench, implemented in the software are:

- **CHARGE CC/VEOC** : constant current charge until the user-selected voltage is reached. Voltage is set by the user during the configuration phase;
- **CHARGE CC-CV** : constant current charge until a chosen voltage value is reached, followed by a constant voltage phase with decreasing current up to a minimum current threshold. Both current and voltage thresholds are user-defined during configuration;
- **DISCHARGE CC/VEOD** : Discharge at constant current until the voltage threshold is reached;
- **DISCHARGE CP/VEOD** : constant power discharge until a minimum voltage threshold value selected by the user is reached;
- **ARBITRARY** : a current profile is followed, with either positive or negative instantaneous values, so that the cell supplies or absorbs current according to the assigned values. The current profile is defined through a .txt file with two columns, showing respectively the current value and the relative time;
- **REST PERIOD** : a rest period with no charge / discharge current, while voltage and temperature values are sampled anyway, in order to monitor the cell during the rest period.

Figure 2.9: Test bench

2.2 Parameters identifications

In this section will discuss the procedure for obtaining the parameters of the battery model. This procedure is widely used in the literature and has been dealt with in detail [14, 70], all the steps will be shown for the determination of the parameters of the SP model. The process to determine the parameters starts from a pulsed discharge test Fig. 2.11, with alternated periods of discharge with a predetermined current, and pause periods in which the current is 0. In the discharge periods the battery is discharged, while in the pause periods the transients on the battery voltage are observed; in this phase the time constants of the circuit can be identified.

The realization and description of the model will consider the most common type of chemistry, the NMC, which in the coming years is expected to cover 70% of batteries on the market [12]. All equations and tests done maintain their validity even for different types, however the trend of the parameters may be different.

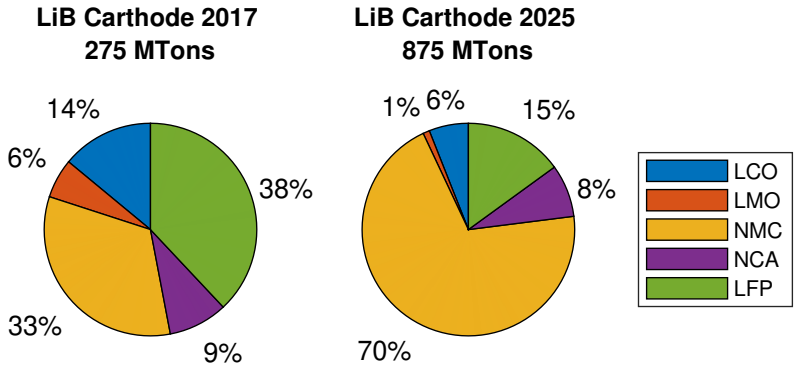

Figure 2.10: Battery market share comparison [12]

2.2.1 SOC-dependent parameters

To perform the pulsed test, the current, the discharge time and the pause time must be chosen. The current depends on the test that is being performed, while the times are crucial for the result of the parameter estimation, so let's explore the effects of the two

intervals. For each discharge period, it is possible to associate a *SOC* value, and then a *OCV* value, R_0, etc, associated to that *SOC* value. Consequently, the shorter the discharges, the more SOC-parameter points can be obtained in a complete battery discharge. The relaxation transient on the contrary should be, if possible, to wait for the extinction of all transients. In the literature [68, 54, 43] there are no standards for defining timing, a good trade-off is $T_{on} = 120s$, $T_{off} = 600s$, i.e. one sample every 3.3% of *SOC*; considering 1C discharge rate during T_{on}, with these timings the test takes six hours. Noting the trend of the parameters it is possible to optimize the pulsed discharge profile to reduce the test time, but at the same time to improve the accuracy of the test in areas where the parameters vary more. The profile of Fig. 2.11 developed specifically for batteries with NMC chemistry, has a $T_{off} = 900s$, and a variable discharge time, so as to obtain samples referenced to $SOC = [100, 96, 92, 88, 84, 80, 70, 55, 40, 25, 20, 16, 12, 8, 4, 0]$. In this way it is possible to get a higher number of points for high and low *SOC*, and make less pauses in the middle zone, thus reducing the test time. with this profile the total time is only four hours.

In this curve five points can be identified, which are used for the determination of the model parameters, shown in Fig. 2.12. "I" the beginning of the discharge, "II" the sample following point "I" which is considered for the calculation of the series resistance R_0, in which the effect of the transients is still considered negligible. "III" the end of the discharge "IV" the sample following "III" in which the effect of the relaxation transients is considered negligible. "V" corresponds to point "I" of the next discharge.

Open Circuit Voltage

The open-circuit voltage is the battery terminal voltage when no current flows and the transients are expired. To obtain the open-circuit voltage it is sufficient to measure the cell voltage in stationary conditions, in the pulsed test these conditions occur at point "I". By collecting all the no-load voltage values at point, "I" of each discharge, it is possible to create a *OCV* vector as a function of *SOC*. An example of a curve is shown Fig. 2.13, in which the points obtained from the "$\times$" test were interpolated.

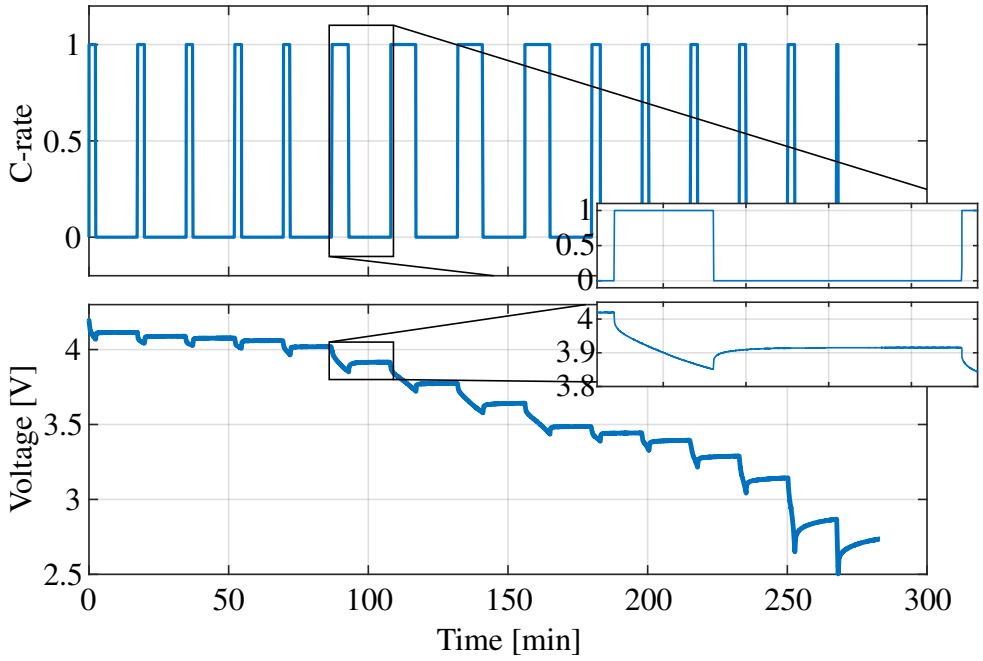

Figure 2.11: Pulse discharge test. Current and typical voltage profile for a 21700 NMC high power Li-Ion cell.

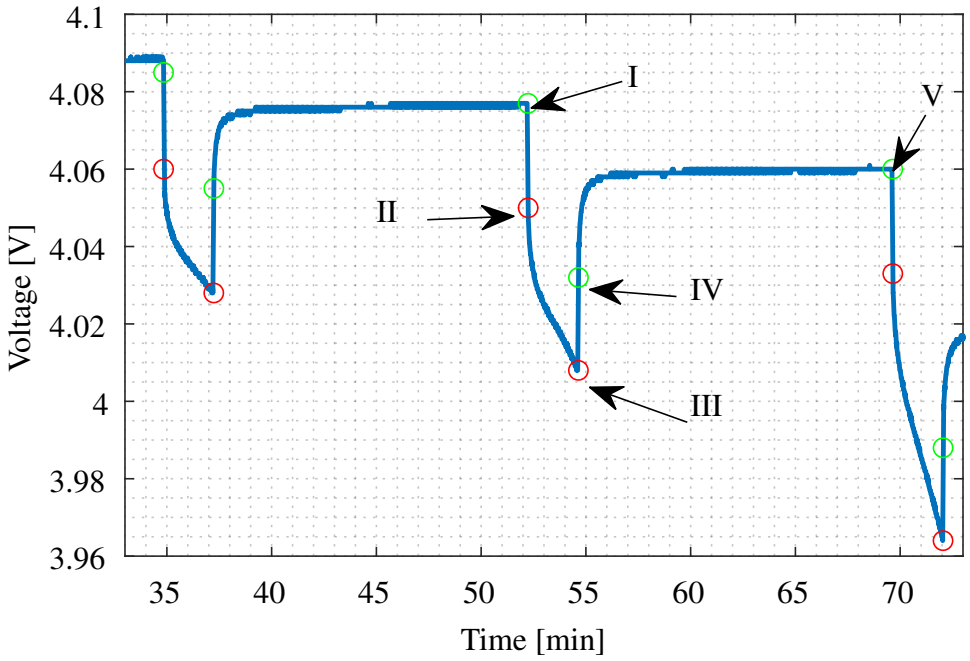

Figure 2.12: Pulse discharge test, interesting points

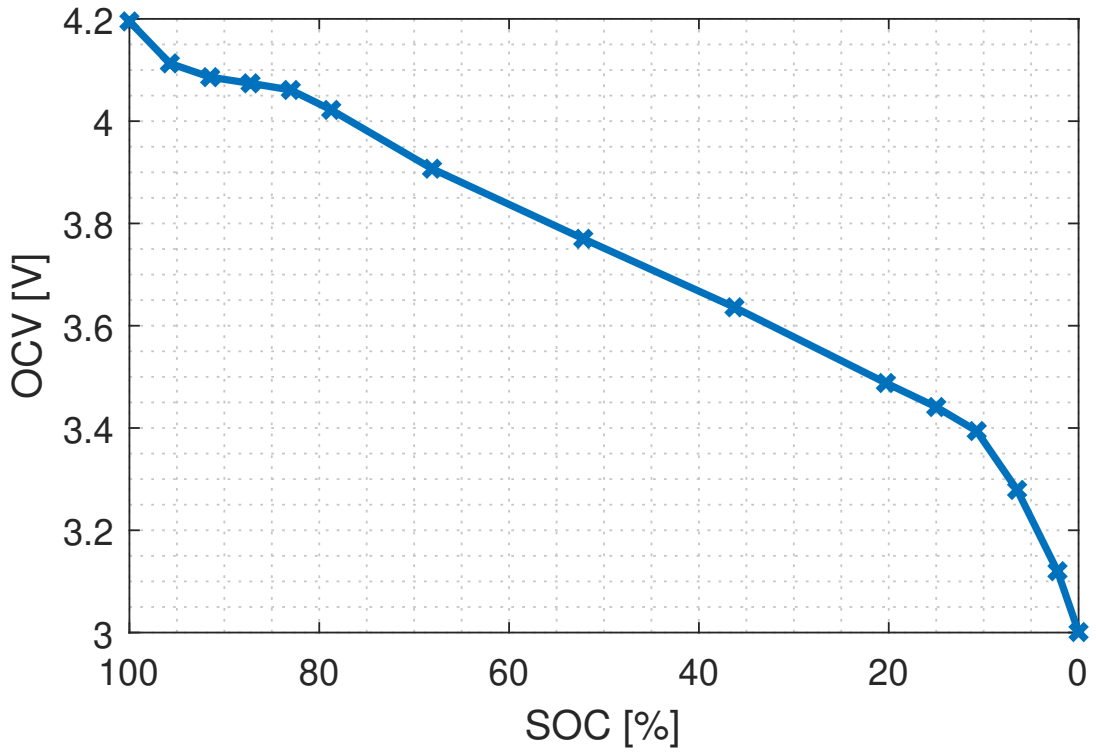

Figure 2.13: Open circuit voltage

Series Resistance

The internal resistance is used to model the voltage drop from no-load to on-load, this parameter can therefore be derived from both the transition from no-load to load and vice versa.

The system can be described by two equations, one for point "I" and one for point "II".

$$\begin{cases} I, & i_B = 0, \quad v_B(I) = OCV \\ II, & i_B = 0, \quad v_B(II) = OCV - V_{R_0} \end{cases} \tag{2.1}$$

Where V_{R_0} is the voltage drop across the series resistor R_0, the value of which is to be calculated .

$$\begin{cases} I, & i_B = 0, \quad v_B(I) = OCV \\ II, & i_B = 0, \quad v_B(II) = OCV - R_0 \times i_B \end{cases} \tag{2.2}$$

By subtracting member by member the two equations $v_B(I) - V_B(II)$ one can obtain

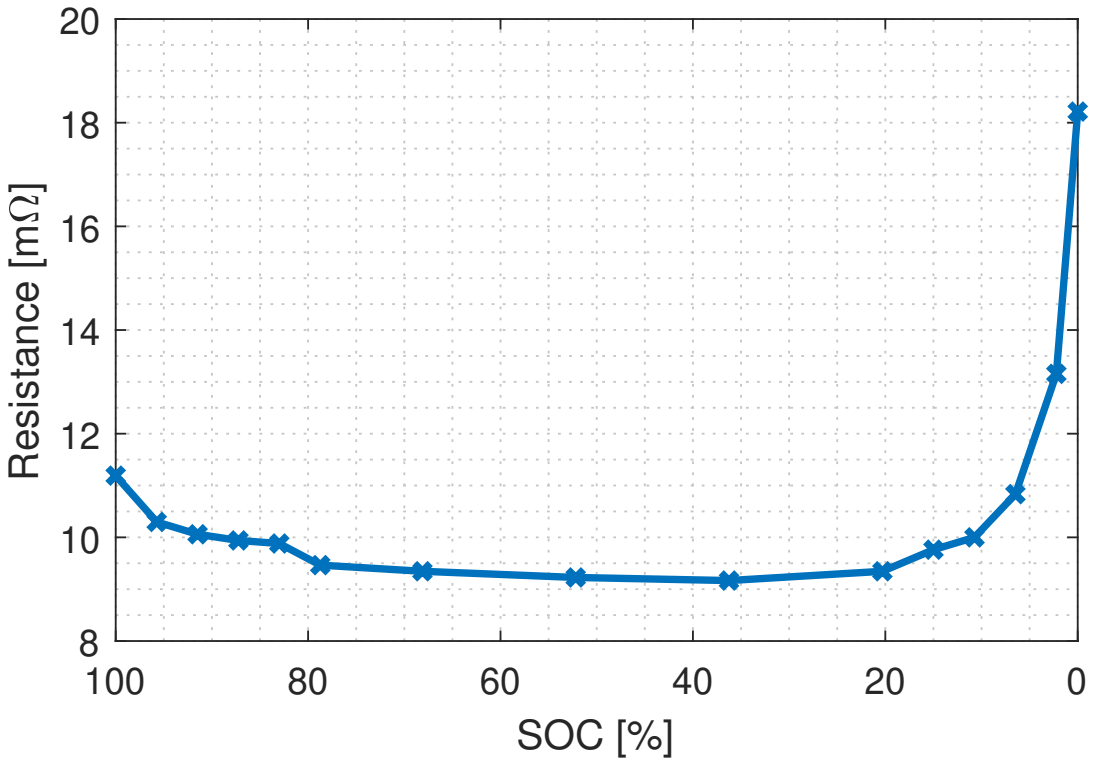

Figure 2.14: Series resistance R_0

the (2.3)

$$v_B(I) - v_B(II) = OCV(I) - OCV(II) - R_0 \times i_B \tag{2.3}$$

Supposing that between point "I" and point "II" the SOC has varied slightly, so it can be neglected, it can be assumed that $OCV(I) = OCV(II)$.

$$R_0 = \frac{v_B(I) - v_B(II)}{i_B} \tag{2.4}$$

Similarly, it is possible to repeat the same logic for the relaxation transient where there is a change from load to no load, thus making it possible to obtain two sets of values for R_0, which will be called $R_{0_{Disch}}$, $R_{0_{Relax}}$ respectively.

$$\begin{aligned} R_{0_{Disch}} &= \frac{v_B(I) - v_B(II)}{i_B} \\ R_{0_{Relax}} &= \frac{v_B(IV) - v_B(III)}{i_B} \end{aligned} \tag{2.5}$$

Due to the nature of the test, the resistance $R_{0_{Disch}}$ calculated between points "I" and

"II" corresponds to a certain value of *SOC*, while the $R_{0_{Relax}}$ calculated between points "III" and IV corresponds to a lower value of *SOC*. For this reason the resistance value for *SOC* 100% will be available only in terms of $R_{0_{Disch}}$, and the resistance value for *SOC* 0% will be available only in terms of $R_{0_{Relax}}$. For the central points, an average is made between the two values with the same *SOC*. The final result is as shown in Fig. 2.14

Time Constant

The time constant represents how long it takes the battery to quench its transient, and thus return to the *OCV*. For the description of the model, the time constant only is not enough, but it is necessary to estimate also the value of the resistor R_1. Similarly to what was said for the series resistance, this value can be obtained from both the discharge and relaxation transients.

It is possible to analyze both transients separately. Starting from the discharge, the equation ruling this phase is.

$$v_B(t) = OCV - R_0 \times I_B - R_1 \times I_B(1 - e^{-\frac{t}{\tau_1}}) \tag{2.6}$$

To obtain the branch parameters R_1 and C_1, let's move the curve back to the origin of the axes, $v_B(t) - OCV + R_0 \times I_B$.

Using the MATLAB® "lsqnonlin" tool, to fit the voltage curve with the (2.7) in order to determine the parameters.

$$v_B(t) = R_1 \times I_B(e^{-\frac{t}{\tau_1}} - 1) \tag{2.7}$$

In the discharge transient, however, the *SOC* value changes over the time, and consequently the variation of the parameter due to *SOC* should be taken into account, which is neglected in this discussion. A further problem on the use of the discharge transient for the determination of the parameters is related to the short observation window, due to the reasons previously analyzed.

For these reasons, the relaxation transient, which will be presented now, is used to determine the parameters. The reference equation in this case is (2.8).

$$v_B(t) = OCV - V_{R_1}(t_0)(e^{-\frac{t}{\tau_1}} - 1) \tag{2.8}$$

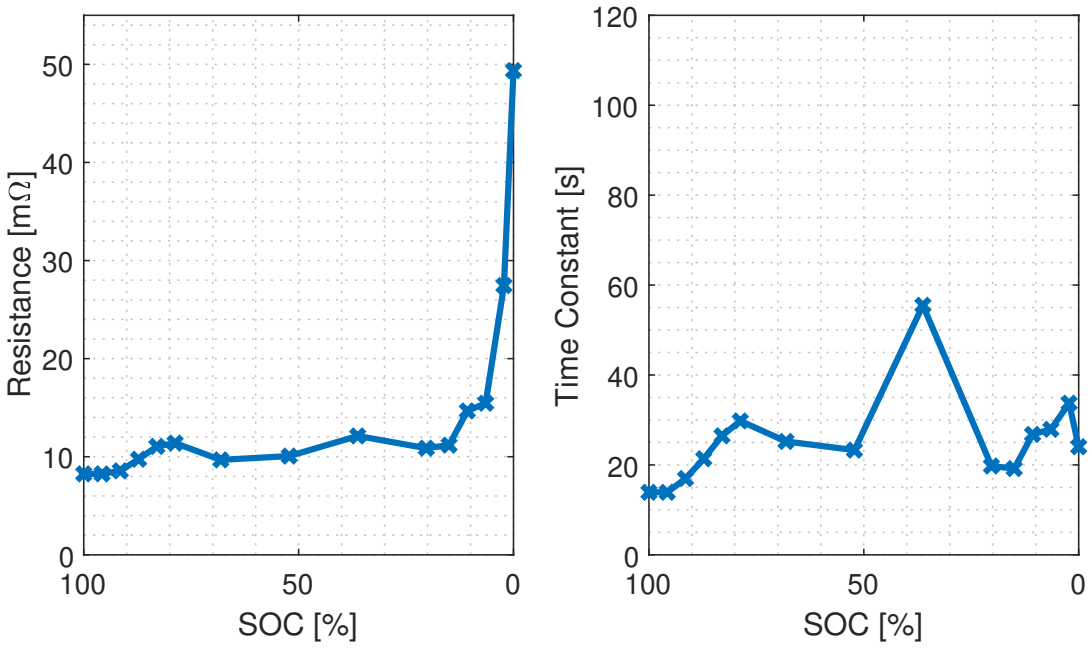

Figure 2.15: Time constant R_1, τ_1

Similarly to what has been done for the discharge phase, the curve is plotted at the origin of the axes $v_B(t) - OCV$.

$$v_B(t) = V_{R_1}(t_0)(1 - e^{-\frac{t}{\tau_1}}) \tag{2.9}$$

$$V_{R_1}(t_0) = R_1 \times i_B(1 - e^{-\frac{t^*}{\tau_1}}) \tag{2.10}$$

where t^* corresponds to the discharge time

By substituting the equation (2.10) into (2.9) it is possible to derive the equation to be used to interpolate the voltage trend into the relaxation curve. In this way the parameters obtained are not a function of the *SOC*, moreover the time constants for the batteries typically go from tens of seconds to a couple of minutes, and in the type of test the relaxation time is 15 minutes, sufficient for the extinction of transients.

$$V_{R_1}(t_0) = R_1 \times i_B(1 - e^{-\frac{t^*}{\tau_1}}) \times (1 - e^{-\frac{t}{\tau_1}}) \tag{2.11}$$

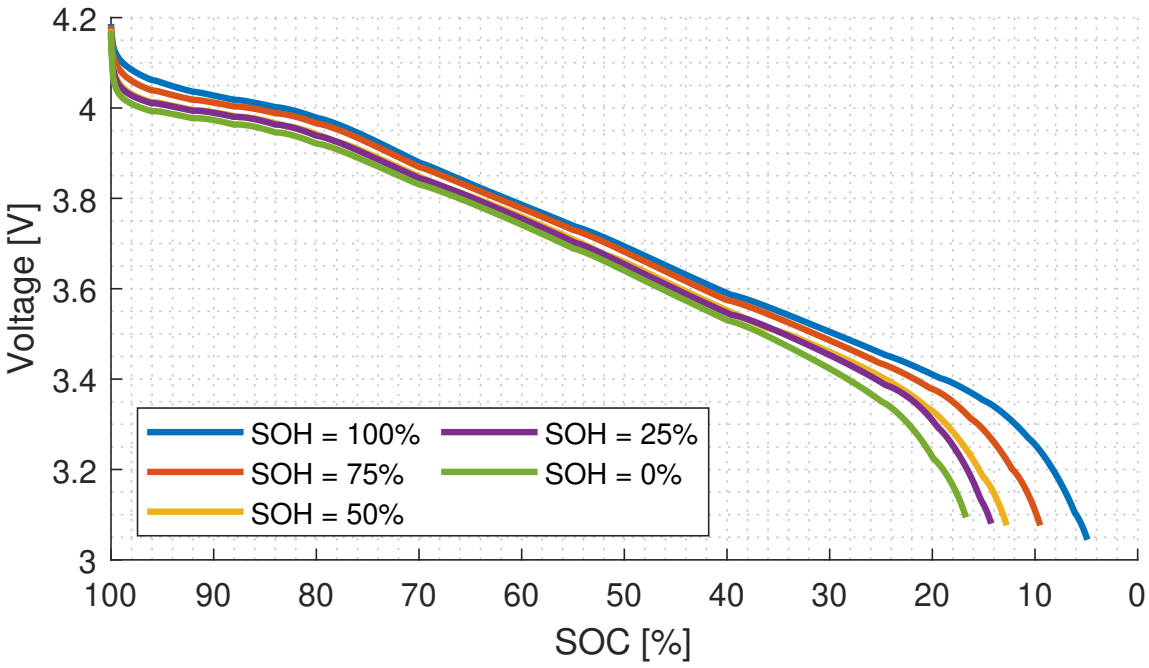

Figure 2.16: Discharge battery voltage, with different temperature

2.2.2 Ageing-dependent parameters

In Fig. 2.16 it is shown the voltage trend with different ageing, and it is possible to see that the voltage drop is greater when the *SOH* is lower, for this reason it is possible to model this effect with a reduction of internal resistance, and the decrease in capacity due to aging phenomena

Capacity of a battery is defined as the amount of charge it can store in fully charged condition, due to the ageing mechanisms the capacity decreases over the time. It can be calculated by integrating the current drawn from the battery over time from fully charged to fully discharged condition.

$$Q = \int_{t_{chg}}^{t_{dsc}} i_B dt \tag{2.12}$$

Where Q is the cell capacity, t_{chg} and t_{dsc} are the time at the fully charged and discharged condition respectively, and i_B is the battery current. As seen above, the battery is at the end of its life when the remaining capacity is less than 80% of its rated value. This chapter will analyze how it is possible to derive a trend between capacity and number of cycles.

The aging model aims to create a dependency between the capacity of the battery and the number of cycles without considering the phenomena that occur inside.

The electrolytic resistance, the charge transfer resistance, and the double layer capacitance C of the battery increase gradually due to repeated cycling. To consider these aspects, it is necessary to introduce in the models the dependence of the parameters R_0, R_1, C_1 on the number of cycles. Thanks to the tests carried out in the laboratory it was possible to notice a reduced variation of R_1 and C_1 from SOH, for this reason these parameters are considered constant throughout the life of the battery, consequently in this chapter will be describe only the dependence of R_0 from SOH.

In order to obtain the parameters as a function of aging, a test procedure was carried out, shown in flowchart form in Fig. 2.17. Tests were performed on an LG brand 21700 cylindrical cell with an NMC chemistry that has a rated capacity of 4.85 Ah. For the determination of the parameters the pulsed test, explained above, is used. For aging the test can be of any type, and is alternated by discharge and charge tests, the number of iterations is increased by 1 at each charge. After every 50 cycles a pulsed test is carried out through which it is possible to obtain the parameters of the model. The most common way to cycle cells is by constant current charging and discharging. For the test, the battery is charged with constant current at 0.7 C (3.39 A) up to 4.2 V and then with constant voltage at 4.2 V till charge current decreases to 0.04 C (0.2 A) followed by discharge current of 1.5 C (7.27 A). Aging and pulse discharge tests are performed at constant room temperature ($25°C$), in order to consider only the effect of ageing.

Capacity

To ensure that the cell capacity is obtained by the pulse discharge test is not affected by the ageing test, the charge before the pulsed discharge is done with a constant current at 0.3 C (1.45 A) to 4.2 V and then with constant voltage at 4.2 V till a cutoff current of 0.01 C (0.05 A) is reached. The cell capacity value C_{res} is obtained with the integration of the current during the pulsed test as shown in (2.12)

Once obtained the values every 50 cycles, the trend of capacity fade can be observed, and it is then possible to interpolate these data as a function of the number of cycles, as

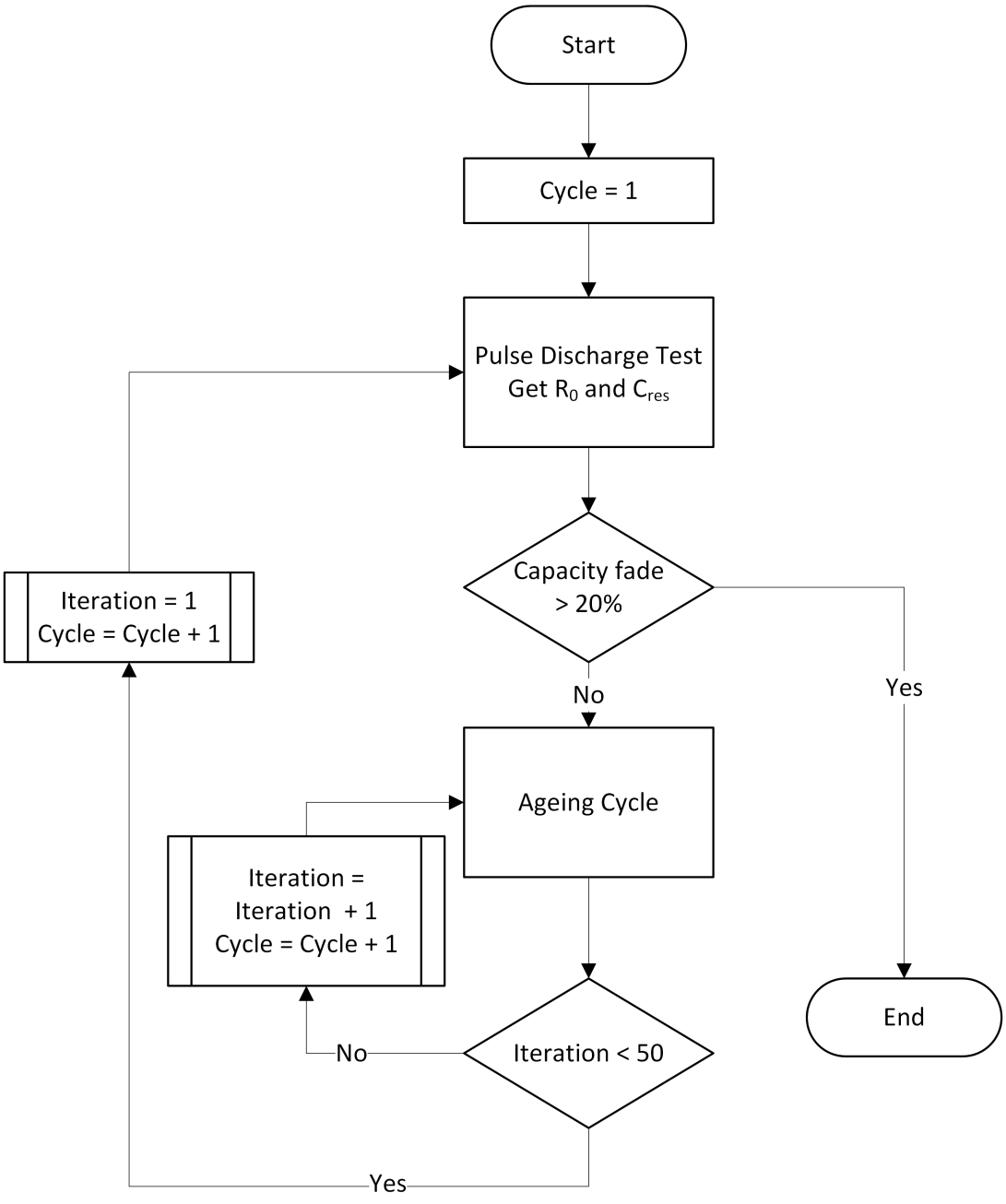

Figure 2.17: Flowchart of the procedure for ageing test

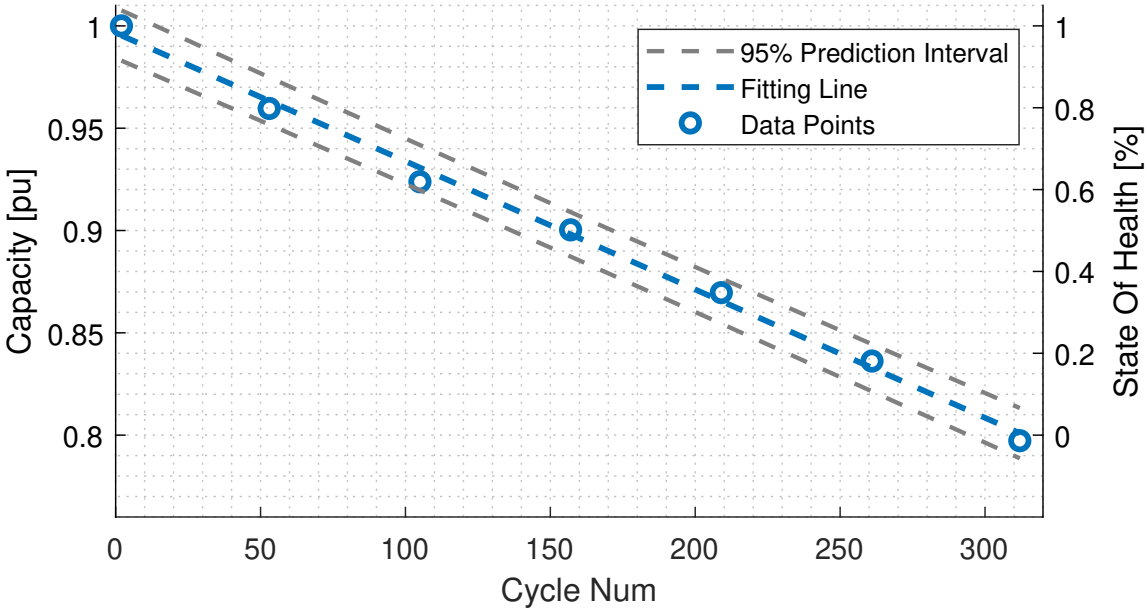

Figure 2.18: Capacity fade in 300 cycle

shown in Fig. 2.18. The "$\circ$" indicates the sample point got from the pulse discharge test and the dashed line the interpolation of the point.

The trend in capacitance as a function of the number of cycles is linear, and the interpolating equation (2.13), where $C_{fade_{rt}}$ is how fast the cell decreases its capacity, and the C_{new} is the value at Begin of Life (BoL).

$$C_{res} = C_{fade_{rt}} \times N_{cycle} + C_{new} \tag{2.13}$$

Usually, SOH is 100% when the battery is new and 0% when the residual capacity C_{res} of the battery decreases under the 20% of the nominal capacity C_{new} meaning that the battery is at the end of its lifetime. So the state of health can be defined as (2.14) [22]

$$SOH_c = (1 - \frac{C_{new} - C_{res}}{0.2 \times C_{new}}) \times 100 \tag{2.14}$$

Resistance

The series resistance is strongly non linear, but for central SOC value it can be considered constant, for this reason it is possible to use an average value in this interval, to evaluate the trend of the resistance in function of the number of cycles.

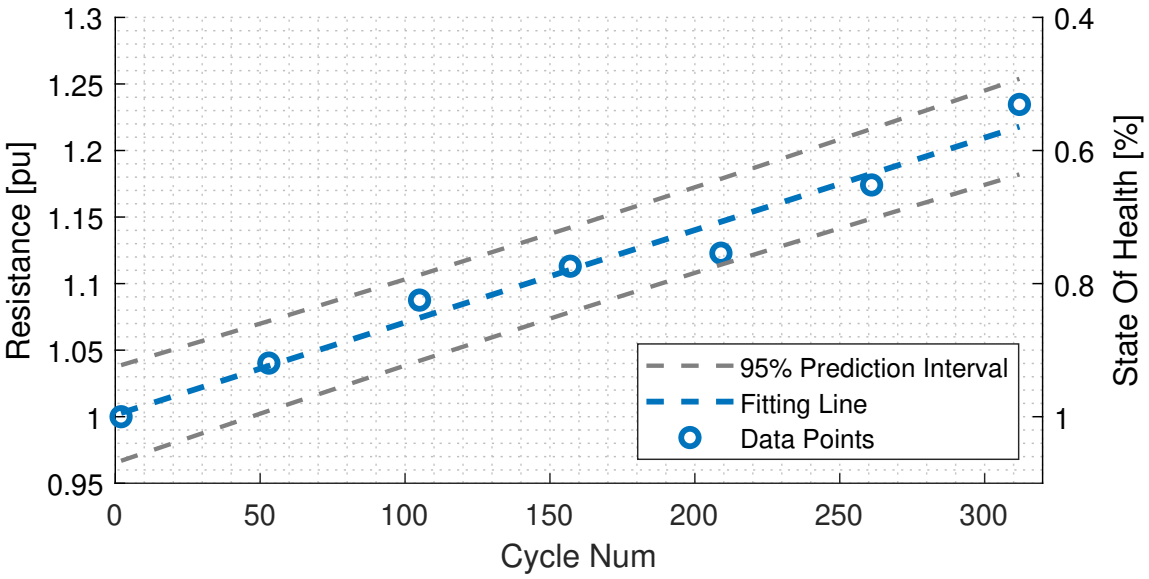

Figure 2.19: Resistance growth in 300 Cycle

Since capacity varies during aging the *SOC* calculation is done using the residual capacity and not the nominal capacity. Each test is normalized on the basis of the current capacity, and therefore the resistance is defined for each *SOC* value from 100% to 0%.

$$R_{act} = \frac{1}{N} \sum_{SOC=20\%}^{80\%} R_0(SOC) \tag{2.15}$$

Once obtained the values every 50 cycles you can see what the trend of resistance growth, and it is then possible to interpolate these data as a function of the number of cycles, as shown in Fig. 2.19. The "$\circ$" indicates the sample point get from the pulse discharge test, and the dashed line the interpolation of the point.

As for the capacitance loss, the increase of internal resistance presents a linear trend, therefore a linear equation is used in (2.16), where $R_{gr_{rt}}$ is how fast the internal resistance increases, and the R_{new} is the value at BoL.

$$R_{act} = R_{gr_{rt}} \times N_{cycle} + R_{new} \tag{2.16}$$

It is possible to define a different method to calculate the *SOH* based on the internal

resistance.

$$SOH_R = \frac{R_{eol} - R_{act}}{R_{eol} - R_{new}} \times 100 \tag{2.17}$$

Where R_{act} is the current average internal resistance mentioned in (2.15), R_{eol} is the internal resistance at the end of the lifetime $SOH = 0\%$, R_{new} is the internal resistance at the start of the lifetime $SOH = 100\%$. As a result, if R_{act}, R_{new} and R_{eol} can be estimated accurately, the SOH_R can be determined with enough accuracy using the definition.

2.2.3 Temperature-dependent parameters

In a battery the operating temperature is a fundamental quantity to be monitored because chemical reactions are strongly influenced by temperature. The higher the temperature of the battery, the faster the reactions, however the temperature cannot increase above certain values as because the reactions may become unstable, leading to thermal runaway phenomena. For this reason the electrical model of the cell must be able to model also this behavior too[75].

In Fig. 2.20 the voltage trend with different temperatures is shown and it is possible to see that the voltage drop is greater when the temperature is lower; for this reason it is possible to model this effect with an increase of internal resistance.

Similarly to what has been done for aging, a pulsed discharge is performed for each temperature, from which the model parameters will be extracted.

The series resistance is strongly non linear, but for central SOC value it can be considered constant, for this reason it is possible to use an average value in this interval, to evaluate the trend of the resistance in function of the temperature.

$$R_{act}(T) = \frac{1}{N} \sum_{SOC=20\%}^{80\%} R_0(SOC) \tag{2.18}$$

In the case of temperature, the resistance trend is non-linear, so a 4-degree polynomial function is used to represent this behavior.

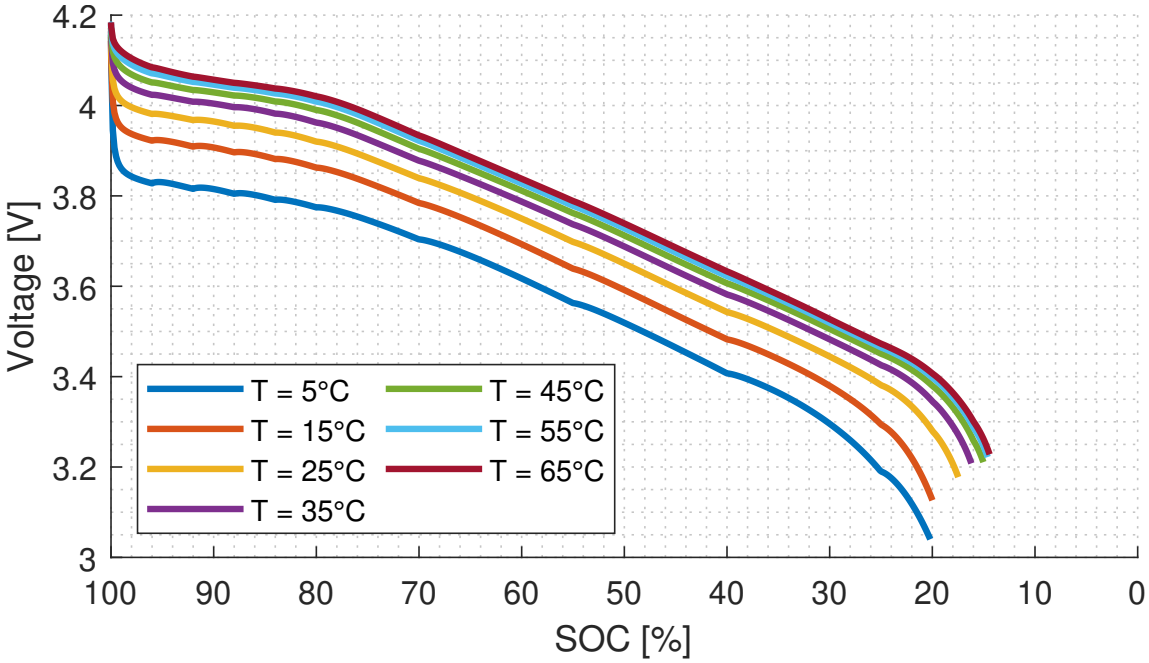

Figure 2.20: Discharge battery voltage, with different temperature

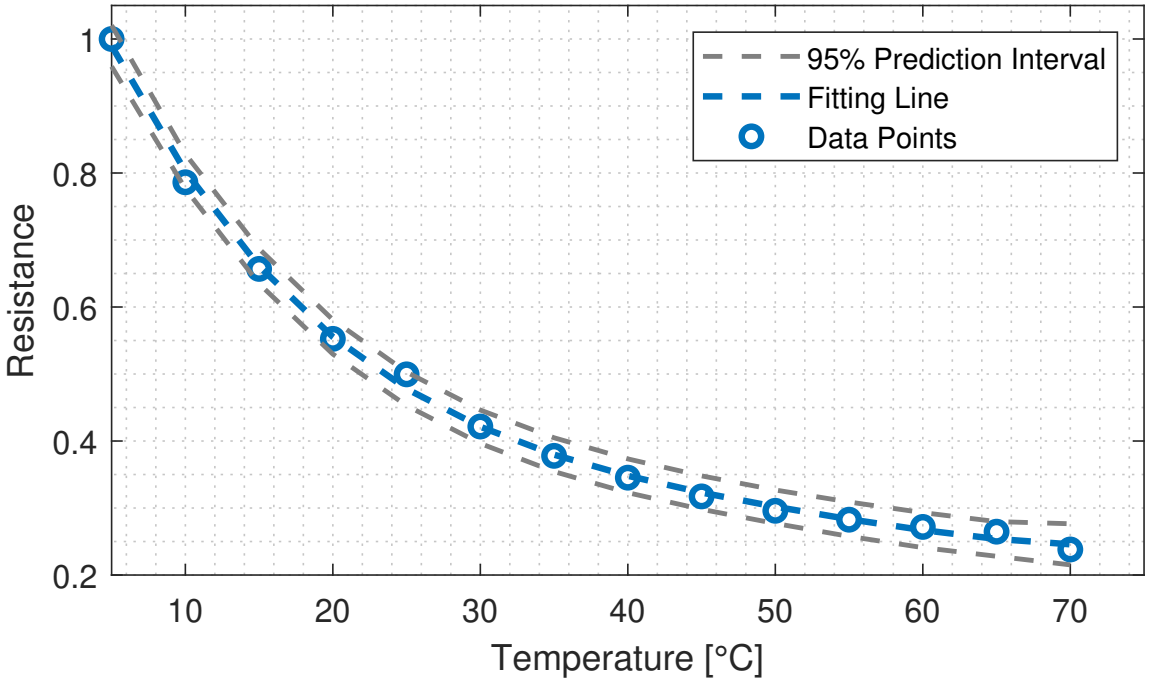

Figure 2.21: Resistance downturn versus temperature

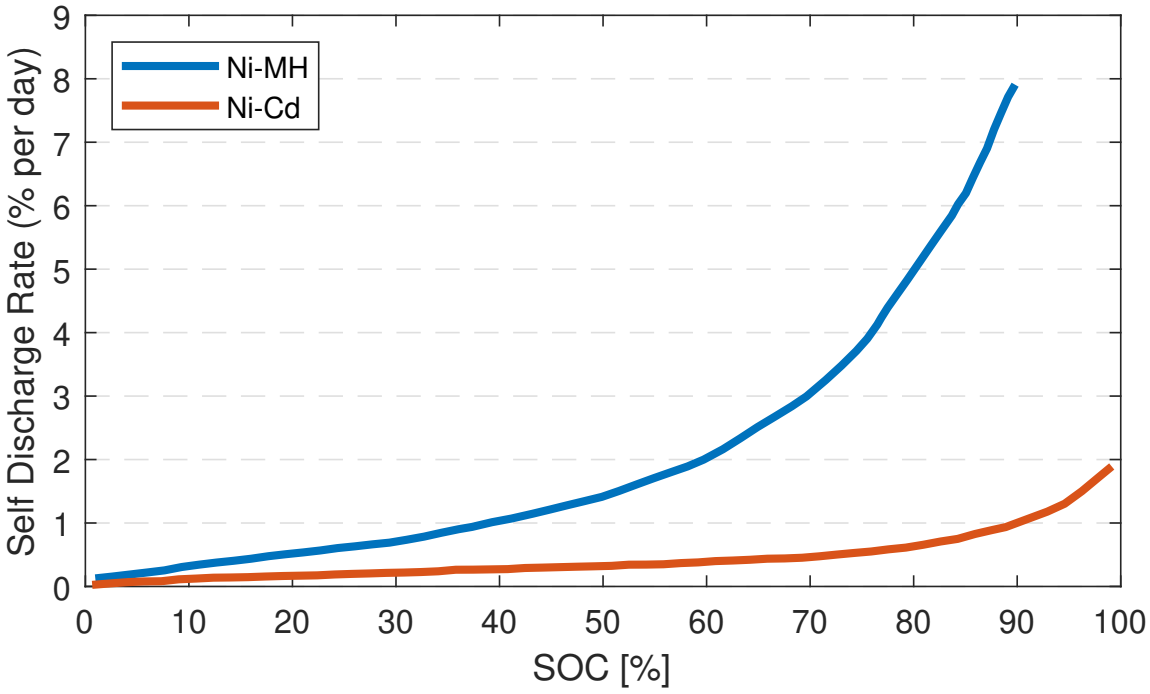

Figure 2.22: Self-discharge rates of Ni-MH and Ni-Cd vs SOC

2.2.4 Self discharge resistance

In chapter 1.5.1 is shown how self-discharge, discharges the battery when it is not connected to the load. The self-discharge rate of a lithium-ion battery is difficult and time-consuming to measure accurately because it is generally very low, C/50,000 or less (10^{-5} % per day), other battery types such as Ni-Cd and Ni-MH have higher self-discharge rates, as shown in Fig. 2.22. Lithium-ion cells have self-discharge rates that are also dependent on temperature, prior cycling history, time, and state-of-charge. [74]

Numerous methods for determining the self-discharge value have been presented in the literature, such as direct measure of the capacity loss or measure of the open circuit voltage and some other.

The first method is based on the difference between the charged and discharged capacitance. This method assumes that the Coulombic efficiency is 1. The cell is fully discharged and then recharged to a given *SOC*, and the capacity is measured. Then it is disconnected and kept at a controlled temperature for a fixed period, afterwards the bat-

tery is discharged, and the capacity is measured; the difference between these two values represents the capacity lose due to self-discharge.

The measurement is more accurate for higher values of the storage SOC, this is because the value of charged and discharged capacity is higher.

The second method is based on the $OCV - SOC$ relationship. In this case the assumption is that OCV trend doesn't change over time, and the voltage is measured with high accuracy. The voltage of the battery is measured 1 hour after the charging is finished, and after the storage period, the OCV is measured again, to obtain the SOC before and after the period. Once the ΔSOC is known, the capacity lost in the given period can be calculated. Due to non-linearity of the OCV, when the SOC is high or low using the $OCV - SOC$ relationship can cause errors.

At the end, with both methods, you can calculate the self-discharge resistance as the ratio between the battery voltage and the capacity lost over time.

$$R_s = \frac{mean(V_B(k), V_B(k+1))}{C_{lost}/\Delta t} \tag{2.19}$$

Where $V_B(k)$ and $V_B(k+1)$ are the voltage at the end of the charge and after the storage period, respectively, while ΔT, is the elapsed time between the two measurements. A common value for R_s ranges from 30kΩ to 150kΩ

2.2.5 Coulomb Efficiency

The life cycle of a Li-ion cell is not infinite because small fractions of cell components are consumed by parasitic reactions during each cycle possibly creating capacity fade, electrolyte oxidation, and so on [66]. Coulombic Efficiency (CE) can be a parameter to monitor the magnitude of side reactions. This value is very close to 1.

$$\eta_c = \frac{Q_d}{Q_c} = \frac{Charge_{Out}}{Charge_{In}} \tag{2.20}$$

For this reason, in order to correctly evaluate CE, very precise and accurate current measurements are required. The result is also influenced by the temperature at which the

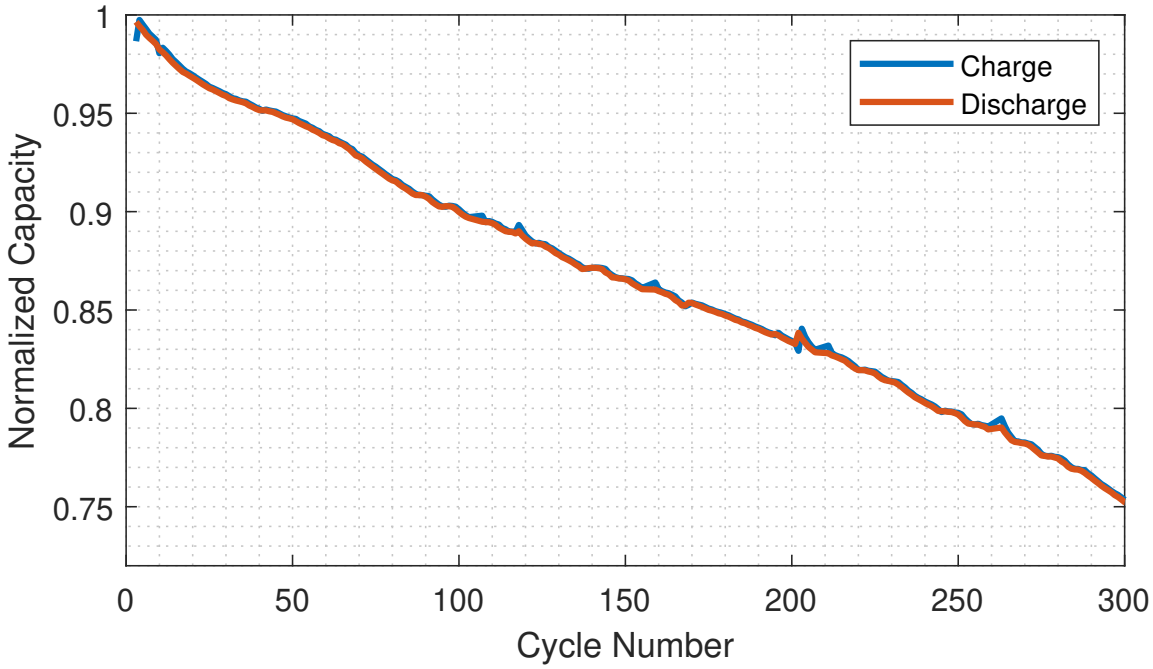

Figure 2.23: Capacity derating over number of cycle, charge and discharge

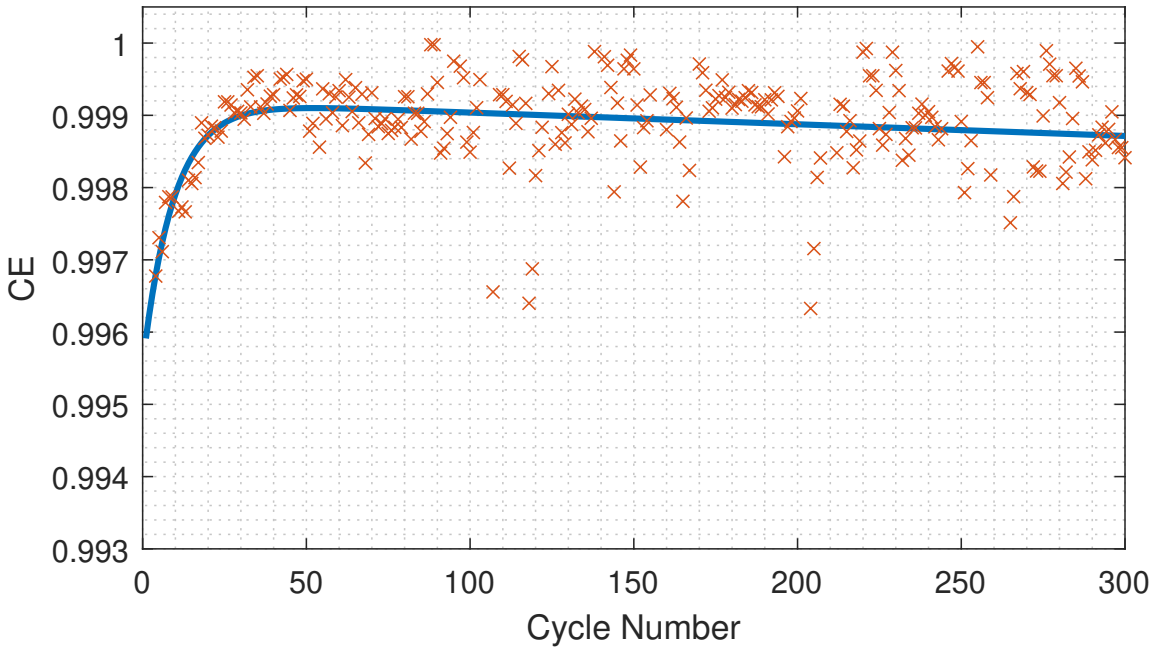

Figure 2.24: Coulombic efficiency over number of cycle

test is performed. In addition, the previous discharge can also influence the capacity value of the recharge.

It is also possible to investigate CE with respect to the degradation of battery capacity. CE of a cell at cycle k is defined as the ratio of the delivered capacity during discharge at cycle k, to the stored capacity during charge at the same cycle [28], the trend is shown in Fig. 2.24.

$$\eta_c(k) = \frac{C_{dsc}}{C_{chg}} = \frac{\int_0^{t_{dsc},k} i_B dt}{\int_0^{t_{chg},k} i_B dt} \tag{2.21}$$

2.2.6 Energy Efficiency

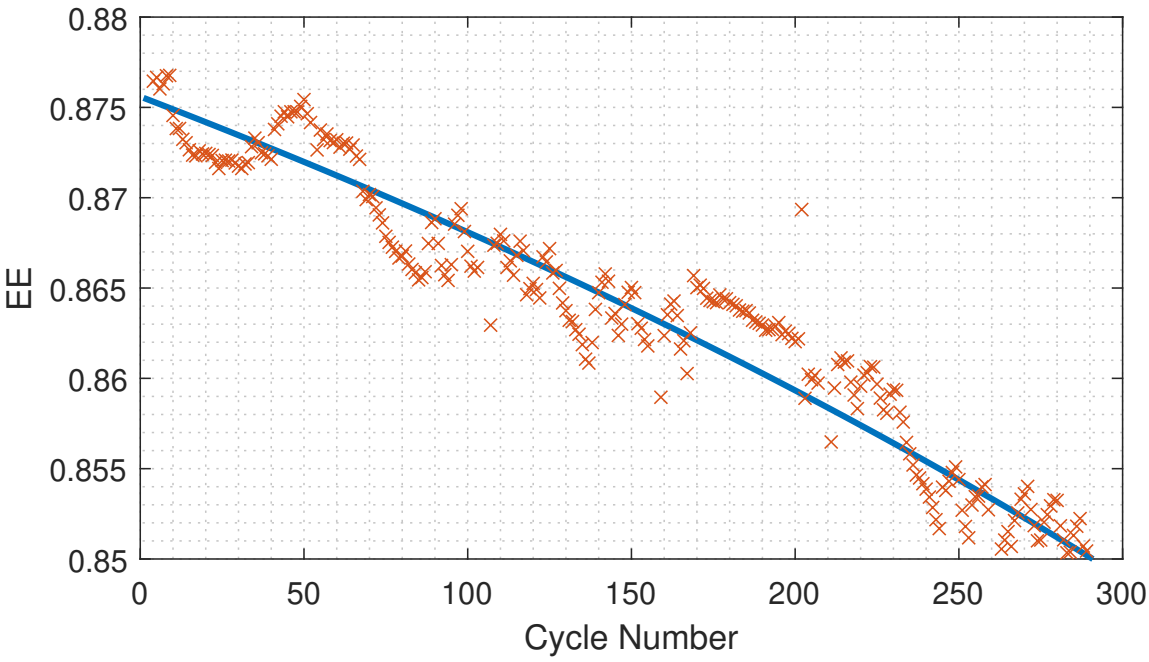

Figure 2.25: Energy efficiency derating over number of cycle, charge and discharge

Energy Efficiency (EE) represents the amount of chemical energy the battery can convert into electrical energy, i.e., it gives an indication of how much thermal energy is produced in the process. This aspect is fundamental to consider because the heat produced in the process must be dissipated.

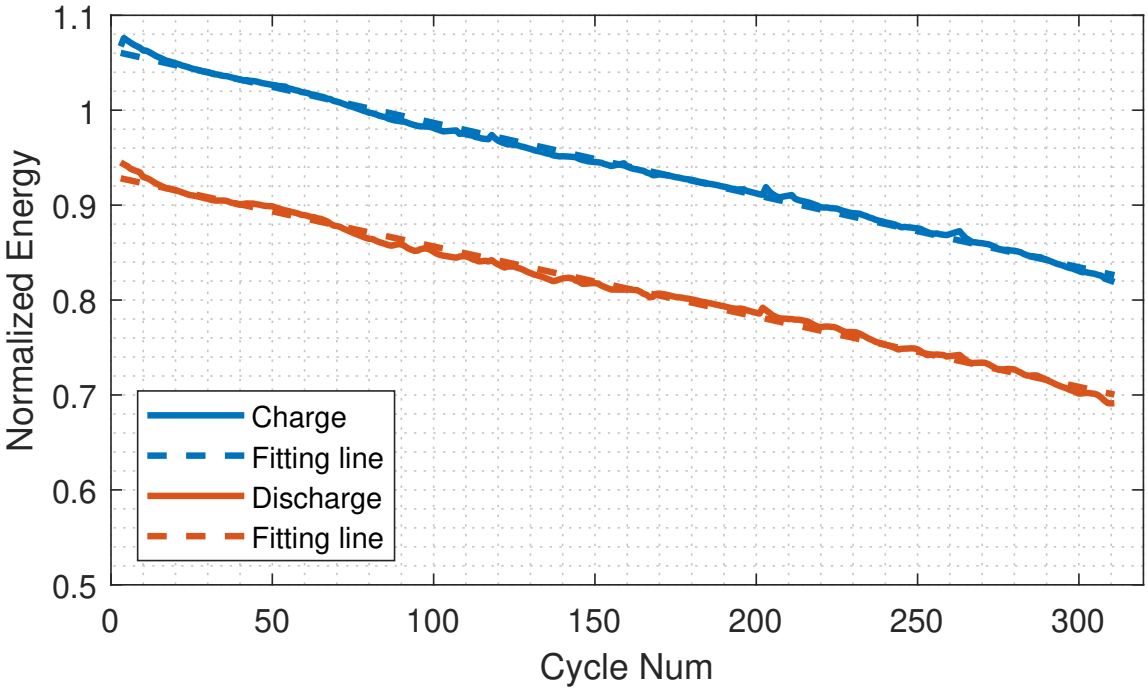

Figure 2.26: Energy efficiency over number of cycle

Through the modeling process the losses have been defined as the Joule losses produced by the cell, while the efficiency is defined as the ratio between the energy discharged and recharged.

Similarly to what has been done for the coulombic efficiency, it is possible to calculate the value of the energy efficiency as a function of the number of cycles.

$$\eta_e(k) = \frac{E_{dsc}}{E_{chg}} = \frac{\int_0^{t_{dsc},k} v_B \times i_B dt}{\int_0^{t_{chg},k} v_B \times i_B dt} \tag{2.22}$$

Due to the ageing the EE worsens, this means that in an old battery, applying the same cycle profile, the losses are higher, which will then be managed by the cooling system.

2.2.7 Ageing Model

Observing the chart in Fig. 2.27, it is possible to see how different types of use cause different ageing with the same number of Ah given by the battery. To realize a model that can calculate the state of health of the battery it is necessary to consider different factors,

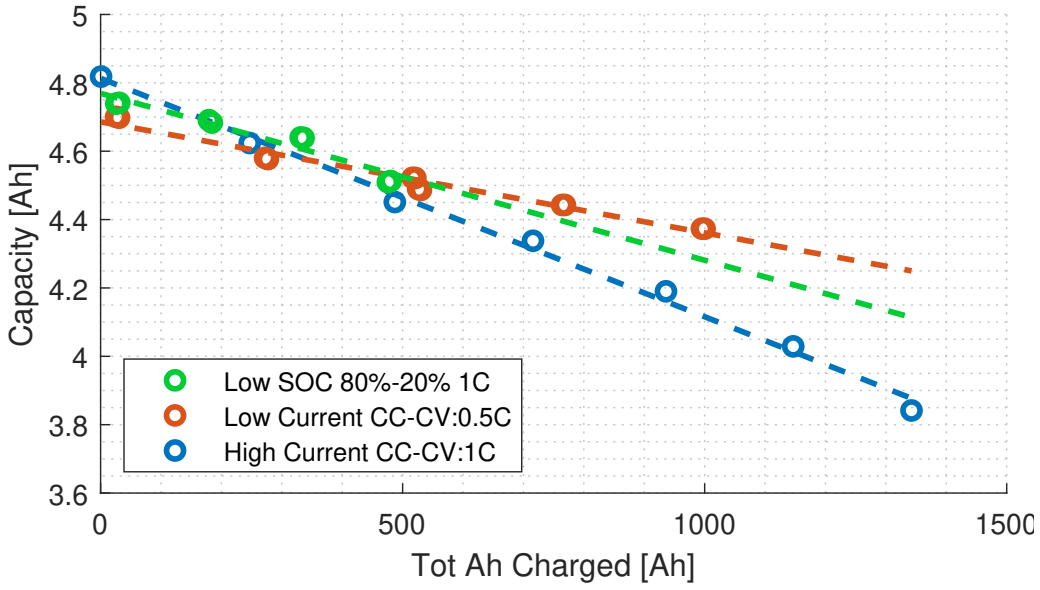

Figure 2.27: Capacity dreading vs battery usage

and their effect. To do this, the principle of superposition of effects is considered valid, so that each contribution can be considered separately. Three aspects that affect aging are considered in this analysis, the charge current, charge temperature, and *SOC* range of the cell. Three coefficients are therefore created, which are used to model these aspects, and their trends are shown below.

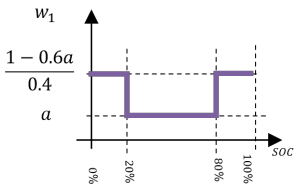

Figure 2.28: w_1 coefficient trend

SOC dependency A linear stroke function is defined for the charge state, which considers reduced aging in the middle phase of the *SOC*, between 20% and 80%, and increased aging for the remaining values. It is made as an assumption that for a full charge the aging produced is equal to one by definition.

$$\int_{0\%}^{100\%} w_1 dSOC \triangleq 1 \tag{2.23}$$

Temperature dependency To consider the effects of temperature on aging, the reference aging is considered to be at $25°C$. If the temperature is higher or lower than this value there is a greater deterioration of the battery. Therefore by definition the tempera-

ture coefficient is considered to be equal to 1 at a temperature of 25°C, and this point is also the minimum for the aging function.

$$\begin{cases} w_2(25°C) \triangleq 1 \\ \dot{w_2}(25°C) \triangleq 0 \end{cases} \tag{2.24}$$

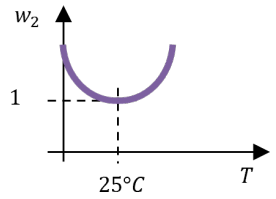

Figure 2.29: w_2 coefficient trend

Current dependency For SOH estimation, only the negative current, charging current, is considered. Moreover, it is assumed that below the value of 0.5C, the same effect on the battery is always produced, while above this values the aging has a polynomial trend as a function of current. Furthermore, charging at constant current equal to 0.5 C produces an aging equal to one.

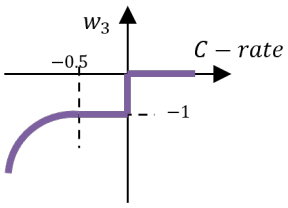

Figure 2.30: w_3 coefficient trend

$$\begin{cases} w_3(-0.5C) \triangleq 1 & for\ i_B < -0.5C \\ \dot{w_3}(-0.5C) \triangleq 1 & for\ i_B < -0.5C \\ w_3 \triangleq 0 & for\ i_B > 0 \\ w_3 \triangleq -1 & for\ -0.5 > i_B > 0 \end{cases} \tag{2.25}$$

The equation to calculate the value of SOH, given the values of voltage, temperature, SOC and current is as follows. Where the value of C_{tot} represents the total capacitance value discharged from the cell under standard test conditions, full cycles at constant current 0.5C at a temperature of 25°C, until 80% of the rated capacity is reached.

$$SOH_t = SOH_{t_0} - \int_{t_0}^{t} \frac{i_{B_k} W_1(SOC) W_2(T) W_3(i_B)}{C_{tot}} dt \tag{2.26}$$

In discrete time

$$SOH_{k+1} = SOH_k - \Delta t \times \frac{i_{B_k} W_1(SOC) W_2(T) W_3(i_B)}{C_{tot}} \tag{2.27}$$

2.2.8 Thermal Model Parameters

The values of R_1 and C_1 can be obtained from literature, or through experimental tests and depend on the type of cell and its internal composition, while the value of R_3 is related to the processes of conduction, convection, and irradiation, so it must be determined on the experimental conditions. In this chapter it will be explained how to obtain the thermal parameters of the cell through an experimental test.

The process of parameters determination can be divided into two steps, first the cell is heated to a certain temperature, and is constant so that the internal temperature is equal to the external one, then it is put at room temperature in free air. In this way it is possible to measure the temperature during the cooling process, and then observe the trend.

Using the equation (2.45), and because there is no current flowing in the cell, there are no losses $Q_{cell} = 0$. Furthermore, when the test starts, the internal temperature is equal to the temperature measured on the surface $T_{int} = T_{surf}$.

The cooling transient equation is described by:

$$Q_{R_1}(t) = \frac{T_{surf}(t_0) - T_{amb}(t_0)}{R_1 + R_3} e^{-\frac{t}{\tau_1}}$$

The surface temperature is:

$$\begin{aligned} T_{surf}(t) &= T_{amb} + Q_{R_1}(t) \times R_3 \\ &= T_{amb} + \left(\frac{T_{surf}(t_0) - T_{amb}(t_0)}{A} \right) e^{-\frac{t}{B}} \end{aligned} \tag{2.28}$$

where $A = R_1/R_3 + 1$, and $B = \tau_1$.

Once the values of A and B are determined, and on the bases of the test conditions the value of R_3 is fixed, it is possible to obtain the values of R_1 and C_1 as follow.

$$\begin{aligned} R_1 &= (A-1) \times R_3 \\ C_1 &= \frac{B}{A \times R_3} \end{aligned} \tag{2.29}$$

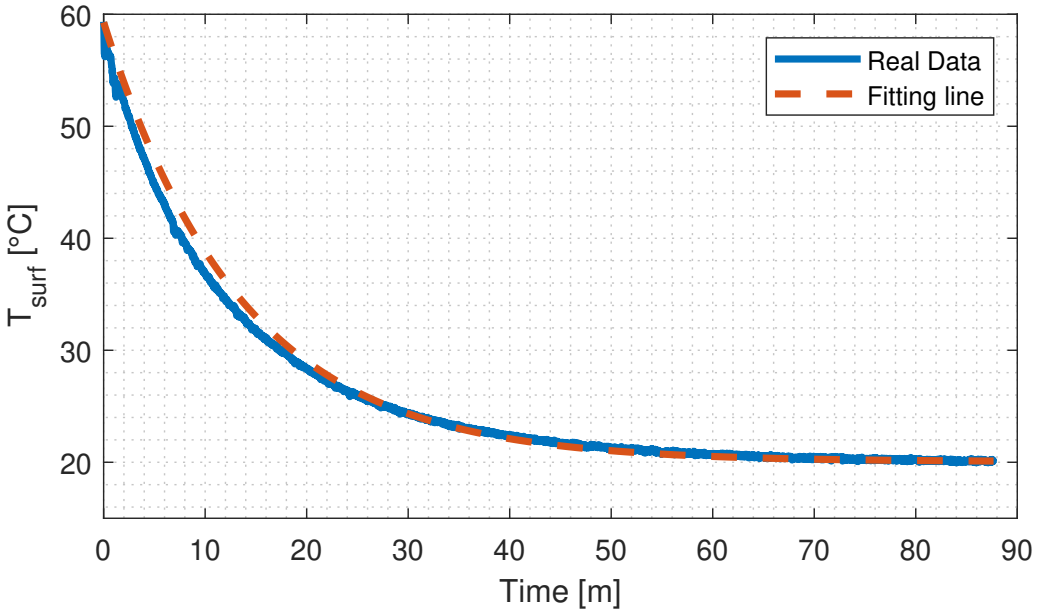

Figure 2.31: Thermal model parameters validations

2.3 Model Description

The proposed model is composed of a thermal electrical and state model. To represent the electrical behavior the single polarization (SP) is chosen, because it allows to reach a good accuracy on the voltage estimation and also to keep low the number of parameters to estimate, in according with [71, 61, 56]. For the Thermal model the radial representation [65] is used, this model cannot consider the power dissipation due to the pole of the cell, but this contribute is not so relevant for our porpoises. The state model is combined from two part the *SOC*, that is a standard coulomb counting *SOC* estimation and a *SOH*. The *SOH* method is a new field to investigate and this chapter shows a new methodology to calculate it.

2.3.1 State Model

The state model is used to estimate the states of the battery, two states have been defined, the *SOC* and the *SOH*. For the *SOC* calculation the Coulomb Counting [63] is used, for the health state a similar counting is done that takes into account the charge as a function of time, in this way the number of cycles is defined. the value C_{res} represents the cell capacitance value for a given *SOH* value, it allows to consider the decrease of the cell capacitance during aging. The Coulombic efficiency is represented by the term η_c while the ratio $\frac{R_s}{OCV}$ is used to represent the self-discharge current. Coulombic efficiency in a typical lithium-ion cell is around 99%, but this value can be different for different cell chemistry [38].

$$SOC_{k+1} = SOC_k - \Delta t \frac{\eta_c i_{B_k} + \frac{R_s}{OCV}}{C_{res}(SOH_{k-1})} \tag{2.30}$$

In (2.31) the proposed *SOH* estimation method is shown, the three weight W_1, W_2 e W_3, allow to consider three main aspects that can affect the ageing of the cell, the *SOC*, temperature and current. C_{Av} is the maximum cell capacity until the cell reaches *SOH* = 0%. This value is the sum of all discharged capacities in constant current discharge in

standard conditions where $T = 25°C$ in a full discharge test $(100\% - 0\%)$ form a new cell until it reach 80% of the nominal capacity.

$$SOH_{k+1} = SOH_k - \Delta t \times \frac{i_{B_k} W_1(SOC) W_2(T) W_3(I_B)}{C_{Av}} \tag{2.31}$$

It is possible to represent the state model as an electric circuit as shown in Fig. 1.27.

2.3.2 Cell Voltage

The electrical model is the Single Polarization (SP) Fig. 1.10, this model represents the right compromise between complexity and accuracy. In fact it allows to model fast transients, and also relaxation phases.

The poles voltage is described in (2.32)

$$\begin{aligned} v_{B_k} &= OCV(SOC_k) - V_{1_K} - R_0(SOC_k, T, SOH_k) \times i_{B_k} \\ &= OCV(SOC_k) - V_{1_K} - R_0(SOC_k) \times R_0(T) \times R_0(SOH_k) \times i_{B_k} \end{aligned} \tag{2.32}$$

The voltage V_1 on the capacitor can be obtained with the equation (1.12) written in discrete form. However, to keep down the complexity of the model, in order to have the possibility to deploy the model on a BMS, it is simplified using the first order Taylor approximation, in this way the (2.33) becomes (2.34).

$$V_{1_{K+1}} = V_{1_K} \times (e^{-\frac{\Delta t}{\tau_1(SOC_k)}}) + R_1(SOC_k, T_k) \times i_{B_k} \times (1 - e^{-\frac{\Delta t}{\tau_1(SOC_k)}}) \tag{2.33}$$

$$V_{1_{K+1}} = V_{1_K}(1 - \frac{\Delta t}{\tau_1(SOC_k)}) + R_1(SOC_k, T) \times i_{B_k} \times \frac{\Delta t}{\tau_1(SOC_k)} \tag{2.34}$$

.

To evaluate the battery losses in literature they are often calculated as $P_{loss} = i_B \times (V_B - OCV)$ [7] ; however, this equation is true only in average value, while the instantaneous value does not take into account the power exchanged on the capacitor.

The instantaneous value of the losses is therefore calculated as the sum of two contributions, the first related to R_0 and the second to R_1.

$$P_{loss} = R_0 \times i_B^2 + \frac{V_1^2}{R_1} \tag{2.35}$$

The parameters OCV, R_0, R_1, τ_1, V_c of the SP model Fig. 1.10 have been calculated as a function of SOC with a pulse discharge test following the procedure described in chapter 2.2. In order to characterize the cell as a function of temperature and state of health, tests have been carried out at different temperatures ($0°C$ to $70°C$ with ΔT = $5°C$), and at different number of cycles (0-300). The number of cycles at the end of life has been chosen to be 300, in accordance with the manufacturer's declaration; moreover, once 300 cycles have been reached, the residual capacity is less than 80 %, therefore SOH can be considered = 0%

SOC dependency

The parameters of the SP model, calculated using experimental test data, are stored in look-up tables as functions of the SOC, and subsequently, more useful interpolation functions are determined.

The OCV curve has been represented using the very reliable function proposed by [72].

$$\begin{aligned} OCV(SOC) =& a + bSOC + cSOC^2 + \frac{d}{SOC} + \\ &+ e\ln(SOC) + f\ln(1 - SOC) \end{aligned} \tag{2.36}$$

The resistances, R_0 are represented with the following algebraic functions:

$$\begin{aligned} R_0(SOC) =& x_1 SOC^{x_2} + x_3 logSOC + x_4 SOC^3 + \\ &+ x_5 SOC^2 + x_6 SOC + x_7 \end{aligned} \tag{2.37}$$

The resistances, R_1 are represented with the following polynomial functions:

$$\begin{aligned} R_1(SOC) =& x_1 SOC^{x_2} + x_3 logSOC + x_4 SOC^3 + \\ &+ x_5 SOC^2 + x_6 SOC + x_7 \end{aligned} \tag{2.38}$$

The time constant can be represented as a constant.

$$\tau_1(SOC) = x_1 \tag{2.39}$$

The proposed model is intended to represent the behavior of the battery under load, and therefore the self-discharge phenomenon is not very influential, moreover for lithium batteries the value of self-discharge resistance is very high. Consequently for these two reasons, the contribution is negligible, i.e. the value of R can be set to infinity.

$$R_s(SOC) = inf \tag{2.40}$$

Ageing dependency

The major effect caused by aging is the decrease of the available capacity of the cell and a growing of the internal resistance, as seen in the previous chapters, it is possible to mathematically describe those as a function of *SOH* using a polynomial equation. Depending on cell type this trend can be linear or non linear.

$$C_p(SOH) = y_1 SOH^2 + y_2 SOH \tag{2.41}$$

The ageing also cause an increment of the resistance in particular the series resistance this phenomenon is model by a coefficient that will be multiplied by the value of the resistance R_0, this value is always greater than 1.

$$R_0(SOH) = y_1 SOH^2 + y_2 SOH \tag{2.42}$$

Thermal dependency

The temperature of the battery affects the parameters of the electrical model, to consider this effect, coefficients are introduced for the two resistance values. The coefficients are obtained as functions of the four degrees and will then be multiplied by the resistance

value obtained from the previous calculation. All other parameters are not affected by temperature, these values are always greater than 1.

$$R_0(T) = z_1T^4 + z_2T^3 + z_3T^2 + z_4T + z_5 \tag{2.43}$$

$$R_1(T) = z_1T^4 + z_2T^3 + z_3T^2 + z_4T + z_5 \tag{2.44}$$

2.3.3 Thermal model

Thermal modeling is particularly complicated because there are hundreds of layers of different materials with different thermal conductivity inside the cell, and heat is created in each inner layer. An example of an accurate thermal model can be found at [33], however, the complexity involved is very high. For simplicity therefore, the thermal model used to represent the cell behavior is the radial model, proposed by [65]. This model considers the power exchanged by the cell in the radial direction only, neglecting the contributions given by the poles. A further simplification is to consider concentrated losses assuming that the whole power is generated at the center of the cell.

Starting from (1.35) it is possible to build the lumped thermal parameter model of the cell.

In Fig. 2.32 the thermal equivalent circuit of the cell is shown. Where the resistance R_1 represents the thermal conduction between the cell core and the surface, while R_3 represents the conductance towards the environment. C_1 models the thermal capacity of the cell. Using the equation (2.45), it is possible to calculate the heat transferred from the cell to the environment.

$$C_1\dot{T_{int}} = Q_{cell} + \frac{T_{amb} - T_{int}}{R_1 + R_3}$$

$$Q_{R_1} = \frac{T_{int} - T_{amb}}{R_1 + R_3}$$

It is possible to get T_{int}

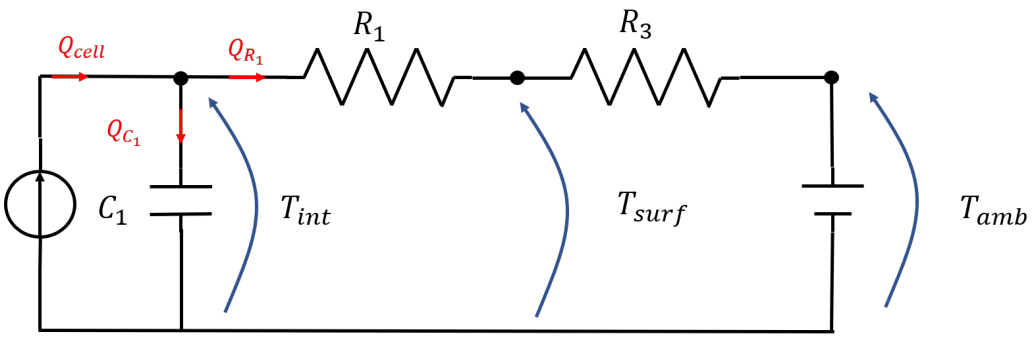

Figure 2.32: Equivalent radial thermal model

$$T_{int} = (R_1 + R_3)Q_{R_1} + T_{amb}$$

Deriving the equation

$$\dot{T_{int}} = (R_1 + R_3)\frac{dQ_{R_1}}{dt}$$

replacing

$$C_1(R_1 + R_3)\frac{dQ_{R_1}}{dt} = Q_{cell} - Q_{R_1}$$

t, where τ_1 is the thermal time constant and is defined as:

$$\tau_1 = C_1 \times (R_1 + R_3)$$

obtaining the differential equation related to the power transferred from the cell to the environment

$$\frac{dQ_{R_1}}{dt} + \frac{Q_{R_1}}{\tau_1} = \frac{Q_{cell}}{\tau_1}$$

The solution of the differential equation is:

$$Q_{R_1}(t) = Q_{R_1}(t_0)e^{-\frac{t}{\tau_1}} + Q_{cell}(1 - e^{-\frac{t}{\tau_1}}) \tag{2.45}$$

finally, the result using discrete-time notation is:

$$Q_{R_1}(k) = Q_{R_1}(k-1)e^{-\frac{\Delta t}{\tau_1}} + Q_{cell}(k)(1 - e^{-\frac{\Delta t}{\tau_1}}) \tag{2.46}$$

To keep the complexity of the system low, it is used the first order Taylor approximation on the equation (2.46), so the heat transferred from the cell to the environment of the thermal model in the Fig. 2.32 is expressed by:

$$Q_{R_1}(k) = Q_{R_1}(k-1)(1-\frac{\Delta t}{\tau_1}) + Q_{cell}(k)\frac{\Delta t}{\tau_1} \tag{2.47}$$

Once obtained the equation (2.47) it is possible to calculate the temperature inside and on the surface of the cell as:

$$\begin{cases} T_{surf} = T_{amb} + R_3 \times Q_{R_{k+1}} \\ T_{int} = T_{amb} + (R_1 + R_3) \times Q_{R_{k+1}} \end{cases} \tag{2.48}$$

2.4 Implementation

In this thesis three implementations of the battery model are presented, realized with three different purposes. The model was first developed using MATLAB® , which allows a fast-prototyping approach, aiming to validate the model comparing it with experimental data. Subsequently, the model has been rewritten in SIMULINK® , that is user friendly and allows to integrate the battery with other components such as an engine, or vehicle model. Moreover, using the tool "Embedded Coder", it is possible to generate the C code starting from the scheme, loading the battery model directly on the BMS. In this way the BMS can perform predictive control strategy based on the model. In the last phase the model was brought on PYTHON^{TM} to generate a large amount of data, to be used in conjunction with data from laboratory tests for neural networks training.

2.4.1 Matlab environment

The programming language Matlab is an excellent development environment, which allows to import the results of experimental tests, and perform complex data processing, and also create comparative figure quickly.

The model is represented as a graph in Fig. 2.33, in which all the steps that make up the algorithm are reported.

During the initialization phase, the vector with the reference current and the temperature at which the test was performed on the real cell is loaded by the program, moreover the initial conditions for *SOC*, *SOH* initial cell temperature, and cell voltage are assigned.

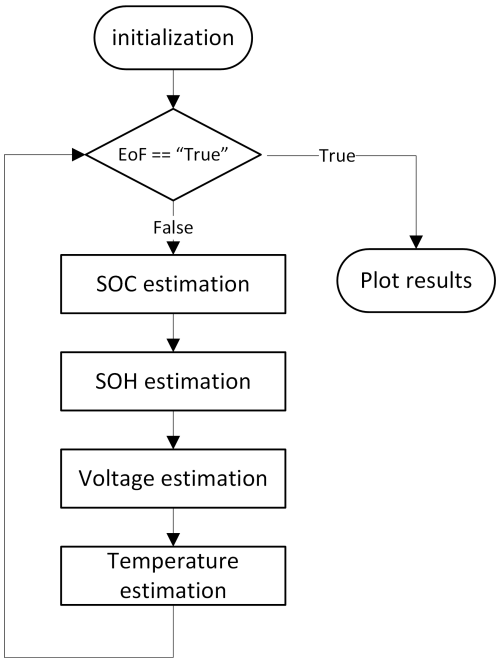

Figure 2.33: Flowchart of MATLAB® model

Once the initialization is performed the model is composed of four main models, estimation of SOC, SOH, V_b, T_{cel} which are calculated successively until the file is terminated,

i.e. until the end of the current vector.

When the file is terminated, the comparison of the values measured in the real battery against the values estimated by the model is shown.

As for the four models, they have been realized by Matlab functions, while for all parameters data by Matlab "function handle" have been used, so to represent functions. By this way at each interaction it is possible to calculate the value of the parameters as a function of the other values.

2.4.2 Simulink Environment

In Simulink the four main functions, also seen in the Matlab environment are implemented; moreover a BMS has been implemented to monitor the key aspects of the simulation, to emulate the real system. The BMS model verifies that the battery reflects the constraints provided by the manufacturer in terms of temperatures, voltages, and currents. To facilitate the use of the model it has been associated an image characterizing each function..

Input Output The subsystem has a summary interface that shows the most important characteristics of the chosen model, the inputs are the current and the ambient temperature, if the simulation describes only electrical behavior the battery temperature is also required.

The outputs are voltage and temperature of the battery, state of charge and health, and the battery losses.

A mask has been created for easy access to the main aspects of the battery to be emulated directly from a graphical interface. The GUI is composed of two pages, in the first page there are all the aspects related to the configuration of the battery Fig. 2.36(a), in the second there are the aspects related to the thermal model Fig. 2.36(b).

Pack Parameters In the first page it is possible to establish the pack configuration, choosing the number of cells in series and number of cells in parallel, it is possible to choose the cell state, in terms of SOC, and SOH, and the cell efficiency can be set in terms of coulombic efficiency. Also, the type of cell used can be set on the base of a dataset of

tested cells.

Thermal Parameters In the second page it is possible to choose the type of model used among radial model, radial model with plastic, or keep the temperature constant. In the future it is expected the possibility to also implement the complete model. The temperature of the battery can be given as a constant, or as a vector. On the last part of the mask the parameters of the thermal model can be set, this part of the mask will be different depending on the previously chosen model.

2.4.3 Python Environment

The Python programming language is ideal for developing algorithms based on machine learning, it is also more efficient than Matlab, for these reasons, the model was also ported on this programming environment.

In this model there is a further step forward, compared to the two previous models, a battery charger which allows to recharge the battery when the *SOC* is below settled value, so the model can simulate battery ageing cycle.

Each simulation step takes in input a current, the room temperature. The model inputs current and temperature are generated using the random walk algorithm [15], by this way it is possible to emulate the battery behavior under real use conditions. All the output generated data are stored as a ".csv" file to be used later.

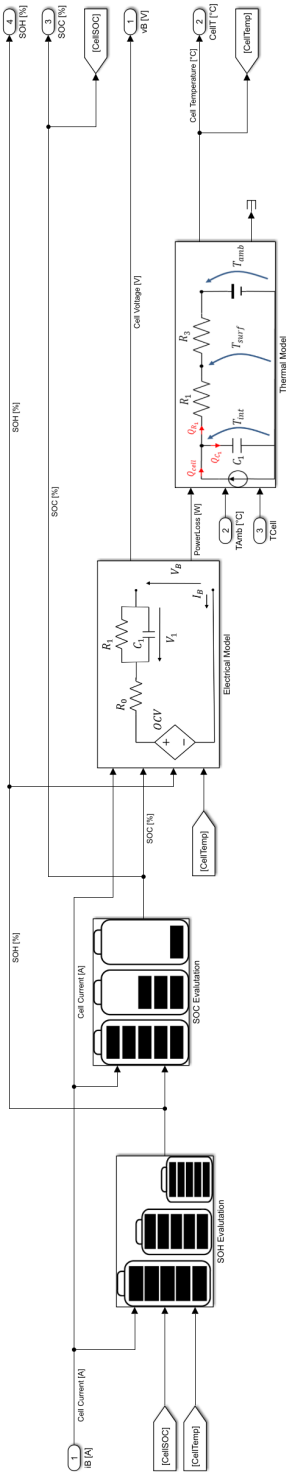

Figure 2.34: Simulink model scheme

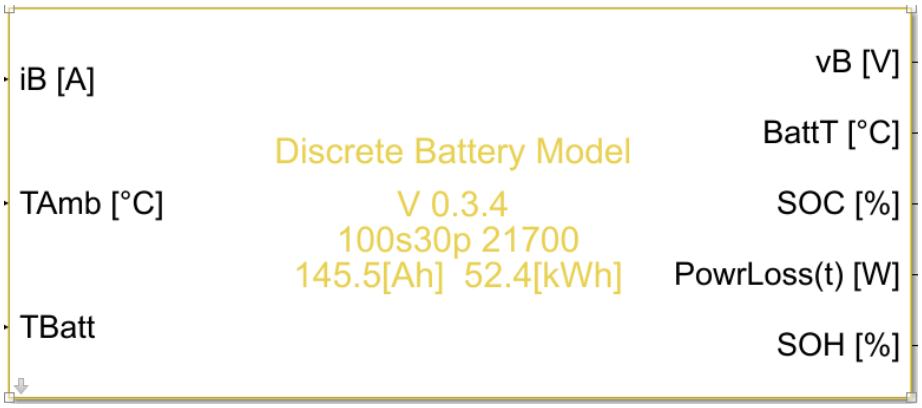

Figure 2.35: Simulink Model Scheme

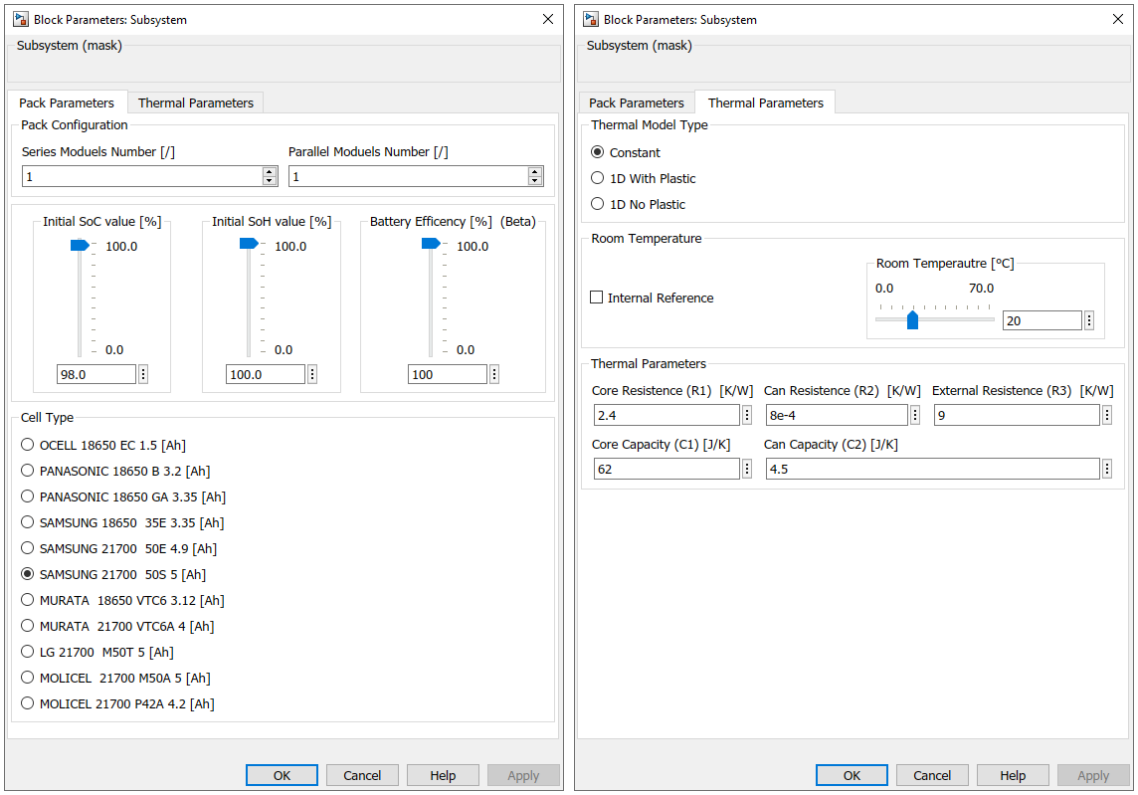

(a) Page1 (b) Page2

Figure 2.36: Comparison between two different chemistry

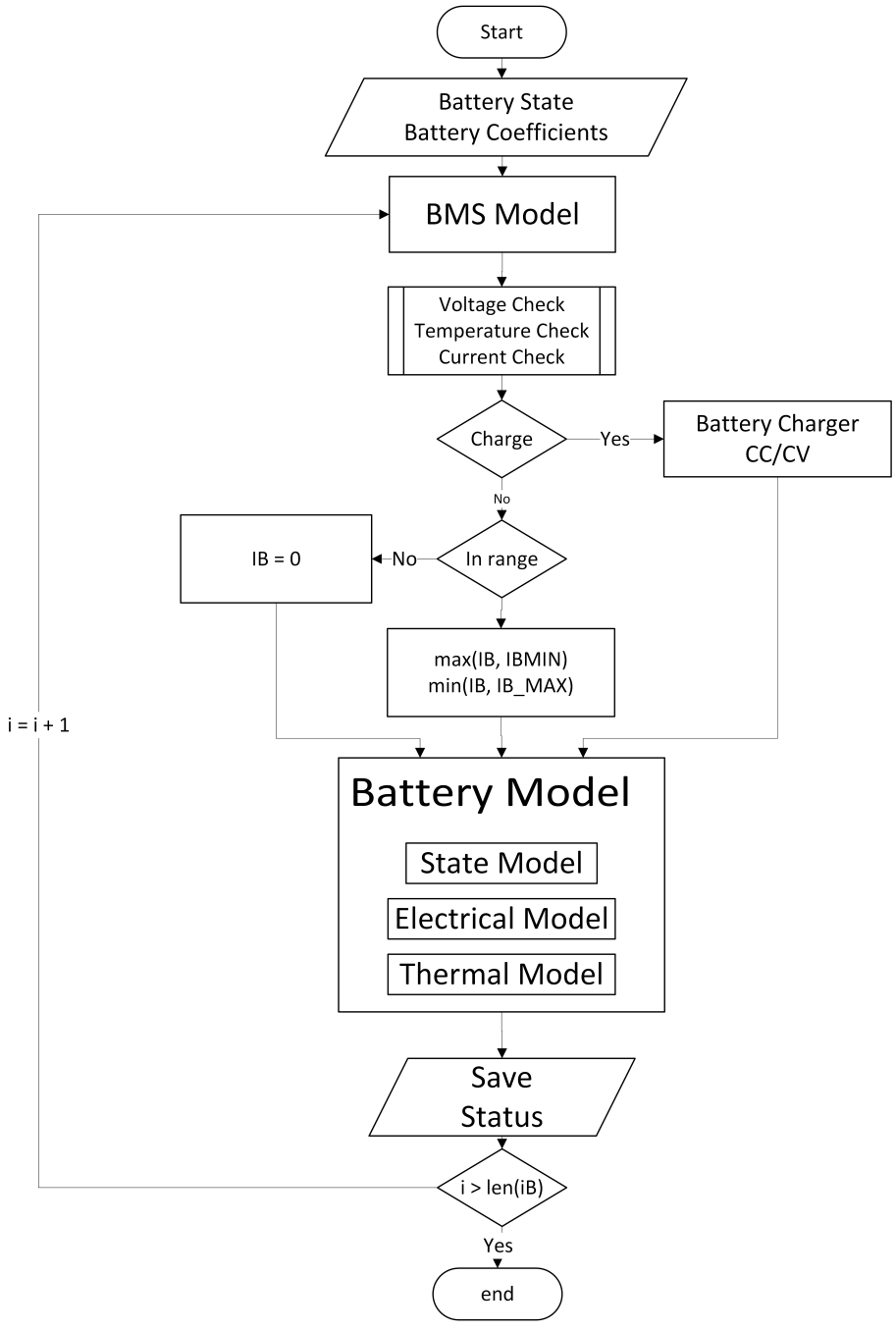

Figure 2.37: Flowchart of python model

2.5 Model Results

In this section, an example of implementation in a Simulink environment will be shown. The model will then be compared with laboratory tests to evaluate its performance.

The test is carried out on a Molicel INR21700P42A, this cell is a high-power cell with 4.2Ah. This cell has a low internal resistance, and it's rated for more than 1C current.

To compare the results the mean error (2.49) and maximum error (2.50) are calculated between the measured voltage and the real voltage.

$$V_{Mean} = \frac{\frac{1}{n}\sum(v_{B_{real}} - \hat{v}_{B_{EKF}})}{v_{nom}} \tag{2.49}$$

$$V_{Max} = \frac{MAX|v_{B_{real}} - \hat{v}_{B_{EKF}}|}{v_{nom}} \tag{2.50}$$

To evaluate the performance of the model, two series of tests were carried out. In the first series, the tests were conducted keeping the temperature of the cell constant, so it was possible to decouple the thermal model from the electrical one. The second series of tests were carried out in free air, to evaluate the performance of the thermal model, by following the temperature of the cell.

out of the total of eight tests performed, four were done on a new cell and four were done on a cell with a 10% SOH. Two tests for each cell were done at constant temperature of $25°C$ and $50°C$ and the rest were done in free air. All tests were carried out with the same current profile starting from a fully charge cell until the cut-off voltage. The free air tests reached the maximum allowed temperature, and consequently a pause was made to allow the cell to cool down.

The implementation was done in Simulink environment, a Matlab tool which allows to create and test models In Fig. 2.34 the implementation scheme is shown.

To validate the model, the measurement of current and temperature during the laboratory tests were used, as inputs for the Simulink model. Then the outputs of the Simulink model were compared, with voltage, temperature, and SOC measured in the test phase. As

Table 2.2: Test performance comparison

Temp. ° C	SOH = 100 %			SOH = 10 %		
	Test	ME (2.49)	MAE (2.50)	Test	ME(2.49)	MAE(2.50)
Const: 25	1	-0.23 %	2.51 %	2	-0.67 %	2.06 %
Const: 50	3	-0.11 %	3.14 %	4	0.98 %	4.85 %
Environment 25	5	-0.94 %	2.12 %	6	0.21 %	2.67 %
Environment 25	7	-0.37 %	2.31 %	8	0.10 %	2.46 %

for the *SOC*, calculations were carried out using the integration of the current and normalizing for the value of capacity obtained in the test, because the cell has always reached the cut-off voltage and consequently the capacity extracted in each test is always the one available in that condition.

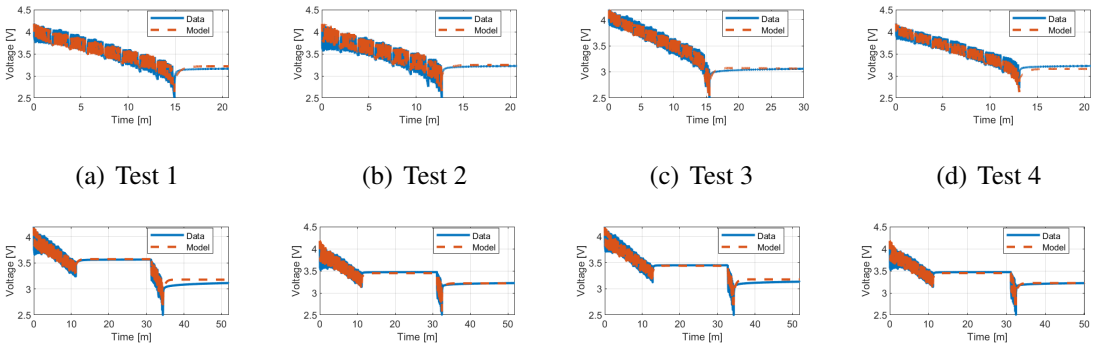

(a) Test 1 (b) Test 2 (c) Test 3 (d) Test 4

(e) Test 5 (f) Test 6 (g) Test 7 (h) Test 8

Figure 2.38: Tests results, voltage comparison

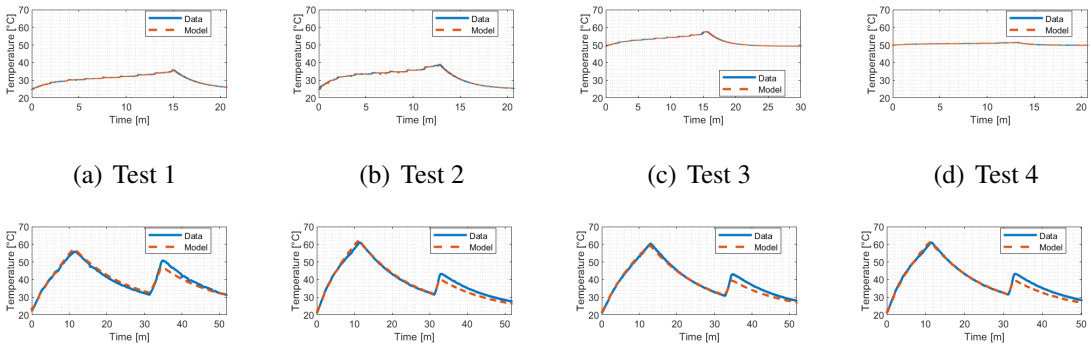

(a) Test 1 (b) Test 2 (c) Test 3 (d) Test 4

(e) Test 5 (f) Test 6 (g) Test 7 (h) Test 8

Figure 2.39: Tests results, temperature comparison

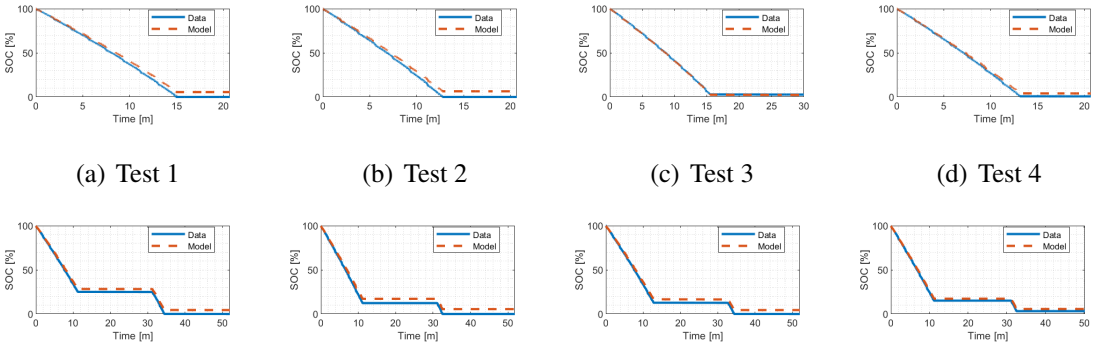

(a) Test 1 (b) Test 2 (c) Test 3 (d) Test 4

(e) Test 5 (f) Test 6 (g) Test 7 (h) Test 8

Figure 2.40: Tests results, SOC comparison

From the tests performed at constant temperature it is possible to evaluate the accuracy of the electrical model of the cell, and the results show that the model can follow very well the voltage measured in the laboratory tests. Tests made in free air are used to evaluate the interaction between the electrical model and the thermal model, and how the parameters are mutually influenced; for this test too, it is seen that the model always reaches very good results on the estimation of the battery voltage. The temperature trend on the cell surface is in line with that predicted by the model, and this is due to a correct estimation of the internal losses of the cell, which is a fundamental information when sizing a cooling system. Aged cell tests show how the variation of parameters due to aging in the real cell is also traced by the model, showing only a slight difference about the state of charge that however is also found in the new cell test, and is not entirely attributable to the model but also to its definition. In all tests the open circuit voltage is overlapping with the open circuit voltage measured on the real cell, confirming that the final *SOC* of the model and the real cell are the same. The error obtained on the voltage estimation is less than 1% for all tests performed, which is very promising also in comparison with the literature on the subject.

3 State Estimation

Filter Methods The Kalman Filter (KF), in all its forms, is an excellent method for determining the states of systems, and even of batteries. This method has good accuracy and reliability, even compared to other methods [35], such as the Particle Filter [50]. For this reason, in literature there are many examples of application of KF algorithms for *SOC* estimation [1, 32, 45, 59].

The *SOH* cannot be directly estimated by using the KF, but it can be derived from the precise estimation of the batteries parameters, such as the internal resistance and capacitance [3, 24, 62].

In the literature more filters are often used simultaneously, the most popular method is that explained by [35], which uses the Dual Extended Kalman Filter. A variation of this method is presented in [3], their proposed method is called Dual Fractional Order Extended Kalman Filter. Other authors propose different filters used together as [34], combining the use of the H-Infinite Filter for the estimation of *SOC* and the UKF for the estimation of cell parameters.

Table 3.1: Filter based method comparison

State estimator	**Model Type**	**Parameters Distribution**	**Computational Cost**
Kalman Filter KF	Linear	Gaussian	Low
Extended Kalman Filter EKF	Locally Linear	Gaussian	Low Medium
Dual Extended Kalman Filter DEKF	Locally Linear	Gaussian	Medium
Unscented Kalman Filter UKF	Non Linear	Gaussian	Medium
Particle Filter PF	Non Linear	Non Gaussian	High

Long Short Therm Memory The strength of these methods is the ability to solve strongly non-linear problems, the computing power required once the model has been trained is much lower than that required in model based methods [21]. On the other hand the great quantity of data necessary for the training makes very difficult its use in the real applications.

As all the neural network algorithms, they can provide high computational speed, but it is not clear yet how to train them effectively. Moreover, a common issue is again the fact that only the internal resistance R_0 can be estimated, with the strong approximation to keep the other parameters constant. Hypothesis that might be not acceptable to evaluate the *SOH* during real usage of the battery.

3.1 Long short therm memory for SOC estimation

In this section, a methodology for determining *SOC* based on neural networks will be presented. The technique used is based on recurrent neural networks (RNNs). To perform the neural network training, two datasets were used, that will be presented later.

RNNs are a type of neural networks that store informations over time. RNNs have connections within the layers that form cyclic directed graphs. This allows the neural networks to have a memory, represented in form of the state. Information from the previous state can be used as input for the next state, this allows the network to consider the relationship between current and past information.

This type of neural network is very well suited for battery state estimation, an example of the architecture of a RNN for *SOC* estimation is shown in Fig. 3.2. The input vector at time t contains the measurable values of the battery such as voltage, current, and temperature, and is denoted as $Input_t$, h_t represents the variable stored at time t while the *SOC* value represents the output.

3.1.1 Used dataset

The two datasets are briefly introduced in this section. The first is a database that has been created over these last years and has been made public available with the the publication of the related article [10], while the second is a public database that has been conducted on LG 18650 cells.

UNIBO Powertools dataset

The UNIBO Powertools dataset was created in collaboration with a local company that produces battery powered equipment. The tests that have been conducted are standard life tests, to compare cells from different manufacturers. The dataset consists of 27 different cells, and is summarized in Tab. 3.2.

The dataset is mixed and contains cells from different manufacturers, different nominal cell capacities, and all cycles end at the end of cell life. Therefore, it is possible to test the

network for different *SOH*, as well as validate the *SOC* estimation method for capacities other than nominal capacities. All the tests are conducted at room temperature, and they were conducted using the procedure shown in Fig. 3.1.

The ageing procedure consists of a charge with a Constant Current-Constant Voltage (CC-CV) at 1.8 A and 4.2V (100 mA cut-off), and a discharge with a Constant Current until cut-off voltage (2.5 V). The sampling time in this procedure is 10 seconds.

After every 100 cycles, the capacity is measured by a standard test, CC-CV 1 A 4.2 V (100 mA cut-off) and discharge CC 0.1 A 2.5 V, and thanks to this test it is also possible to determine the parameters of the model.

Three types of tests have been conducted:

1. The **standard test**, where the battery was discharged at 5 A current in main cycles;
2. The **high current test**, where the battery was discharged at 8 A current in main cycles;
3. The **preconditioned test**, where the battery cells are stored at 45°*C* environment for 90 days before conducting the test.

Table 3.2: UNIBO Powertools dataset summary

Test type	Nominal capacity	Cell amount
Standard	4.0Ah	2
	3.0Ah	4
	2.85Ah	4
	2.0Ah	6
High current	3.0Ah	3
	2.85Ah	2
Preconditioned	3.0Ah	5

LG 18650HG2 Li-ion Battery Data

The public LG 18650HG2 Li-ion Battery dataset, published by [11], was obtained from Mendeley data. In the dataset, a series of tests were performed under six different temper-

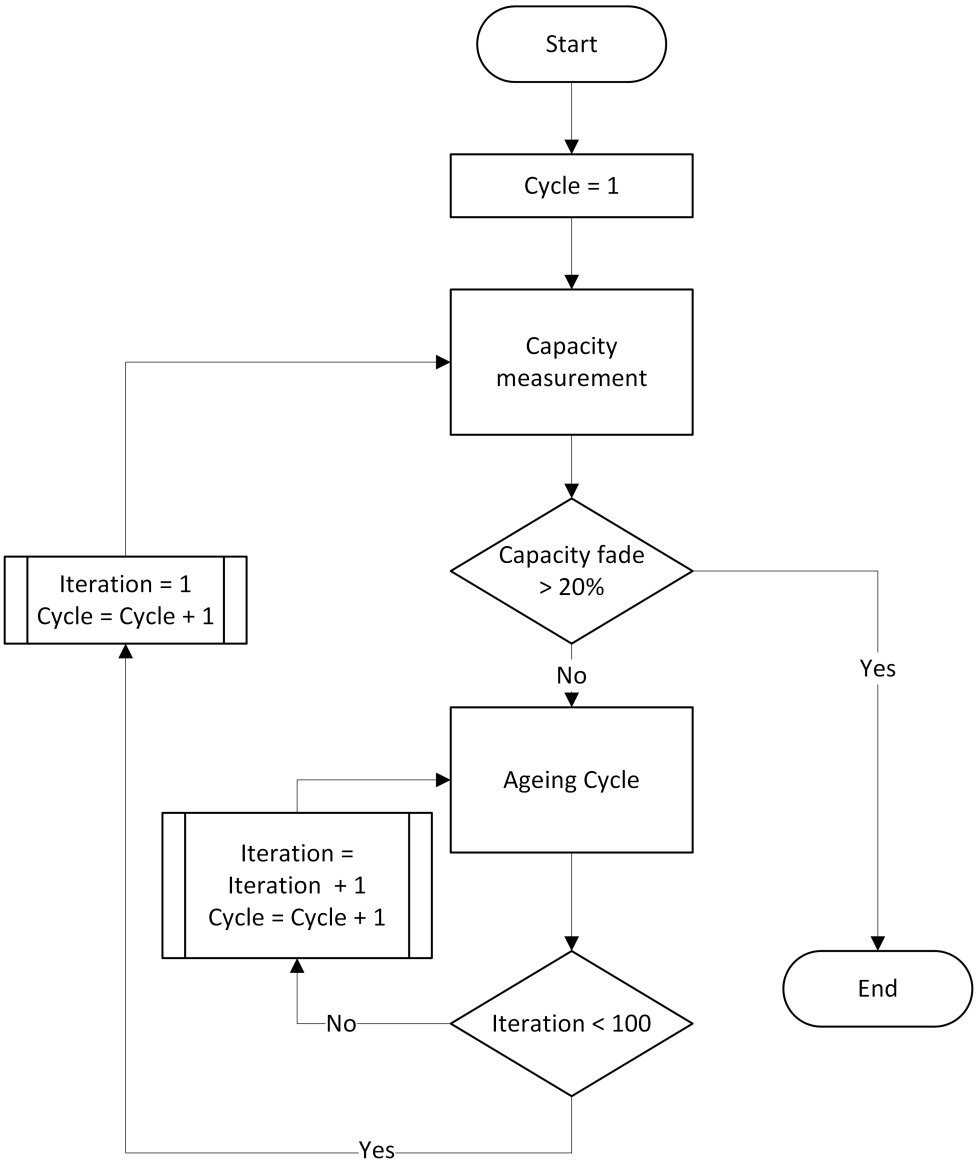

Figure 3.1: Flowchart of the procedure for ageing test for unibo powertools dataset

atures. The battery was charged at 1 C rate to 4.2 V (50 mA cut-off) before each discharge test. The values were measured in the discharge cycles with a sampling rate of 10 Hz. Different drive cycles such as UDDS, LA92, and US06, as well as mixes of them, were applied in the discharge tests. The discharge cycles with temperature of $0°C$, $10°C$ and $25°C$ were used for training and testing the proposed model.

3.1.2 Theory

Fig. 3.2 shows a common approach for time-series called many-to-many, where multiple input steps feed the network with one prediction made at each step. There are other approaches such as the many-to-one and one-to-many, where in the first case multiple time-steps are fed with one output produced, and in the second case one input is used to produce multiple time-steps. As the two battery datasets have very different sampling frequencies, two approaches are used: the many-to-many approach for the first model (low-frequency sampling) while in the second one (high-frequency sampling) are used the many-to-one approach.

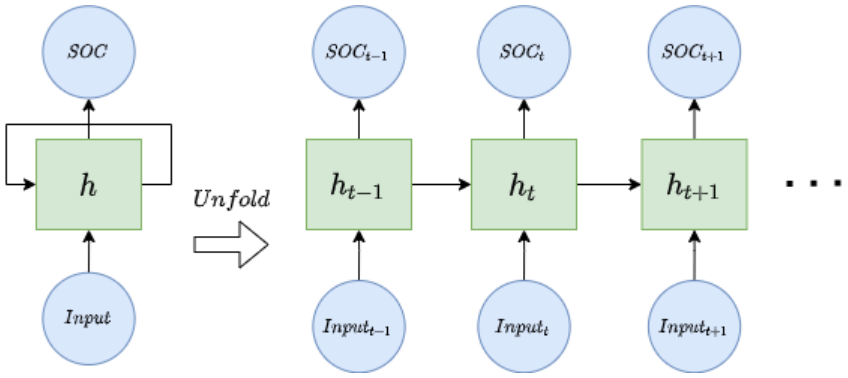

Figure 3.2: RNN architecture for SOC estimation unfolded in time

The long short-term memory is a type of RNN which is widely used to learn long-term dependencies without experiencing the exploding and vanishing gradient problems.

Two approaches that are based on lstm are presented below, one for each dataset, because of the huge difference in their sampling time. Scaled exponential linear units (SELU) [31] activation function is used in all the LSTM cells and hidden dense layers. In the output layer, the linear activation function is applied to produce the final *SOC* value.

The first approach is used for the UNIBO dataset. It is a deep neural network with three LSTM layers followed by two dense layers to map the learned states to desired *SOC* output. The number of cells of each LSTM layer is 256, 256, and 128 respectively. Fig. 3.3 illustrates the system architecture. The first layer is the input layer with battery parameters including voltage V_b, current i_B, and temperature T at each time step t. Since

it is a deep LSTM network, each LSTM layer returns a sequence which means that each step is propagated to the next layer. The many-to-many approach is used, and the *SOC* value is then estimated at each step.

The input time series feeding the deep LSTM network is defined as $[Input_{t_0}, Input_{t_1}, ..., Input_{t_n}]$, where n is the number of steps in the entire discharge cycle, and $Input = [V_{B_t}, i_{B_t}, T_t]$ represents voltage, current and temperature at each time step respectively. Although the entire discharge cycle feeds the network, only the part that precedes the step under examination is available as input for *SOC* estimation, i.e., the hidden state from previous steps $t-1$ and the current input at step t are used to estimate the output at step t.

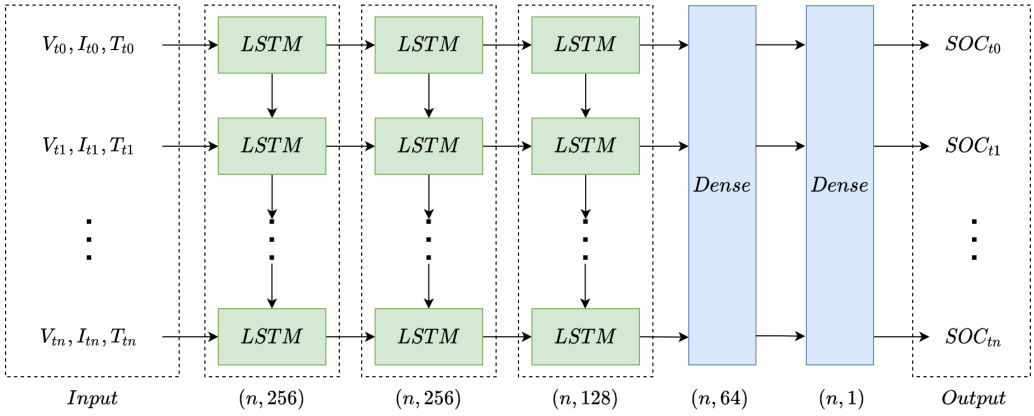

Figure 3.3: Architecture of the first model

The second model is used for the LG 18650HG2 Li-ion battery dataset. The model is composed of two LSTM layers followed by three dense layers. The number of cells of both LSTM layers is 256. Fig. 3.4 shows the architecture of the second proposed model. Since the second dataset contains more steps in one discharge cycle due to its higher sampling rate (100 ms), the many-to-one approach is more appropriate. In this case, for each n step as input, one output is returned. In the implementation, 300, 500, and 700 are used as the number of steps. For example, given input steps $[Input_{t_0}, Input_{t_1}, ..., Input_{t_{500}}]$, the model should estimate the *SOC* value at step 500.

The proposed models are implemented by using the Keras library [41]. The Adam algorithm [44] is chosen as the optimizer to update the network weights and biases with the learning rate configured as 0.00001. All proposed models are trained for 1000 epochs, but

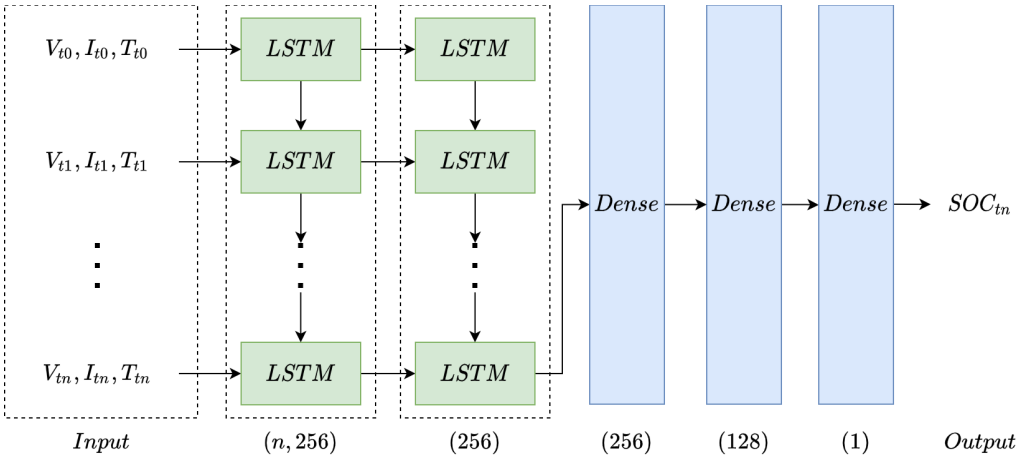

Figure 3.4: Architecture of the second model

the training process would stop earlier if there were no further improvement of validation loss within 50 epochs. The Huber loss [78] is used as the loss function. Its peculiarity is that it can be quadratic or linear depending on the error value.

3.1.3 Experimental Results

The proposed deep LSTM models are trained and tested using the two datasets. The model performance against each dataset is discussed in this section. Root Mean Square Error (RMSE) and mean absolute error (MAE) are used to evaluate the proposed models.

The Mean Square Error (MSE) is the sum of squared distances between the target and predicted variables divided by the number of samples. The RMSE is the square root of the MSE which scales the output value to the same scale as MAE. It is more sensitive to outliers as it penalizes the model by squaring the error. The MAE on the other hand is more robust to outliers as the error is not squared. MAE is an L1 loss function that calculates the sum of the absolute difference between the target and predicted variables. The MAE is more suitable for problems where the training data present outliers.

$$SOC_{mean} = \frac{1}{n}\sum |SOC - S\hat{O}C_{LSTM}| \tag{3.1}$$

$$SOC_{RMS} = \sqrt[2]{\frac{1}{n}\sum (SOC - S\hat{O}C_{LSTM})^2} \tag{3.2}$$

UNIBO Powertools dataset In tests performed on the "UNIBO Powertools" dataset, the performance of the method is evaluated on constant current discharge. It was trained on a total of 7738 discharge cycles. One cell per test type (standard, high current, preconditioned) and per cell capacity was extracted from the training data for use in testing. The overall MAE and RMSE on all test data are 0.69% and 1.34%, respectively.

The evaluation of the standard test type with rated capacity of 4.0Ah and the high current test type with rated capacity of 2.85Ah has the worst performance, due to the small amount of this test data in the dataset, specifically only two cell tests of the type, so only one cell was used for training and one for testing. Whereas, in the other types of tests with sufficient data the method can obtain accurate results with RMSE less than 1%.

In Fig. 3.5, Fig. 3.6, Fig. 3.7, the results obtained for this dataset are shown, tests were done at the beginning of life and at the end of life to verify the accuracy with different SOH.

The results were obtained always starting from fully charged cell, up to the cut-off. Where the *SOC* is charted against the discharge time in second. The black line is the *SOC* value obtained with the coulomb counting during the discharge and the red line is the *SOC* value estimated by LSTM.

The *SOC* in the first and last cycle is estimated accurately, which suggests that the estimation method can predict the *SOC* with different *SOH*. Moreover, very good performance is also obtained in the case of preconditioned cells, which shows that storage does not affect the estimation accuracy.

Table 3.3: UNIBO dataset tests performance

Test type	Nominal capacity	MAE	RMSE
Standard	4.0Ah	2.68%	3.42%
	3.0Ah	0.52%	0.73%
	2.85Ah	0.31%	0.39%
	2.0Ah	0.59%	0.80%
High Current	3.0Ah	0.46%	0.61%
	2.85Ah	2.13%	3.24%
Preconditioned	3.0Ah	0.47%	0.66%

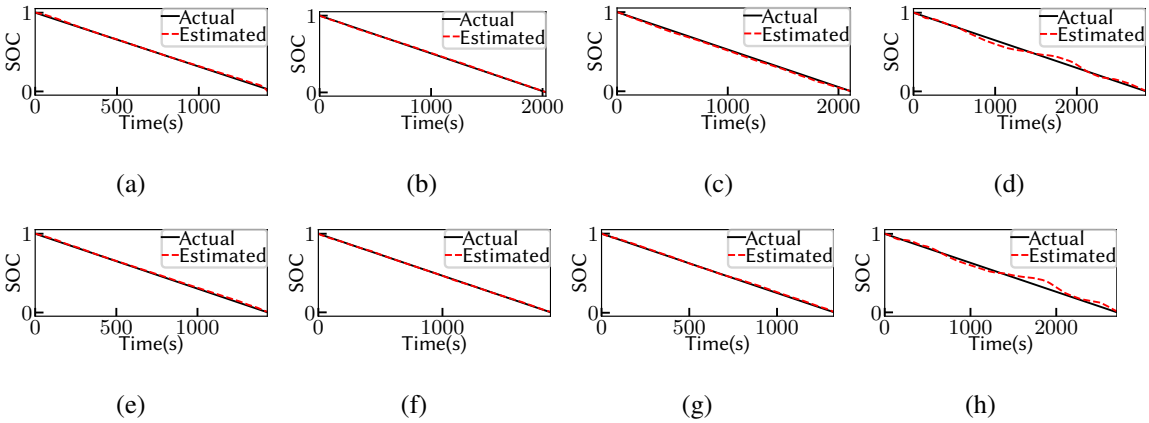

Figure 3.5: UNIBO dataset SOC estimation results (standard), (a, b, c, d) are all tested with *SOH* = 100%, (e, f, g, h) are all tested with *SOH* = 0%, (a,e) cell capacity = 2.0 Ah, (b,f) cell capacity = 2.85 Ah,(c, g) cell capacity = 3 Ah and (d, h) cell capacity = 4.0 Ah

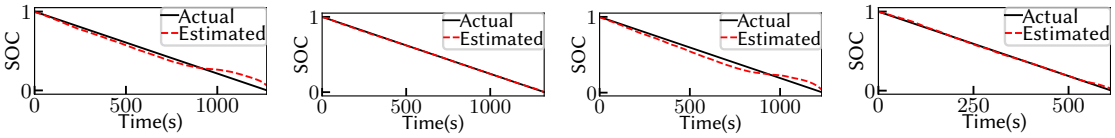

(a) (b) (c) (d)

Figure 3.6: UNIBO dataset SOC estimation results (high current), (a, b) are all tested with SOH = 100%, (c, d) are all tested with SOH = 0%, (a,c) cell capacity = 2.85 Ah, (b, d) cell capacity = 3 Ah

(a) (b)

Figure 3.7: UNIBO dataset SOC estimation results (preconditioned), (a) is tested with SOH = 100%, (b) is tested with SOH = 0%, both cell have the same capacity of 3.0 Ah

LG 18650HG2 dataset In the LG 18650HG2 Li-ion battery dataset, the performance of the method under dynamic discharge current is evaluated. Six mixed driving cycles for three different temperatures $0°C$, $10°C$ and $25°C$ were used as training set. Three different time series lengths were tested, with a number of steps of 300, 500, and 700, which are approximately equal to 30 seconds, 50 seconds, and 70 seconds depth in time respectively. The test set was composed of a UDDS, an LA92, and a US06 driving cycle plus one mixed driving cycle for each of the three different temperatures available in the dataset.

Table 3.4: LG 18650HG2 data tests performance

Temp. (°C)	300 Steps		500 Steps		700 Steps	
	MAE	RMSE	MAE	RMSE	MAE	RMSE
0	1.69%	2.27%	**1.47%**	**2.23%**	1.65%	2.60%
10	1.61%	2.12%	**1.57%**	**2.12%**	2.22%	2.89%
25	**1.17%**	**1.57%**	1.59%	2.02%	1.92%	2.64%

As shown in Tab. 3.4 the MAE and RMSE achieved by the 300 steps model are 1.47% and 1.99%. The 500 steps one reached a MAE and RMSE of 1.54% and 2.12%. The 700 steps model achieved 1.94% MAE and 2.72% RMSE. The model performance under each temperature with different input lengths is listed in Tab. 3.4. Among all the configurations, the best performance is achieved from testing data below $25°C$ temperature with 300 steps in input, which demonstrates that the battery operates most stably under room temperature. The model is able to learn the battery behavior at room temperature through the provided driving cycles without the need for a long history. Whereas, at $10°C$ and $0°C$ temperatures, better performance is obtained by the 500 input model. This indicates that increasing input steps could help to improve the estimation result at temperatures that are lower than room temperature. However, the worst results come from the 700 input steps which suggests that the increment of input steps must be selected carefully for the many-to-one approach as an inappropriate increment of input steps could result in performance degradation. The *SOC* estimation results on the mixed driving cycles at $0°C$, $10°C$ and $25°C$ temperatures are displayed in Fig. 3.8. The estimation results at the three temperatures are competitive and without significant errors. Still, errors can be seen from the ending steps in mixed

cycles at 0°C temperature due to their more dynamic discharge pattern.

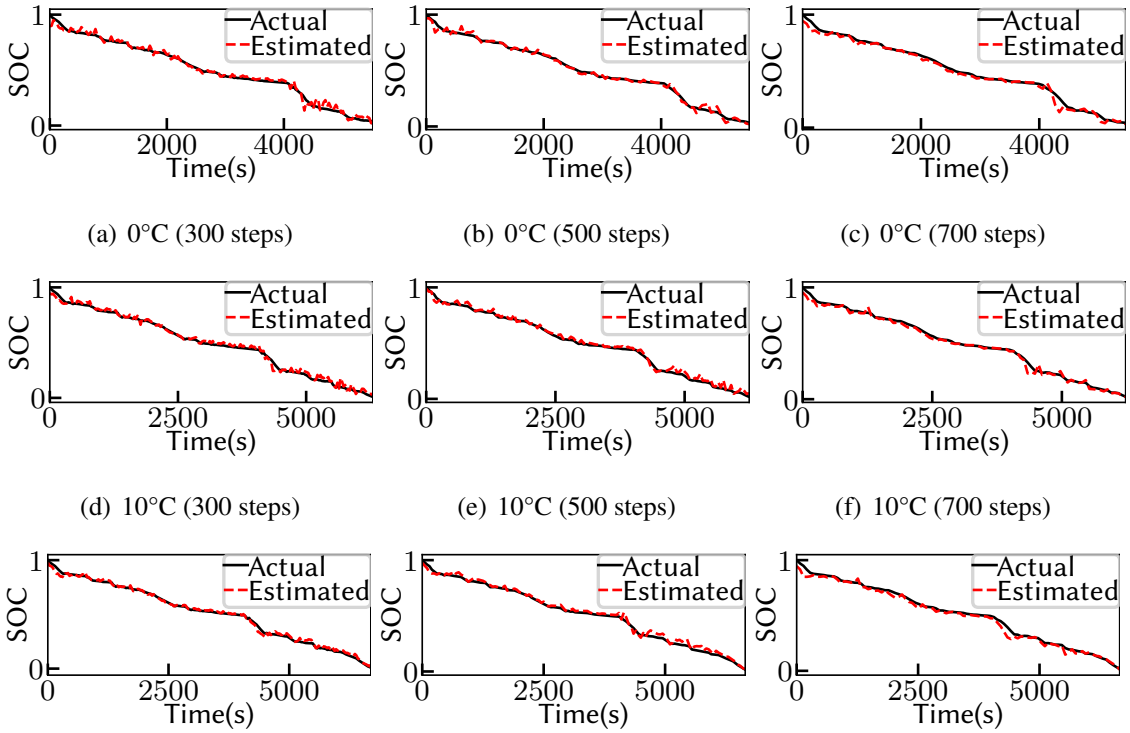

(a) 0°C (300 steps) (b) 0°C (500 steps) (c) 0°C (700 steps)

(d) 10°C (300 steps) (e) 10°C (500 steps) (f) 10°C (700 steps)

(g) 25°C (300 steps) (h) 25°C (500 steps) (i) 25°C (700 steps)

Figure 3.8: LG 18650HG data SOC estimation results (mixed cycles),

3.2 Extended Kalman Filter

The Kalman filter was originally introduced by R.E. Kalman (1930-2016) in 1960 in the article “A New Approach to Linear Filtering and Prediction Problems” [79]. This theory, extended for non-linear systems, was later applied to the batteries by Plett [71], for *SOC* estimation, and more recently it has been extended to the estimation of the cell parameters [72].

3.2.1 Theory

Kalman filters theory is based on the input-state-output system representations

A system is an object, device or phenomenon that interacts with the environment, this interaction is manifested through the variation of measurable quantities or variables, which can be quantified. The iterations between the system and the environment happen following the principle of causality.

The inputs are the independent variables, which describe the action of the surrounding environment on the system, while the outputs are dependent variables, which describe the response of the system to the inputs. The systems can be subdivided according to their characteristics, so it’s possible to identify algebraic systems or dynamic systems, linear or non-linear systems, stationary or non-stationary systems and finally continuous time or discrete time systems.

- **Algebraic systems**: the outputs of the system at a certain time instant depend only on the values of the inputs at the same time instant. **Dynamic systems**: in these systems the outputs also depend on the past values of the inputs. These models therefore have a memory (ability to accumulate energy) and are described by differential equations, harmonic response functions, etc.;

- **Linear systems**: systems where the principle of superposition of effects is applicable. The effect of a sum of inputs is equal to the sum of the effects produced by each individual input. **Non-linear systems**: the principle of superposition of effects is not valid;

- **Stationary systems**: the systems for which the property of translation in time of input and output is valid: that is if applying to the system the input u(t) the response is y(t) then, to parity of initial conditions, to the input translated in the time u(t-t0) the system responds with the output y(t-t0). **Non stationary systems**: the principle of translation in time does not apply, an input u(t) produces a response if it is applied to the system at the time u(t-t0);

- **Continuous time systems**: the system assumes a value at every instant of time, **Discrete time system**: the system assumes a value only for some instants of time called sampling instants.

In the representation of input-state-output type systems there are new variables that are neither input nor output, and they take the name of state variables. The state variable describes the internal behaviour of the system, and are tied up to its history, for this reason they can be considered as a memory of the system. It is possible to describe a system by means of two matrix equations, process equation

$$\frac{d\boldsymbol{x}(t)}{dt} = \mathbf{f}(\boldsymbol{x}(t), \mathbf{u}(t), t) \tag{3.3}$$

Measurement equation

$$\mathbf{y}(t) = \mathbf{h}(\boldsymbol{x}(t), \mathbf{u}(t), t) \tag{3.4}$$

$\mathbf{x}(t)$ is the state vector, $\mathbf{u}(t)$ is the input vector and $\mathbf{y}(t)$ is the output vector. While the function **f** e **h** are the state transition function and the output function respectively. Where $\boldsymbol{x}(t) \in \mathbb{R}^n$, $\boldsymbol{y}(t) \in \mathbb{R}^m$, $\boldsymbol{u}(t) \in \mathbb{R}^l$

The process equation is a differential equation of n-order , composed of n first-order differential equations, which relates the input variables to the state variables (n is the order of the model). The measurement equation is an algebraic equation that allows to determine the output at a certain instant of time from the knowledge of the state (and the input at the same instant of time.

For linear systems it is possible to rewrite the functions **f** e **g** as linear compositions of the matrices **F** e **B**, e **H** e **D** respectively. Where $\mathbf{F}(n \times n)$, $\mathbf{B}(n \times l)$, $\mathbf{A}(n \times n)$, $\mathbf{H}(m \times n)$,

$\mathbf{B}(m \times n)$, $\mathbf{A}(m \times l)$

$$\dot{\mathbf{x}}(t) = \mathbf{F}\mathbf{x}(t) + \mathbf{B}\mathbf{u}(t) \tag{3.5}$$

Measurement equation

$$\mathbf{y}(t) = \mathbf{H}\mathbf{x}(t) + \mathbf{D}\mathbf{u}(t) \tag{3.6}$$

For discrete time systems, the input-state-output representation can be used, however, the equations must be discretized. Through the discretization process, the differential equations become difference equations, and the time is expressible as k natural number multiplied by T_c representing the sampling time.

$$\boldsymbol{x}_{k+1} = \boldsymbol{f}(\boldsymbol{x}_k, \boldsymbol{u}_k, kT_c) \tag{3.7}$$

$$\boldsymbol{y}_{k+1} = \boldsymbol{h}(\boldsymbol{x}_k, \boldsymbol{u}_k, kT_c) \tag{3.8}$$

In the case that the discrete system is also linear it is possible to rewrite the equations as follows:

$$\mathbf{x}_{k+1} = \mathbf{F}\mathbf{x}_k + \mathbf{B}\mathbf{u}_k \tag{3.9}$$

$$\mathbf{y}_k = \mathbf{H}\mathbf{x}_k + \mathbf{D}\mathbf{u}_k \tag{3.10}$$

Kalman Filter

The Kalman Filter (KF) [77] recursively calculates an estimated state of a linear dynamic system as the weighted average between the predicted state and the measured state determined from the available measurements. The weighting is based on bases on the covariance, allowing to estimate a state with uncertainty lower than uncertainty of both the predicted and measured state. This iterative process minimizes the use of resources because requires measuring the current input and output quantities and storing only data related to the last estimated state. KF relies on the state-space formulation of linear dynamic systems in discrete time domain represented in Fig. 3.9. Assuming discrete time

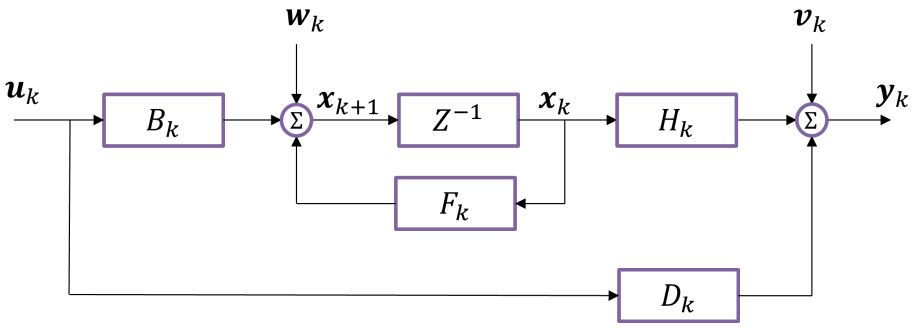

Figure 3.9: Schematic state-space representation of the linear dynamic system in discrete time at the basis of Kalman filter formulation [71]

sample k, the state vector $\boldsymbol{x}_k$ contains the minimal data set required to predict the future $k+1$ behavior of the system by using data taken from the past step k. Referring to state-space linear system representation, the transition matrix $\mathbf{F}_k$, brings the state from instant k to the future state $k+1$, matrix $\mathbf{B}_k$ represents the effect of a set of input variables $\boldsymbol{u}_k$ to the future state $\boldsymbol{x}_{k+1}$. Assuming the vector $\boldsymbol{y}_k$ as the set of output measurable quantities, the measurement matrix $\mathbf{H}_k$ determines the output from the states. The straightforward matrix $\mathbf{D}_k$ directly influences the output $\boldsymbol{y}_k$ with the input variables $\boldsymbol{u}_k$.

Two additional uncorrelated variables, the process noise $\boldsymbol{w}_k$ and the measurement error (or noise) v_k are added to the system. Both noises are Gaussian distributed white noise, have zero mean value and must be non-correlated to each other [77] . The covariance for $\boldsymbol{w}_k$ and $\boldsymbol{v}_k$ are respectively $\mathbf{Q}_k$ and $\mathbf{R}_k$:

$$\mathbb{E} = [w_n {w_k}^T] = \begin{cases} \mathbf{Q}_k & n = k \\ 0 & n \neq k \end{cases} \tag{3.11}$$

$$\mathbb{E} = [v_n {v_k}^T] = \begin{cases} \mathbf{R}_k & n = k \\ 0 & n \neq k \end{cases} \tag{3.12}$$

Assuming the following domains:

$$\boldsymbol{x}_k \in \mathbb{R}^n, \boldsymbol{y}_k \in \mathbb{R}^m, \boldsymbol{u}_k \in \mathbb{R}^l,$$
$$\mathbf{F}_k \in \mathbb{R}^{n \times n}, \mathbf{B}_k \in \mathbb{R}^{n \times l}, \mathbf{H}_k \in \mathbb{R}^{m \times n}, \mathbf{D}_k \in \mathbb{R}^{m \times l}$$

The two resulting fundamental equations are: the process equation (3.13) and the measurement equation (3.14)

$$\boldsymbol{x}_{k+1} = \mathbf{F}_k \boldsymbol{x}_k + \mathbf{B}_k \boldsymbol{u}_k + \boldsymbol{w}_k \tag{3.13}$$

$$\boldsymbol{y}_k = \mathbf{H}_k \boldsymbol{x}_k + \mathbf{D}_k \boldsymbol{u}_k + \boldsymbol{v}_k \tag{3.14}$$

Using the linear system representation of Fig. 3.9 and Eq. (3.13) and (3.14), the KF algorithm splits the estimation process, computed at the time interval k, in two consecutive steps: the prediction step and the update step.

In the prediction step, the Kalman filter:

1. estimates the current state $\hat{\boldsymbol{x}}_k^-$ with Eq. (3.15) using the estimated state at the previous step $\hat{\boldsymbol{x}}_{k-1}^-$ and the observed quantity at the previous step $\boldsymbol{u}_{k-1}$

$$\hat{\boldsymbol{x}}_k^- = \mathbf{F}_{k-1} \hat{\boldsymbol{x}}_{k-1}^- + \mathbf{B}_{k-1} \boldsymbol{u}_{k-1} \tag{3.15}$$

2. calculates the uncertainty of the state estimation $\hat{\boldsymbol{x}}_k^-$, in terms of predicted covariance $\mathbf{P}_k{}^-$ with Eq. (3.16), by processing the previous predicted covariance $\mathbf{P}_{k-1}$ and the process noise covariance $\mathbf{Q}_{k-1}$.

$$\mathbf{P}_k^- = \mathbf{F}_{k-1} \mathbf{P}_{k-1} \mathbf{F}_{k-1}^T + \mathbf{Q}_{k-1} \tag{3.16}$$

   Both estimations of the prediction step, , $\hat{\boldsymbol{x}}_k^-$ and $\mathbf{P}_k{}^-$, do not use any measurements taken at the current time;

3. calculates the Kalman gain matrix $\mathbf{G}_K$ using Eq. (3.17) from the previously estimated covariance $\mathbf{P}_k{}^-$ and the covariance matrix of the observed quantities $\mathbf{R}_k$. In this way estimated state $\hat{\boldsymbol{x}}_k$ will be updated by giving more weight to the estimates with higher accuracy.

$$\mathbf{G}_k = \mathbf{P}_k^- \mathbf{H}_k^T [\mathbf{H}_k \mathbf{P}_k^- \mathbf{H}_k^T + \mathbf{R}_k]^{-1} \tag{3.17}$$

In the update step, the Kalman filter:

1. calculates the estimated output quantity $\hat{\boldsymbol{y}}_k$ by applying the estimated states $\hat{\boldsymbol{y}}_k^-$ to the measured input quantities $\boldsymbol{u}_K$

$$\hat{\boldsymbol{y}}_k = \mathbf{H}_k \hat{\boldsymbol{x}}_k^- + \mathbf{D}_k \boldsymbol{u}_k \tag{3.18}$$

2. updates with Eq. (3.19) the estimated state at the new corrected values $\hat{\boldsymbol{x}}_k$, by applying the Kalman gain matrix $\mathbf{G}_K$ to the $(\boldsymbol{y}_k - \hat{\boldsymbol{y}}_k)$ difference. In Eq. (3.18) the measured output quantity $\boldsymbol{y}_k$ necessarily includes some amount of the measurement noise (or error) $\boldsymbol{v}_k$. Fig. Fig. 3.10 gives a schematic overview of the update function applied to a system state estimation.

$$\hat{\boldsymbol{x}}_k = \hat{\boldsymbol{x}}_k^- + \mathbf{G}_k[\boldsymbol{y}_k - \hat{\boldsymbol{y}}_k] \tag{3.19}$$

3. updates the covariance $\mathbf{P}_k$ of the corrected estimated state $\hat{\boldsymbol{x}}_k$

$$\mathbf{P}_k = (\mathbf{I} - \mathbf{G}_k \mathbf{H}_k)\mathbf{P}_k^- \tag{3.20}$$

Both updated state $\hat{\boldsymbol{x}}_k$ and updated covariance $\mathbf{P}_k$ will be used at the following time interval $k+1$ in the prediction step. Fig. 3.11 represents the described steps for states prediction and update. In this scheme it is also represented the initialization step at time $k = 0$ for setting both the state $\boldsymbol{x}_0$ and covariance matrix $\mathbf{P}_0$. Proper selection of these coefficients impacts on the estimation performances, mainly in terms of accuracy in the state estimation.

Summarizing, the KF can be used on linear systems only, where the model is perfectly known, noises are unrelated and the covariances of the noises can be calculated. Unfortunately, in many cases, as when dealing with Ion-Li cells, the model is both uncertain and non-linear, and the noise covariances are hard to calculate. Even under these conditions, the basic KF equations and the prediction-update process are used to derive more advanced estimators. These KF variants and, in particular, the so-called Extended Kalman Filter (EKF) [77], are now widely proposed as effective battery parameters estimators.

Extended Kalman Filter

If the system is non-linear, it is possible to extend the use of Kalman filtering through a linearization procedure. The resulting filter is referred to as the Extended Kalman Filter

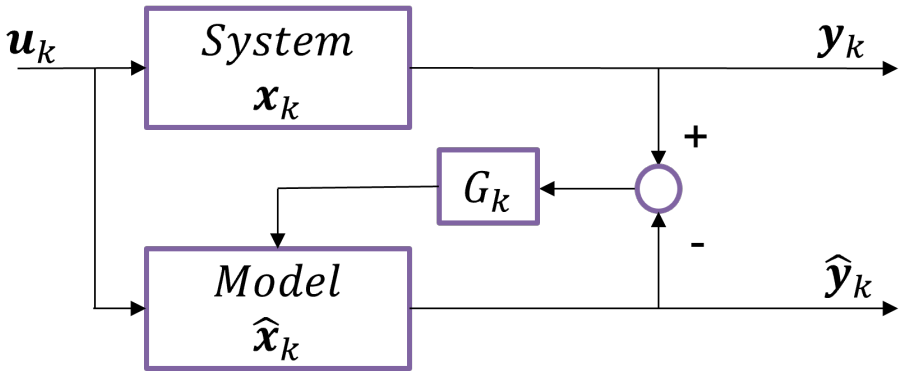

Figure 3.10: Schematic representation of the application of the Kalman gain to the measured and estimated outputs

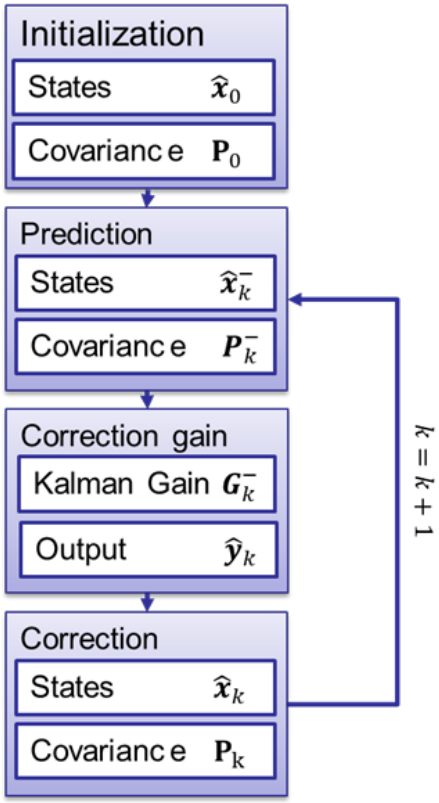

Figure 3.11: Sequence of the prediction and update steps in the Kalman filter estimation process[36]

(EKF) [71]. The non-linear system is still described by the state-space model representation, following the KF basic description. In EKF, $f(\boldsymbol{x}_k, \boldsymbol{u}_k)$ and $h(\boldsymbol{x}_k, \boldsymbol{u}_k)$ represent the non-linear transition matrix and the non-linear measurement matrix, respectively. The resulting fundamental KF Eq. (3.13) and (3.14) become the new process and measurement equations:

$$\boldsymbol{x}_{k+1} = \boldsymbol{f}(\boldsymbol{x}_k, \boldsymbol{u}_k) + \boldsymbol{w}_k \tag{3.21}$$

$$\boldsymbol{y}_{k+1} = \boldsymbol{h}(\boldsymbol{x}_k, \boldsymbol{u}_k) + \boldsymbol{v}_k \tag{3.22}$$

As in KF, $\boldsymbol{w}_k$ and $\boldsymbol{v}_k$ are independent zero-mean white Gaussian noise processes with covariance matrices $\mathbf{Q}_k$ and $\mathbf{R}_k$ respectively. Common assumption, introduced by many authors [36, 71] is that: if the system remains in the same external conditions, and the sensors used to make the measurements stay the same, the elements of the covariance matrices $\mathbf{Q}$, $\mathbf{R}$ can be kept constant. The basic idea of the Extended Kalman Filter is to linearize the system equations at each time instant around the most recent estimated state. If the functions f and h are changing slowly with time, they can be approximated with first order Taylor series. With this approximation, the Kalman Filter is then applied as in the linear case. The linearization process requires to calculate the partial derivatives of the two functions f and g with respect to each estimated states $\hat{\boldsymbol{x}}_k$ and $\hat{\boldsymbol{x}}_k^-$, for obtaining the new transition matrix $\mathbf{F}_k$ and the new measurement matrix $\mathbf{H}_k$:

$$\mathbf{F}_k = \left.\frac{\partial f(\boldsymbol{x}_k, \boldsymbol{u}_k)}{\partial \boldsymbol{x}}\right|_{\boldsymbol{x}=\hat{\boldsymbol{x}}_k} \tag{3.23}$$

$$\mathbf{H}_k = \left.\frac{\partial h(\boldsymbol{x}_k, \boldsymbol{u}_k)}{\partial \boldsymbol{x}}\right|_{\boldsymbol{x}=\hat{\boldsymbol{x}}_k^-} \tag{3.24}$$

The two non-linear functions (3.21) and (3.22) are then approximated using the two Taylor expansions:

$$\boldsymbol{f}(\boldsymbol{x}_k, \boldsymbol{u}_k) \approx \boldsymbol{f}(\hat{\boldsymbol{x}}_k, \boldsymbol{u}_k) + \mathbf{F}_k(\boldsymbol{x}_k - \hat{\boldsymbol{x}}_k) \tag{3.25}$$

$$\boldsymbol{h}(\boldsymbol{x}_k, \boldsymbol{u}_k) \approx \boldsymbol{h}(\hat{\boldsymbol{x}}_k^-, \boldsymbol{u}_k) + \mathbf{H}_k(\boldsymbol{x}_k - \hat{\boldsymbol{x}}_k) \tag{3.26}$$

So the new process equation and the new measurement equation are obtained:

$$\boldsymbol{x}_{k+1} = \mathbf{F}_k \boldsymbol{x}_k + \boldsymbol{f}(\hat{\boldsymbol{x}}_k, \boldsymbol{u}_k) - \mathbf{F}_k \hat{\boldsymbol{x}}_k + \boldsymbol{w}_k \tag{3.27}$$

$$\boldsymbol{y}_k = \mathbf{H}_k \boldsymbol{x}_k + \boldsymbol{h}(\hat{\boldsymbol{x}}_k, \boldsymbol{u}_k) - \mathbf{H}_k \hat{\boldsymbol{x}}_k + \boldsymbol{v}_k \tag{3.28}$$

Comparing (3.27) and (3.28) with (3.13) and (3.14), respectively, both terms witch are not function of $\boldsymbol{x}_k$ can be defined as follows:

$$[\boldsymbol{f}(\hat{\boldsymbol{x}}_k, \boldsymbol{u}_k) - \mathbf{F}_k \hat{\boldsymbol{x}}_k] = \mathbf{B}_k \boldsymbol{u}_k \tag{3.29}$$

$$[\boldsymbol{h}(\hat{\boldsymbol{x}}_k, \boldsymbol{u}_k) - \mathbf{H}_k \hat{\boldsymbol{x}}_k] = \mathbf{D}_k \boldsymbol{u}_k \tag{3.30}$$

Given the linearized state space model, represented by the two linearized equations:

$$\boldsymbol{x}_{k+1} = \mathbf{F}_k \boldsymbol{x}_k + \mathbf{B}_k \boldsymbol{u}_k + \boldsymbol{w} \tag{3.31}$$

$$\boldsymbol{y}_k = \mathbf{H}_k \boldsymbol{x}_k + \mathbf{D}_k \boldsymbol{u}_k + \boldsymbol{v} \tag{3.32}$$

The Kalman filter theory can be applied following the same sequence of the linear case represented in Fig. 3.11, briefly described as follows.

In the prediction step, the EKF:

1. estimates the current state $\hat{\boldsymbol{x}}_k^-$ with eq. (3.33), using the estimated state at the previous step $\hat{\boldsymbol{x}}_{k-1}^-$ and the observed quantity at the previous step $\boldsymbol{u}_{k-1}$

$$\hat{\boldsymbol{x}}_k^- = \boldsymbol{f}(\boldsymbol{x}_{k-1}, \boldsymbol{u}_{k-1}) \tag{3.33}$$

2. calculates the uncertainty of the state estimation $\hat{\boldsymbol{x}}_k^-$, in terms of predicted covariance $\mathbf{P}_k{}^-$ with eq. (3.34), by processing the previous predicted covariance $\mathbf{P}_{k-1}$. The process noise covariance $\mathbf{Q}$ and the estimate the transition matrix $\mathbf{F}_{k-1}$ (3.23), using the estimated state at the previous step $\hat{\boldsymbol{x}}_{k-1}^-$.

$$\mathbf{P}_k^- = \mathbf{F}_{k-1}\mathbf{P}_{k-1}\mathbf{F}_{k-1}^T + \mathbf{Q} \tag{3.34}$$

Both prediction step, $\hat{\boldsymbol{x}}_k^-$ and $\mathbf{P}_k{}^-$, do not use any measurements taken at the current time.

3. calculates the Kalman gain matrix $\mathbf{G}_K$ with (3.35) from the previously estimated covariance $\mathbf{P}_k^-$ and the covariance matrix of the observed quantities $\mathbf{R}$. In this way estimated state $\hat{\boldsymbol{x}}_k$ will be updated by giving more weight to the estimations with higher accuracy.

$$\mathbf{G}_k = \mathbf{P}_k^-\mathbf{H}_k^T[\mathbf{H}_k\mathbf{P}_k^-\mathbf{H}_k^T + \mathbf{R}_k]^{-1} \tag{3.35}$$

In the update step, the EKF:

1. estimates with (3.36) the output vector $\hat{\mathbf{y}}_k$ by applying the available estimated states $\hat{\boldsymbol{x}}_k^-$ to the measurement matrix $\mathbf{H}_k$ calculated with Eq. (3.24), and the actual inputs $\boldsymbol{u}_k$:

$$\hat{\boldsymbol{y}}_k = \boldsymbol{h}(\boldsymbol{x}_k, \boldsymbol{u}_k) \tag{3.36}$$

2. updates with (3.37) the estimated state at the new corrected values $\hat{\boldsymbol{x}}_k$, by applying the Kalman gain matrix $\mathbf{G}_K$ to the $(\boldsymbol{y}_k - \hat{\boldsymbol{y}}_k)$ difference.

$$\hat{\boldsymbol{x}}_k = \hat{\boldsymbol{x}}_k^- + \mathbf{G}_k[\boldsymbol{y}_k - \hat{\boldsymbol{y}}_k] \tag{3.37}$$

3. updates the covariance $\mathbf{P}_k$ of the corrected estimated state $\hat{\boldsymbol{x}}_k$

$$\mathbf{P}_k = (\mathbf{I} - \mathbf{G}_k\mathbf{H}_k)\mathbf{P}_k^- \tag{3.38}$$

Both updated state $\hat{\boldsymbol{x}}_k$ and updated covariance $\mathbf{P}_k$ will be used at the following time interval $k+1$ in the prediction step, as represented in the flowchart of Fig. 3.11.

3.2.2 Battery applications

In this section two implementations of the EKF will be proposed, with the aim of determining the *SOC*, and the parameter R_0, in both cases the single polarization model shown in section 1.4.4 will be used as a reference model whose scheme and equations.

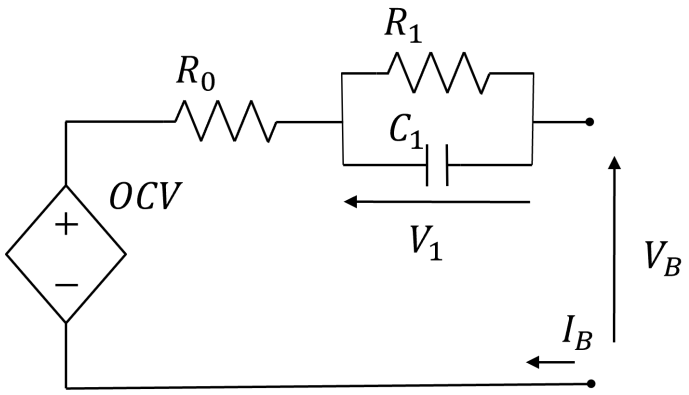

Figure 3.12: Single polarization model

$$\begin{aligned} V_{B_k} &= OCV(SOC_k) - R_0(SOC_k) \times i_{B_k} - V_{1_k} \\ V_{1_{k+1}} &= V_{1_k} \times (e^{-\frac{\Delta t}{\tau_1(SOC_k)}}) + R_1(SOC_K) \times i_{B_k} \times (1 - e^{-\frac{\Delta t}{\tau_1(SOC_k)}}) \\ SOC_{k+1} &= SOC_k - \frac{i_{B_k} \times \Delta t}{C_{nom}} \end{aligned} \tag{3.39}$$

SOC estimation

For the determination of the state of charge by means of Kalman Filter is followed the procedure described by [69]. The voltage at the ends of the capacitor V_1, and the *SOC* are chosen as state variables, these variables in fact represent a memory of the system and for this reason they can be used in the input state output representation. The input variable is the current, while the temperature is not taken into account, and is considered as a disturbance of the system. The measurable output is the voltage at the ends of the battery.

By summarizing, the state variable vector $\boldsymbol{x}$ is defined as:

$$\boldsymbol{x} = \begin{bmatrix} V_1 \\ SOC \end{bmatrix} \tag{3.40}$$

The input variable vector $\mathbf{u}$ is defined by the cell current i_B only:

$$\boldsymbol{u} = u = [i_B] \tag{3.41}$$

and the output variable vector $\boldsymbol{y}$ is defined by the cell voltage v_B only:

$$\boldsymbol{y} = y = [v_B] \tag{3.42}$$

The EKF estimator is implemented by using the notation and procedure introduced in Section 3.2.1 and the discretization time interval Δt.

$$f(\boldsymbol{x}_k, \mathbf{u}_k) = \begin{bmatrix} V_{1_k} \times (e^{-\frac{\Delta t}{\tau_1}}) + R_1 \times i_{B_k} \times (1 - e^{-\frac{\Delta t}{\tau_1}}) \\ SOC_k - \frac{i_{B_k} \times \Delta t}{C_{nom}} \end{bmatrix} \tag{3.43}$$

$$h(\boldsymbol{x}_k, \mathbf{u}_k) = [OCV_k - V_{c_k} - R_0 i_{B_k}] \tag{3.44}$$

The open circuit voltage OCV of the battery is considered a function of the SOC only. To implement the EKF, it is necessary to make explicit the function $OCV - SOC$, for calculating its derivative at the considered point. The equation used is the one presented in the modeling chapter, eq: (2.36), given below.

$$\begin{aligned} OCV(SOC) =& a + bSOC + cSOC^2 + \frac{d}{SOC} + \\ &+ e\ln(SOC) + f\ln(1 - SOC) \end{aligned} \tag{3.45}$$

The model parameters, R_0, R_1, τ_1 are recalculated at each iteration through their function seen above, so the value is updated with the current SOC.

$$\mathbf{F}_k = \frac{\partial \boldsymbol{f}(\boldsymbol{x}_k, \boldsymbol{u}_k)}{\partial \boldsymbol{x}} = \begin{bmatrix} \frac{\partial V_1(\boldsymbol{x}_k, \boldsymbol{u}_k)}{\partial V_c} & \frac{\partial V_1(\boldsymbol{x}_k, \boldsymbol{u}_k)}{\partial SOC} \\ \frac{\partial SOC(\boldsymbol{x}_k, \boldsymbol{u}_k)}{\partial V_c} & \frac{\partial SOC(\boldsymbol{x}_k, \boldsymbol{u}_k)}{\partial SOC} \end{bmatrix} = \begin{bmatrix} e^{-\frac{\Delta t}{\tau_1}} & 0 \\ 0 & 1 \end{bmatrix} \tag{3.46}$$

$$\mathbf{H}_k = \frac{\partial \boldsymbol{h}(\boldsymbol{x}_k, \boldsymbol{u}_k)}{\partial \boldsymbol{x}} = \begin{bmatrix} \frac{\partial V_B(\boldsymbol{x}_k, \boldsymbol{u}_k)}{\partial V_1} & \frac{\partial V_B(\boldsymbol{x}_k, \boldsymbol{u}_k)}{\partial SOC} \end{bmatrix} = \begin{bmatrix} -1 & \frac{\partial OCV(SOC)}{\partial SOC} \end{bmatrix} \tag{3.47}$$

R0 estimation

The estimation of the internal parameters, is fundamental in order to determine the *SOH* of the battery, the model used is always the SP model shown in Fig. 3.12, and is used as a reference for the implementation at [19].

The voltage of the RC branch V_1, the DC resistance R_0, the resistance of the RC branch R_1, the time constant of the RC branch $\tau_1 = R_1 C_1$, the parameters R_0, R_1, τ_1 can be chosen as state variables, since they have a variation in time that can be traced back due to the *SOC* and *SOH* dynamic, in both charge and discharge direction, and these parameters change over the life of the battery.

Summarizing, the state variable vector $\boldsymbol{x}$ is defined as:

$$\boldsymbol{x} = \begin{bmatrix} V_1 \\ R_0 \\ R1 \\ \tau_1 \end{bmatrix} \tag{3.48}$$

The input variable vector $\mathbf{u}$ is defined by the cell current i_B only

$$\boldsymbol{u} = u = [i_B] \tag{3.49}$$

and output variable vector $\boldsymbol{y}$ is defined by the cell voltage v_B only

$$\boldsymbol{y} = y = [v_B] \tag{3.50}$$

The EKF estimator is implemented by using the notation and procedure introduced in Section 3.2.1 and the discretization time interval Δt. From the SP circuit of Fig. 3.12, the discretized state variable $\boldsymbol{x} = f(\boldsymbol{x}_k, \boldsymbol{u}_k)$ is expressed by (3.51).

$$f(\boldsymbol{x}_k, \boldsymbol{u}_k) = \begin{bmatrix} V_{1_k}(1 - \frac{\Delta t}{\tau_{1_k}}) + \frac{\Delta t}{\tau_{1_k}} R_{1_k} i_{B_k} \\ R_{0_k} \\ R_{1_{k-1}} \\ \tau_{1_k} \end{bmatrix} \tag{3.51}$$

The discretized output variable $\boldsymbol{y}_k = h(\boldsymbol{x}_k, \boldsymbol{u}_k)$ is derived by the SP circuit as:

$$h(\boldsymbol{x}_k, \boldsymbol{u}_k) = [OCV_k - V_{c_k} - R_{0_k} i_{B_k}] \tag{3.52}$$

Where V_{OC_k} is the Open Circuit Voltage. The open circuit voltage OCV of the battery is considered a function of the SOC only. In order to implement the EKF, it is necessary to make explicit the function $OCV - SOC$, in order to calculate its derivative at the considered point. The equation used is the one presented in the modeling chapter, eq: (2.36), given below.

$$\begin{aligned} OCV(SOC) =& a + bSOC + cSOC^2 + \frac{d}{SOC} + \\ &+ e\ln(SOC) + f\ln(1 - SOC) \end{aligned} \tag{3.53}$$

With the aim of reducing the complexity of the system and therefore the complexity of the linearization process the eq: (3.39), has been approximated using the first order Taylor approximation.

$$\begin{aligned} \mathbf{F}_k &= \frac{\partial \boldsymbol{f}(\boldsymbol{x}_k, \boldsymbol{u}_k)}{\partial \boldsymbol{x}} = \\ &= \begin{bmatrix} \frac{\partial V_1(\boldsymbol{x}_k, \boldsymbol{u}_k)}{\partial V_1} & \frac{\partial V_1(\boldsymbol{x}_k, \boldsymbol{u}_k)}{\partial R_0} & \frac{\partial V_1(\boldsymbol{x}_k, \boldsymbol{u}_k)}{\partial R_1} & \frac{\partial V_1(\boldsymbol{x}_k, \boldsymbol{u}_k)}{\partial \tau_1} \\ \frac{\partial R_0(\boldsymbol{x}_k, \boldsymbol{u}_k)}{\partial V_1} & \frac{\partial R_0(\boldsymbol{x}_k, \boldsymbol{u}_k)}{\partial R_0} & \frac{\partial R_0(\boldsymbol{x}_k, \boldsymbol{u}_k)}{\partial R_1} & \frac{\partial R_0(\boldsymbol{x}_k, \boldsymbol{u}_k)}{\partial \tau_1} \\ \frac{\partial R_1(\boldsymbol{x}_k, \boldsymbol{u}_k)}{\partial V_1} & \frac{\partial R_1(\boldsymbol{x}_k, \boldsymbol{u}_k)}{\partial R_0} & \frac{\partial R_1(\boldsymbol{x}_k, \boldsymbol{u}_k)}{\partial R_1} & \frac{\partial R_1(\boldsymbol{x}_k, \boldsymbol{u}_k)}{\partial \tau_1} \\ \frac{\partial \tau_1(\boldsymbol{x}_k, \boldsymbol{u}_k)}{\partial V_1} & \frac{\partial \tau_1(\boldsymbol{x}_k, \boldsymbol{u}_k)}{\partial R_0} & \frac{\partial \tau_1(\boldsymbol{x}_k, \boldsymbol{u}_k)}{\partial \tau_1} & \frac{\partial R_1(\boldsymbol{x}_k, \boldsymbol{u}_k)}{\partial \tau_1} \end{bmatrix} = \\ &= \begin{bmatrix} (1 - \frac{\Delta t}{\tau_{1_{k-1}}}) & 0 & \frac{\Delta t}{\tau_{1_{k-1}}} \times i_{B_{k-1}} & V_{1_{k-1}} \frac{\Delta t}{\tau^2_{1_{k-1}}} - \frac{\Delta t}{\tau^2_{1_{k-1}}} R_{1_{k-1}} i_{B_{k-1}} \\ 0 & 1 & 0 & 0 \\ 0 & 0 & 1 & 0 \\ 0 & 0 & 0 & 1 \end{bmatrix} \end{aligned} \tag{3.54}$$

$$\begin{aligned} \mathbf{H}_k &= \frac{\partial \boldsymbol{h}(\boldsymbol{x}_k, \boldsymbol{u}_k)}{\partial \boldsymbol{x}} = \\ &= \begin{bmatrix} \frac{\partial V_B(\boldsymbol{x}_k, \boldsymbol{u}_k)}{\partial V_1} & \frac{\partial V_B(\boldsymbol{x}_k, \boldsymbol{u}_k)}{\partial R_0} & \frac{\partial V_B(\boldsymbol{x}_k, \boldsymbol{u}_k)}{\partial R_1} & \frac{\partial V_B(\boldsymbol{x}_k, \boldsymbol{u}_k)}{\partial \tau_1} \end{bmatrix} = \\ &= \begin{bmatrix} -1 & -i_{B_k} & 0 & 0 \end{bmatrix} \end{aligned} \tag{3.55}$$

3.2.3 Experimental Results

To test the Extended Kalman Filter, a power profile was used. The used profile is obtained from a standardized driving cycle for passenger cars (WLTC). As the driving cycle is defined as a speed profile, the reference power was calculated by introducing the vehicle model [42]. In other words, the cycle represents the hypothetical operation of the cell in an automotive application. The reference power profile has been applied to the real cell and the voltage and current were measured throughout the test. The tests begins with fully charged cells, and stops when the discharge cut-off voltage is reached. Three power profiles were used, so that the performance of the filter could be evaluated under different conditions.

Once the actual cell usage profiles were obtained, they were imported into Matlab environment, where the EKF algorithms were implemented. The input and output vectors used in the filter are real data, so that also the non-ideality of the measuring instruments, as well as the variation of cell temperature, are considered.

Tests were conducted on cells from different manufacturers. Two cells are considered high energy and one high power. The cells used are LG M50T, Samsung S50E and Molicel P42A, their specifications have been summarized in the table 3.5. In addition, the cells have different SOHvalues, to verify that the estimate of SOC, and especially of R_0 is accurate for different aging values.

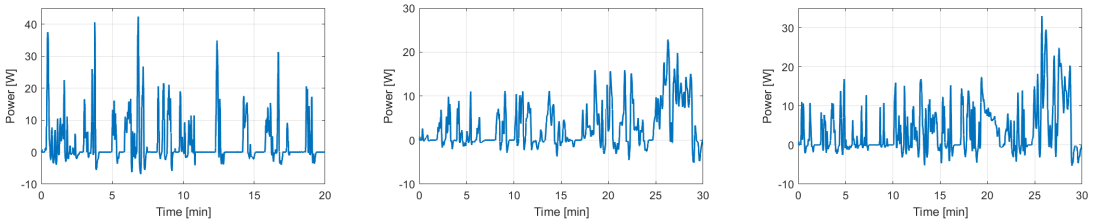

(a) Cycle A (b) Cycle B (c) Cycle C

Figure 3.13: Three used profile, (a) Cycle A: Energy = 0.951 [Wh], Max power = 42.351 [W], Mean Power = 2.853 [W]; (b) Cycle B: Energy = 0.593 [Wh], Max power = 15.847 [W], Mean Power = 1.780 [W]; (c) Cycle C: Energy = 0.869 [Wh], Max power = 17.327 [W], Mean Power = 2.607 [W]

Figure 3.14: Cells examined from left to right: LG M50T, Samsung 50E, Molicel P42A

Table 3.5: Nominal data of the cells selected for the experimental tests

Manufacturer	LG	SAMSUNG	MOLICEL
Model	INR21700 50T	INR21700 50E	INR21700 P42A
Chemistry	NMC	NMC	NMC
Capacity [Ah]	5	4.9	4.2
Energy [Wh]	18.15	17.6	15.1
Weight [g]	70	70	70

SOC

The voltage error is calculated between the real voltage and the filter estimated one, the value is normalized by the nominal voltage of each cell, as in (3.57) and (3.56), (3.59) and (3.58).

The state of charge is not directly measurable. The capacity measured by the wattmeter was used to determine the *SOC* value, and normalized for the value at the end of discharge. Since all tests end when the voltage cut-off is reached, the cell is considered to have reached $SOC = 0$.

The MAE and RMS values were calculated for each test, all results are reported in Tab. 3.6, Tab. 3.7, Tab. 3.8. The trend of the two values of the *SOC*with the relative error were reported below.

$$V_{Mean} = \frac{\frac{1}{n}\sum |v_{B_{real}} - \hat{v}_{B_{EKF}}|}{v_{nom}}. \tag{3.56}$$

$$V_{RMS} = \frac{\sqrt[2]{\frac{1}{n}\sum(v_{B_{real}} - \hat{v}_{B_{EKF}})^2}}{v_{nom}} \tag{3.57}$$

$$SOC_{Mean} = \frac{1}{n}\sum |SOC_{model} - \hat{SOC}_{EKF}|. \tag{3.58}$$

$$SOC_{RMS} = \sqrt[2]{\frac{1}{n}\sum(SOC_{model} - \hat{SOC}_{EKF})^2} \tag{3.59}$$

Table 3.6: LG - M50T EKF-*SOC*estimation performance

Test type	SOH	Voltage		SOC	
		MAE	RMSE	MAE	RMSE
A	100 %	44.40 ppm	0.03 ppm	2.11 %	0.62 %
	50 %	42.35 ppm	-0.27 ppm	1.70 %	-0.87 %
	0 %	43.13 ppm	-0.38 ppm	1.44 %	-0.42 %
B	100 %	40.55 ppm	-0.02 ppm	1.94 %	0.36 %
C	100 %	38.85 ppm	-0.20 ppm	1.91 %	-0.30 %

Table 3.7: Samsung - S50E EKF-SOC estimation performance

Test type	SOH	Voltage		SOC	
		MAE	RMSE	MAE	RMSE
A	100 %	16.49 ppm	-0.62 ppm	0.63 %	-0.28 %
	50 %	20.03 ppm	-0.84 ppm	2.62 %	2.28 %
	0 %	15.06 ppm	0.05 ppm	4.95 %	4.37 %
B	0 %	15.52 ppm	0.04 ppm	3.92 %	3.33 %
C	0 %	22.27 ppm	-0.99 ppm	4.07 %	3.52 %

Table 3.8: Molicel - P42A EKF-SOC estimation performance

Test type	SOH	Voltage		SOC	
		MAE	RMSE	MAE	RMSE
A	100 %	7.52 ppm	0.13 ppm	2.17 %	-1.50 %
B	100 %	22.52 ppm	-0.13 ppm	2.52 %	-1.92 %
C	100 %	102.16 ppm	0.40 ppm	1.72 %	-0.89 %

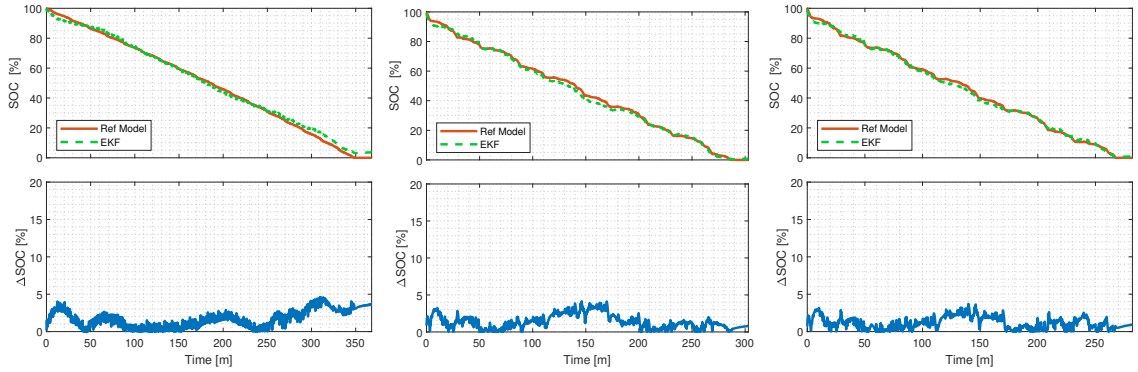

(a) SOH 100% Cycle A (b) SOH 50% Cycle A (c) SOH 0% Cycle A

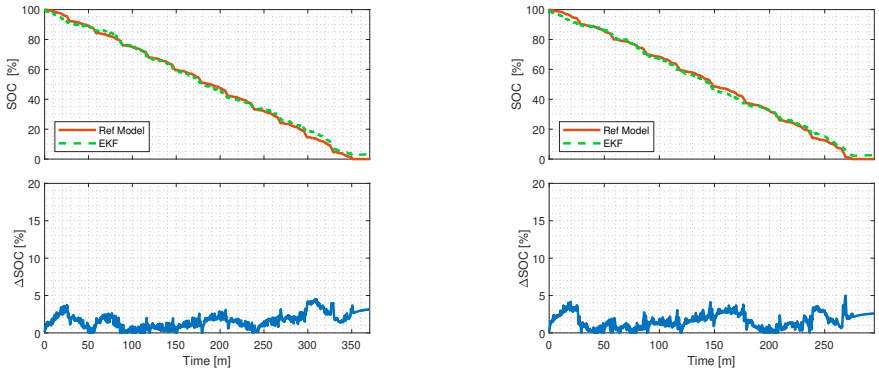

(d) SOH 100% Cycle B (e) SOH 100% Cycle C

Figure 3.15: Tests results, LG - M50T EKF-SOC estimation performance

R0

The voltage error is calculated between the real voltage and the filter estimated one, the value is normalized by the nominal voltage of each cell, as in (3.61) and (3.60), (3.63) and (3.62).

To compare the estimated value of the internal resistance R_0, the cell model described in the previous chapter was used. The model is used as a reference to estimate the value of R_0 is considered reliable, and has already been validated previously. The current measured in the laboratory test was used as input in order to obtain the resistance trend in time as a function of SOC, for that specific SOH value. The interaction between the various systems is shown in Fig. 3.18.

The MAE and RMS values were calculated for each test, all results are reported in Tab. 3.6, Tab. 3.7, Tab. 3.8. The trends of the two values of the R_0 with the relative error were

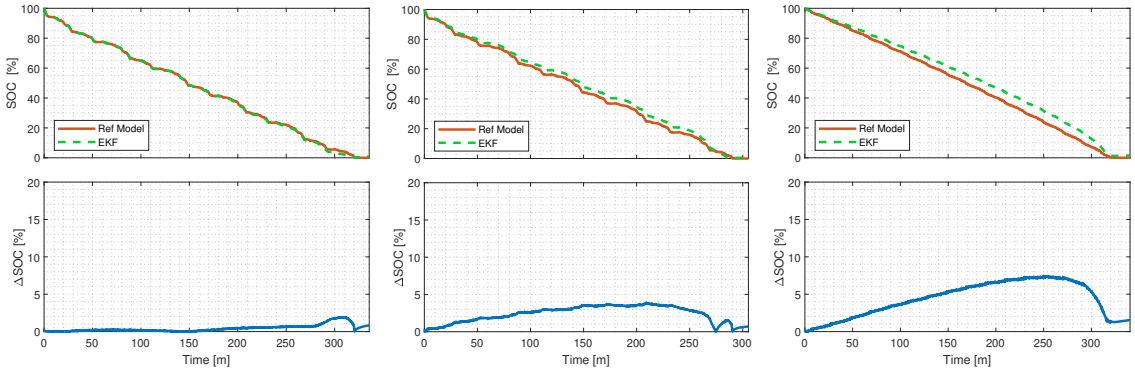

(a) SOH 100% Cycle A (b) SOH 50% Cycle A (c) SOH 0% Cycle A

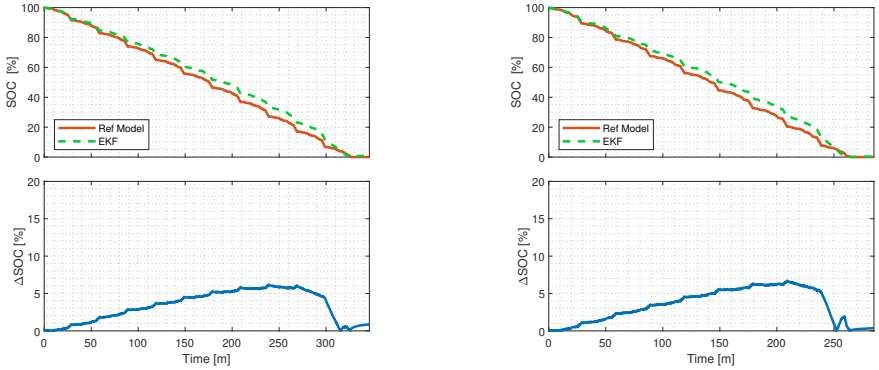

(d) SOH 0% Cycle B (e) SOH 0% Cycle C

Figure 3.16: Tests results, Samsung - S50E EKF-SOC estimation performance

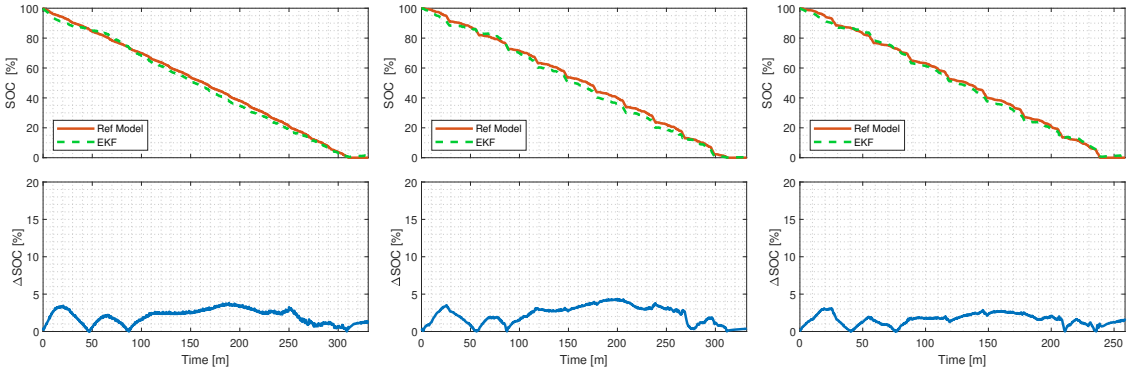

(a) SOH 100% Cycle A (b) SOH 100% Cycle B (c) SOH 100% Cycle C

Figure 3.17: Tests results, Molicel - P42A EKF-SOC estimation performance

reported below.

$$V_{Mean} = \frac{\frac{1}{n}\sum |v_{B_{real}} - \hat{v}_{B_{EKF}}|}{v_{nom}}. \tag{3.60}$$

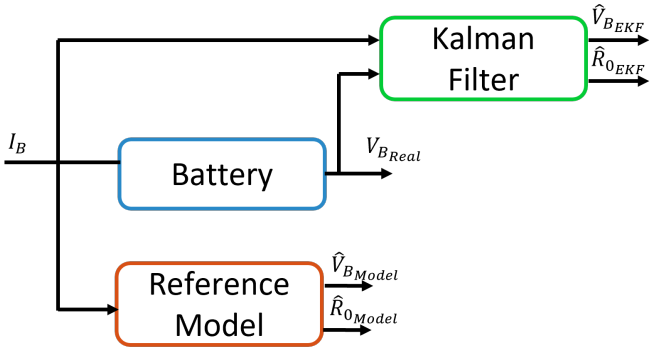

Figure 3.18: Block diagram of the EKF validation procedure

$$V_{RMS} = \frac{\sqrt[2]{\frac{1}{n}\sum(v_{B_{real}} - \hat{v}_{B_{EKF}})^2}}{v_{nom}} \tag{3.61}$$

$$R_{Mean} = \frac{\frac{1}{n}\sum|R_{0_{model}} - \hat{R}_{0_{EKF}}|}{R_{0_{model}}|_{SOC=50\%}} \tag{3.62}$$

$$R_{RMS} = \frac{\sqrt[2]{\frac{1}{n}\sum(R_{0_{model}} - \hat{R}_{0_{EKF}})^2}}{R_{0_{model}}|_{SOC=50\%}} \tag{3.63}$$

Table 3.9: LG - M50T EKF-R_0 estimation performance

Test type	SOH	Voltage		Resistance	
		MAE	RMSE	MAE	RMSE
A	100 %	3.52 ppm	80.41 ppm	1.80 %	4.80 %
	50 %	-3.86 ppm	65.15 ppm	1.62 %	2.83 %
	0 %	-4.33 ppm	61.49 ppm	-0.91 %	3.60 %
B	100 %	1.94 ppm	65.17 ppm	1.84 %	5.61 %
C	100 %	0.77 ppm	78.53 ppm	3.17 %	21.28 %

Table 3.10: Samsung - S50E EKF-R_0 estimation performance

Test type	SOH	Voltage		Resistance	
		MAE	RMSE	MAE	RMSE
A	100 %	-3.30 ppm	57.72 ppm	2.18 %	4.14 %
	50 %	-5.23 ppm	62.89 ppm	1.16 %	3.31 %
	0 %	-2.61 ppm	60.29 ppm	1.95 %	5.41 %
B	0 %	-1.79 ppm	58.83 ppm	4.20 %	5.32 %
C	0 %	-2.84 ppm	56.94 ppm	2.63 %	3.50 %

Table 3.11: Molicel - P42A EKF-R_0 estimation performance

Test type	SOH	Voltage		Resistance	
		MAE	RMSE	MAE	RMSE
A	100 %	1.14 ppm	12.90 ppm	1.62 %	16.07 %
B	100 %	0.49 ppm	13.34 ppm	0.70 %	11.15 %
C	100 %	0.93 ppm	12.76 ppm	7.52 %	14.53 %

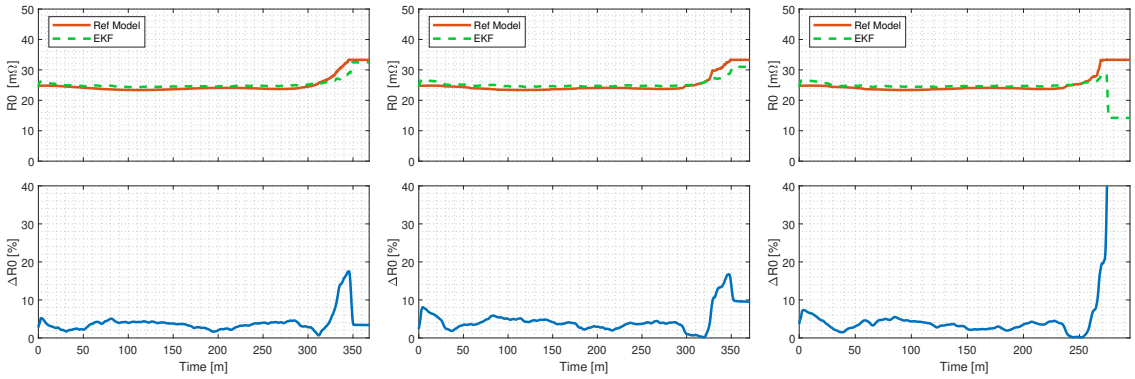

(a) SOH 100% Cycle A (b) SOH 50% Cycle A (c) SOH 0% Cycle A

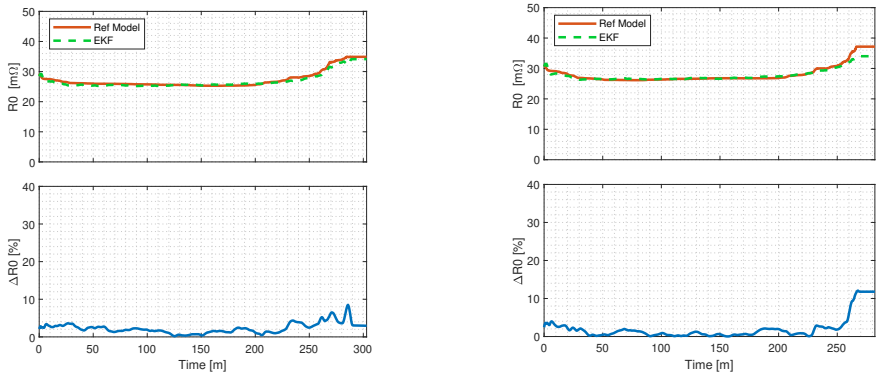

(d) SOH 100% Cycle B (e) SOH 100% Cycle C

Figure 3.19: tests results, LG - M50T EKF-R_0 estimation performance

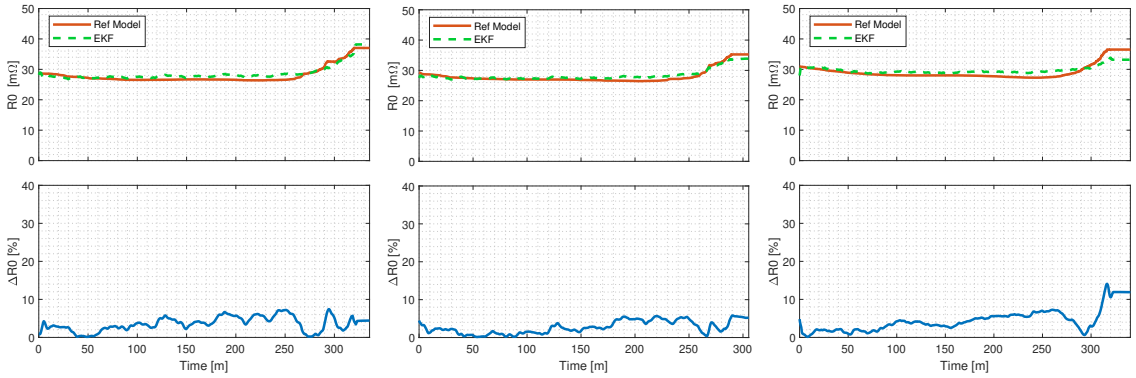

(a) SOH 100% Cycle A (b) SOH 50% Cycle A (c) SOH 0% Cycle A

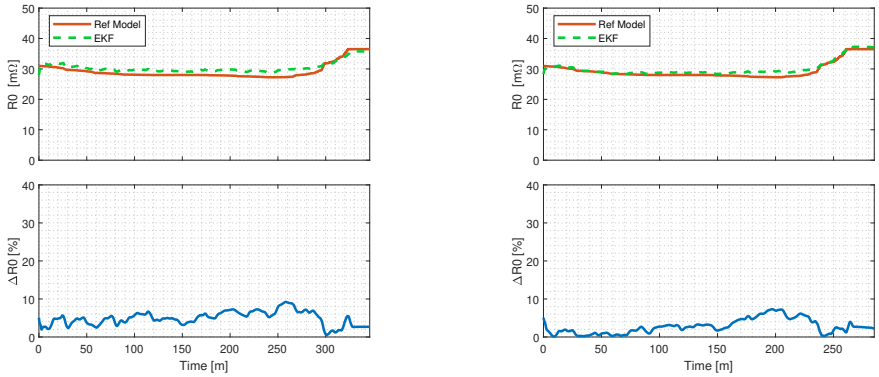

(d) SOH 0% Cycle B (e) SOH 0% Cycle C

Figure 3.20: Tests results, Samsung - S50E EKF-R_0 estimation performance

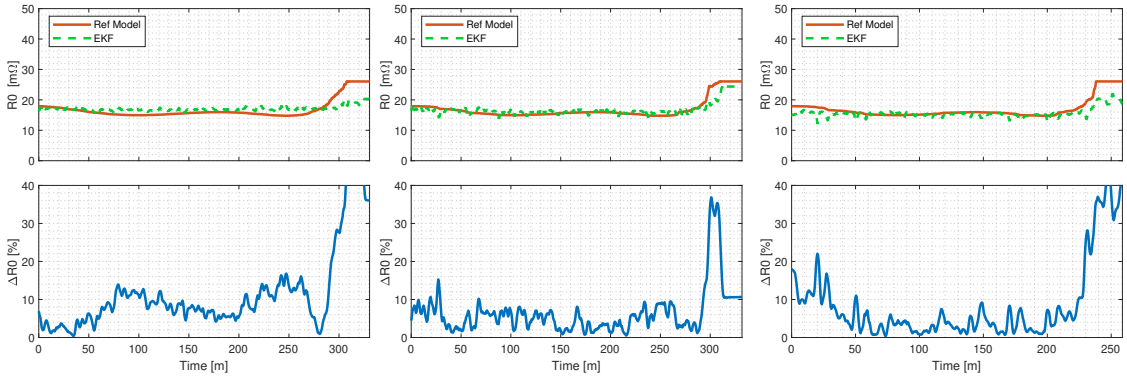

(a) SOH 100% Cycle A (b) SOH 100% Cycle B (c) SOH 100% Cycle C

Figure 3.21: Tests results, Molicel - P42A EKF-R_0 estimation performance

The results obtained using of the Extended Kalman Filter show excellent results both for the estimation of the *SOC* and for the estimation of the internal resistance R_0. The error reached on the estimate of the *SOC*, is consistent with what is present in the literature, with average errors around 2% with the only exception of the tests conducted on the Samsung S550E cell, where the error is around 4%, for the aged cell, which however remains an acceptable value.

This method can achieve a good accuracy on the internal resistance R_0 estimation. The maximum error is high due to the initial value of R_0, but the filter quickly converges to the true value. With such a low error value, it is interesting to estimate the internal resistance in order to evaluate the *SOH* of the cell, which would not be possible with higher errors. In this case the value of the internal resistance R_0 increases by 20% after 200 cycles for the LG sample and 40% after 500 cycles for the Samsung sample. The biggest errors on the estimate of the internal resistance are seen in the final part of the discharge, where the value of R_0 increases a lot compared to the value in the central area of the discharge, so the estimate in this area is not considered reliable.

The very high error values for the estimate of the internal resistance in the P42A sample are due to the low value of internal resistance of the cell, for this reason an error on the estimate of some $m\Omega$ leads to a much higher percentage error for this cell, but nevertheless remains acceptable for the methodology used.

3.3 Dual Extended Kalman Filter

3.3.1 Theory

An evolution of the EKF is represented by the Dual Extended Kalman Filter (DEKF). The estimation of the *SOC* with a Kalman filter depends strongly on the accuracy of the electric model parameters R_0, R_1,K τ_1. If the parameters are not correct or vary over time the estimation error increases. DEKF can compensate this type of problem by updating the ECM parameters over time[73]. Simultaneously updating the parameters and *SOC* allows a more detailed assessment of battery aging, and consequently provides a better estimate of *SOH*. Dual estimation emphasizes the interdependent link between *SOC* and *SOH* under different battery working conditions [13, 26, 57].

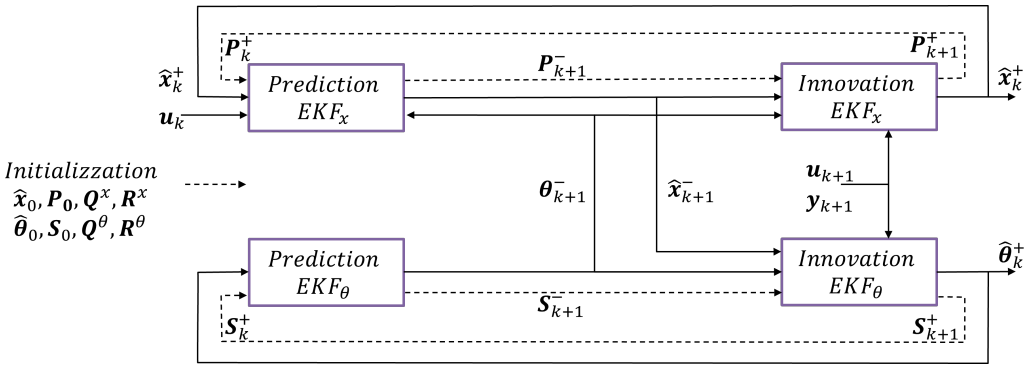

Figure 3.22: Graphic representation of the Dual Extended Kalman Filter [57]

The DEKF consist of two separate EKF used to estimate both state, and parameter values simultaneously [77]. Estimation is done on two separate filters to simplify operations between matrices. Considering then that we want to find both the states $\mathbf{x}_k$ and the parameters θ_k of a nonlinear time-discrete dynamical system, we use a first filter EKF_x that will estimate the state (fast-varying state $\boldsymbol{x}_k$), and a second filter EKF_θ that will estimate the parameters (slow-varying state $\boldsymbol{\theta}_k$).

State estimations The equations for implementing EKF_x are given below.

$$\begin{aligned} \boldsymbol{x}_{k+1} &= \boldsymbol{f}(\hat{\boldsymbol{x}}_k, \boldsymbol{u}_k, \boldsymbol{\theta}_k) + \boldsymbol{q}_k^x \\ \boldsymbol{y}_k &= \boldsymbol{h}(\hat{\boldsymbol{x}}_k, \boldsymbol{u}_k, \boldsymbol{\theta}_k) + \boldsymbol{r}_k^x \end{aligned} \tag{3.64}$$

$\mathbf{x}(t)$ is the state vector, $\boldsymbol{\theta}(t)$ is the parameters vector, $\mathbf{u}(t)$ is the input vector and $\mathbf{y}(t)$ is the output vector. While the functions **f** and **h** are the state transition function and the output function respectively. Where $\boldsymbol{x}(t) \in \mathbb{R}^n$, $\boldsymbol{y}(t) \in \mathbb{R}^m$, $\boldsymbol{u}(t) \in \mathbb{R}^l$. The term $\boldsymbol{q}_k^x$ zero means stochastic type noise that considers disturbances on the system states, while the term $\boldsymbol{r}_k^x$ represents noise caused by the measurement on the output $\boldsymbol{y}_k$. Both are zero mean stochastic disturbances with covariance matrices $\boldsymbol{Q}^x$ and $\boldsymbol{P}^x$.

$$\mathbb{E} = [q_n {q_k}^T] = \begin{cases} \mathbf{Q}_k & n = k \\ 0 & n \neq k \end{cases} \tag{3.65}$$

$$\mathbb{E} = [r_n {r_k}^T] = \begin{cases} \mathbf{R}_k & n = k \\ 0 & n \neq k \end{cases} \tag{3.66}$$

Assuming the following domains:

$$\boldsymbol{x}_k \in \mathbb{R}^n, \boldsymbol{y}_k \in \mathbb{R}^m, \boldsymbol{u}_k \in \mathbb{R}^l, \theta_k \in \mathbb{R}^i$$

Also for the dual filter, it is necessary to perform a first-order Taylor linearization that approximates at each step the nonlinear system with a linear time-varying system at the considered point.

$$\mathbf{F}_k = \left. \frac{\partial \boldsymbol{f}(\boldsymbol{x}_k, \boldsymbol{u}_k, \boldsymbol{\theta}_k)}{\partial \boldsymbol{x}} \right|_{\boldsymbol{x}=\hat{\boldsymbol{x}}_k} \tag{3.67}$$

$$\mathbf{H}_k = \left. \frac{\partial \boldsymbol{h}(\boldsymbol{x}_k, \boldsymbol{u}_k, \boldsymbol{\theta}_k)}{\partial \boldsymbol{x}} \right|_{\boldsymbol{x}=\hat{\boldsymbol{x}}_k^-} \tag{3.68}$$

The two non-linear functions (3.21) and (3.22) are then approximated using the two Taylor expansions:

$$f(x_k, u_k, \theta_k) \approx f(\hat{x}_k, u_k, \theta_k) + \mathbf{F}_k(x_k - \hat{x}_k) \tag{3.69}$$

$$h(x_k, u_k, \theta_k) \approx h(\hat{x}_k, u_k, \theta_k) + \mathbf{H}_k(x_k - \hat{x}_k) \tag{3.70}$$

For obtaining the new process equation, and the new measurement equation:

$$x_{k+1} = \mathbf{F}_k x_k + f(\hat{x}_k, u_k, \theta_k) - \mathbf{F}_k \hat{x}_k + q_k \tag{3.71}$$

$$y_k = \mathbf{H}_k x_k + h(\hat{x}_k, u_k, \theta_k) - \mathbf{H}_k \hat{x}_k + r_k \tag{3.72}$$

Parameters estimations The equations for implementing EKF_θ are given below.

$$\theta_{k+1} = \theta_k + q_k^\theta \tag{3.73}$$

$$d_k = h(x_k, u_k, \theta_k) + r_k^\theta \tag{3.74}$$

The modeled parameters in (3.73) and (3.74) show variation caused by zero mean Gaussian white noise, both described by the $\boldsymbol{Q}$ and $\boldsymbol{R}$ covariance matrices, respectively.

Errors that come from noise generated by the measurement sensors and the model. In (3.73) the parameters are estimated as constants with small perturbations in addiction, while (3.74) expresses the output of the system and after being linearized will take the following form:

$$d_k = H_k^\theta x_k + h(\hat{x}_k, u_k, \theta_k) - H_k^\theta \hat{x}_k + r_k^\theta \tag{3.75}$$

Where the term $\mathbf{H}_k^\theta$ is a matrix that will represent the output updates based on the variation of the parameters.

$$\mathbf{H}_k^{\theta} = \left.\frac{\partial \boldsymbol{h}(\hat{\boldsymbol{x}}_{k+1}^{-}, \boldsymbol{u}_{k+1}, \boldsymbol{\theta}_k)}{\partial \boldsymbol{\theta}}\right|_{\boldsymbol{\theta}=\hat{\boldsymbol{\theta}}_{k+1}^{-}} \tag{3.76}$$

Being a matrix that expresses the dynamics of the parameters it will also be influenced by the previous states of the system $\hat{\boldsymbol{x}}_k^{+}$ and $\hat{\boldsymbol{x}}_{k+1}^{-}$. It is then necessary to perform a total derivative, which involves three recursively computed derivatives, initialized to zero and then updated at each step.

$$\begin{aligned}
\hat{H}_k^{\theta} = \left.\frac{\partial \boldsymbol{h}(\hat{\boldsymbol{x}}_{k+1}^{-}, \boldsymbol{u}_{k+1}, \boldsymbol{\theta}_k)}{\partial \boldsymbol{\theta}}\right|_{\boldsymbol{\theta}=\hat{\boldsymbol{\theta}}_{k+1}^{-}} &= \frac{\partial \boldsymbol{h}(\hat{\boldsymbol{x}}_{k+1}^{-}, \boldsymbol{u}_{k+1}, \boldsymbol{\theta}_k)}{\partial \boldsymbol{\theta}} + \frac{\partial \boldsymbol{h}(\hat{\boldsymbol{x}}_{k+1}^{-}, \boldsymbol{u}_{k+1}, \boldsymbol{\theta}_k)}{\partial \hat{\boldsymbol{x}}_{k+1}^{-}} \frac{d\hat{\boldsymbol{x}}_{k+1}^{-}}{d\boldsymbol{\theta}} \\
\frac{d\hat{\boldsymbol{x}}_{k+1}^{-}}{d\boldsymbol{\theta}} &= \frac{\partial \boldsymbol{f}(\hat{\boldsymbol{x}}_k^{+}, \boldsymbol{u}_k, \boldsymbol{\theta}_k)}{\partial \boldsymbol{\theta}} + \frac{\partial \boldsymbol{f}(\hat{\boldsymbol{x}}_k^{+}, \boldsymbol{u}_k, \boldsymbol{\theta}_k)}{\partial \hat{\boldsymbol{x}}_k^{+}} \frac{d\hat{\boldsymbol{x}}_k^{+}}{d\boldsymbol{\theta}} \\
\frac{d\hat{\boldsymbol{x}}_k^{+}}{d\boldsymbol{\theta}} &= \frac{d\hat{\boldsymbol{x}}_k^{-}}{d\boldsymbol{\theta}} - \boldsymbol{G}_k^{x} \frac{d\boldsymbol{h}(\hat{\boldsymbol{x}}_k^{-}, \boldsymbol{u}_k, \boldsymbol{\theta}_k)}{d\boldsymbol{\theta}}
\end{aligned} \tag{3.77}$$

At initial step $k = 0$, the terms are initialized to 0.

Algorithm The Dual Extended Kalman Filter theory can be applied following the same sequence of the linear case represented in Fig. 3.23, briefly described as follows.

1. **Initialization**: The initialization is done for both EKF, and the state and parameter values are chosen as close as possible to the expected value.

$$\begin{aligned}
\hat{\boldsymbol{x}}_0^{+} &= \mathbb{E}[\boldsymbol{x}_0] \\
P_{k,0}^{+} &= \mathbb{E}[(\boldsymbol{x}_0 - \hat{\boldsymbol{x}}_0^{+})(\boldsymbol{x}_0 - \hat{\boldsymbol{x}}_0^{+})^T]
\end{aligned} \tag{3.78}$$

$$\begin{aligned}
\hat{\boldsymbol{\theta}}_0^{+} &= \mathbb{E}[\boldsymbol{x}_0] \\
S_{k,0}^{+} &= \mathbb{E}[(\boldsymbol{x}_0 - \hat{\boldsymbol{x}}_0^{+})(\boldsymbol{x}_0 - \hat{\boldsymbol{x}}_0^{+})^T]
\end{aligned} \tag{3.79}$$

2. **Prediction**: The prediction step allows through the state transaction function to estimate the current value of the state and parameters, using the information of the previous cycle. The uncertainty on the estimate of the state and parameters is also calculated through the covariance matrices.

$$\begin{aligned}
\boldsymbol{x}_k^{-} &= \boldsymbol{f}(\hat{\boldsymbol{x}}_{k-1}^{+}, \boldsymbol{u}_k, \boldsymbol{\theta}_k^{-}) \\
\boldsymbol{P}_{x,k}^{-} &= \boldsymbol{F}_{k-1} \boldsymbol{P}_{x,k-1}^{+} \boldsymbol{F}_{k-1}^{T} + \boldsymbol{Q}^{x}
\end{aligned} \tag{3.80}$$

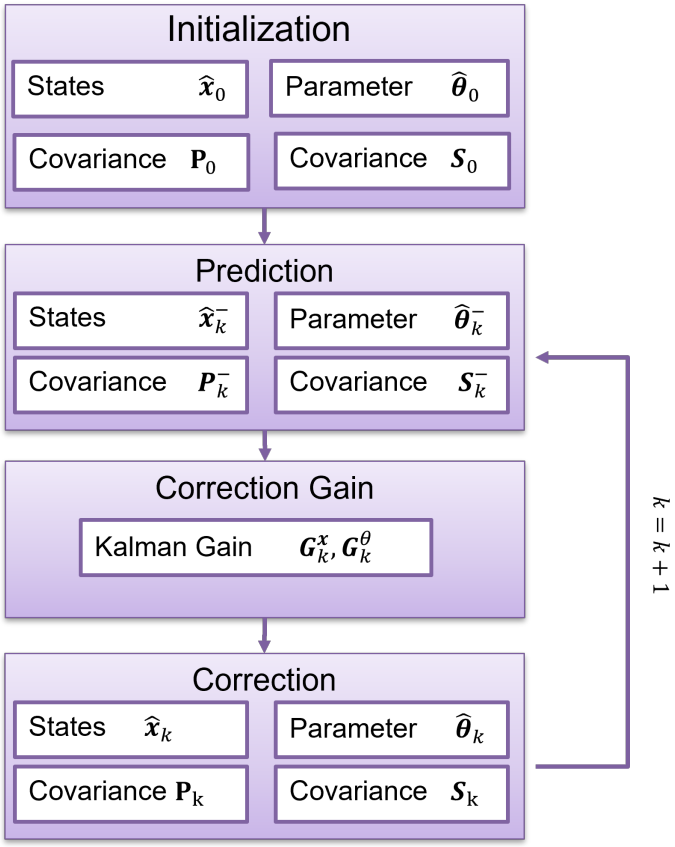

Figure 3.23: Sequence of the prediction and update steps in the DEKF estimation process [36]

$$\begin{aligned} \hat{\boldsymbol{\theta}}_k^- &= \hat{\boldsymbol{\theta}}_{k-1}^- \\ \boldsymbol{S}_{\theta,k}^- &= \boldsymbol{S}_{\theta,k-1}^+ + \boldsymbol{Q}^\theta \end{aligned} \tag{3.81}$$

3. **Correction Gain**: The value of both the Kalman gain are calculated based on the values of the covariance matrices just estimated

$$\boldsymbol{G}_k^x = \boldsymbol{P}_{x,k}^-(\boldsymbol{H}_k^x)^T[\boldsymbol{H}_k^x\boldsymbol{P}_{x,k}^-(\boldsymbol{H}_k^x)^T + \boldsymbol{R}_k^x]^{-1} \tag{3.82}$$

$$\boldsymbol{G}_k^\theta = \boldsymbol{S}_{\theta,k}^-(\boldsymbol{H}_k^\theta)^T[\boldsymbol{H}_k^\theta\boldsymbol{S}_{\theta,k}^-(\boldsymbol{H}_k^\theta)^T + \boldsymbol{R}_k^\theta]^{-1} \tag{3.83}$$

4. **Correction**: It is possible to estimate the output using the output function, using the values estimated during the prediction phase, then through the output measurement

and the newly calculated gain it is possible to correct the state and the estimated parameters.

$$\hat{\boldsymbol{y}}_k = \boldsymbol{h}(\hat{\boldsymbol{x}}_k, \boldsymbol{u}_k, \hat{\boldsymbol{\theta}}_k) + \boldsymbol{r}_k^x \tag{3.84}$$

Status update:

$$\begin{aligned} \hat{\boldsymbol{x}}_k^+ &= \hat{\boldsymbol{x}}_k^- + \boldsymbol{G}_k^x[\boldsymbol{y}_k - \hat{\boldsymbol{y}}_k] \\ \mathbf{P}_{x,k} &= (\mathbf{I} - \mathbf{G}_k^x \mathbf{H}_k^x)\mathbf{P}_{x,k}^- \end{aligned} \tag{3.85}$$

Parameters update:

$$\begin{aligned} \hat{\boldsymbol{\theta}}_k^+ &= \hat{\boldsymbol{\theta}}_k^- + \boldsymbol{G}_k^\theta[\boldsymbol{y}_k - \hat{\boldsymbol{y}}_k] \\ \mathbf{S}_{\theta,k} &= (\mathbf{I} - \mathbf{G}_k^\theta \mathbf{H}_k^\theta)\mathbf{S}_{\theta,k}^- \end{aligned} \tag{3.86}$$

Both updated state $\hat{\boldsymbol{x}}_k^+$ and updated parameters $\hat{\boldsymbol{\theta}}_k^+$ will be used at the following time interval $k+1$ in the prediction step, as represented in the flowchart of Fig. 3.23

3.3.2 Battery applications

This section will show the results obtained using DEKF for the determination of *SOC* and R_0, The model that is used for comparison is the single polarization model, shown in the section 1.4.4 whose scheme and equations it are given below.

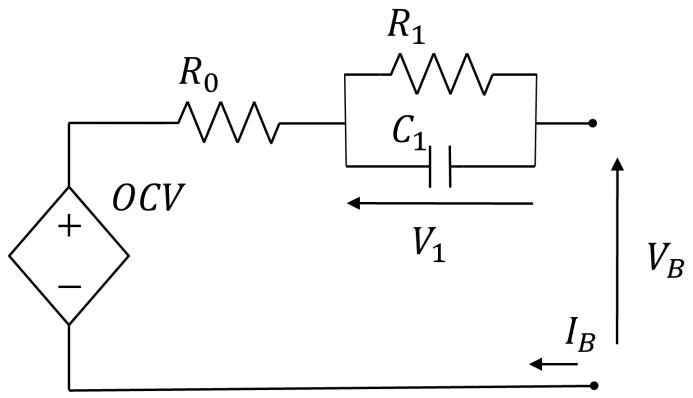

Figure 3.24: Single polarization model

$$\begin{aligned} V_{B_k} &= OCV(SOC_k) - R_0(SOC_k) \times i_{B_k} - V_{1_k} \\ V_{1_{k+1}} &= V_{1_k} \times (e^{-\frac{\Delta t}{\tau_1(SOC_k)}}) + R_1(SOC_K) \times i_{B_k} \times (1 - e^{-\frac{\Delta t}{\tau_1(SOC_k)}}) \\ SOC_{k+1} &= SOC_k - \frac{i_{B_k} \times \Delta t}{C_{nom}} \end{aligned} \tag{3.87}$$

The voltage on the capacitor V_1, and the *SOC* are chosen as state variables, these variables in fact represent a memory of the system and for this reason they can be used in the input state output representation. The battery parameters R_0, R_1, τ_1 are chosen as parameters. The input variable is the battery current i_B, while the temperature is not taken into account, and is considered as a disturbance of the system. The measurable output is the battery voltage V_B.

By summarizing, the state variable vector $\boldsymbol{x}$ is defined as:

$$\mathbf{x} = \begin{bmatrix} V_1 \\ SOC \end{bmatrix} \tag{3.88}$$

The parameters vector $\boldsymbol{\theta}$ is defined as:

$$\boldsymbol{\theta} = \begin{bmatrix} R_0 \\ R_1 \\ \tau_1 \end{bmatrix} \tag{3.89}$$

The input variable vector **u** is defined by the cell current i_B only:

$$\boldsymbol{u} = u = [i_B] \tag{3.90}$$

And the output variable vector $\boldsymbol{y}$ is defined by the cell voltage v_B only:

$$\boldsymbol{y} = y = [v_B] \tag{3.91}$$

The EKF estimator is implemented by using the notation and procedure introduced in Section 3.3.1 and the discretization time interval Δt. From the SP circuit of Fig. 3.24, the discretized state variable $\boldsymbol{x} = f(\boldsymbol{x}_k, u_k, \boldsymbol{\theta}_k)$ is expressed by (3.92). With the aim of reducing the complexity of the system and therefore the complexity of the linearization process the eq: (3.87), has been approximated using the first order Taylor approximation.

$$\boldsymbol{f}(\boldsymbol{x}_k, u_k, \boldsymbol{\theta}_k) = \begin{bmatrix} V_{1_k}(1 - \frac{\Delta t}{\tau_{1_k}}) + \frac{\Delta t}{\tau_{1_k}} R_{1_k} i_{B_k} \\ SOC_k - \frac{i_{B_k} \times \Delta t}{C_{nom}} \end{bmatrix} \tag{3.92}$$

The discretized output variable $y_k = h(\boldsymbol{x}_k, u_k, \boldsymbol{\theta}_k)$ is derived by the SP circuit as:

$$\boldsymbol{h}(\boldsymbol{x}_k, u_k, \boldsymbol{\theta}_k) = [OCV_k - V_{1_k} - R_{0_k} i_{B_k}] \tag{3.93}$$

The open circuit voltage OCV of the battery is considered a function of the SOC only. In order to implement the DEKF, it is necessary to make explicit the function $OCV - SOC$, in order to then calculate its derivative at the considered point. The equation used is the one presented in the modeling chapter, eq: (2.36), given below.

$$\begin{aligned} OCV(SOC) =& a + bSOC + cSOC^2 + \frac{d}{SOC} + \\ &+ e\ln(SOC) + f\ln(1 - SOC) \end{aligned} \tag{3.94}$$

$$\mathbf{F}_k = \frac{\partial \boldsymbol{f}(\boldsymbol{x}_k, u_k, \boldsymbol{\theta}_k)}{\partial \boldsymbol{x}} = \begin{bmatrix} \frac{\partial V_1(\boldsymbol{x}_k, u_k, \boldsymbol{\theta}_k)}{\partial V_1} & \frac{\partial V_1(\boldsymbol{x}_k, u_k, \boldsymbol{\theta}_k)}{\partial SOC} \\ \frac{\partial SOC(\boldsymbol{x}_k, u_k, \boldsymbol{\theta}_k)}{\partial V_1} & \frac{\partial SOC(\boldsymbol{x}_k, u_k, \boldsymbol{\theta}_k)}{\partial SOC} \end{bmatrix} = \begin{bmatrix} (1 - \frac{\Delta t}{\tau_{1_{k-1}}}) & 0 \\ 0 & 1 \end{bmatrix} \tag{3.95}$$

$$\mathbf{H}_k^x = \frac{\partial \boldsymbol{h}(\boldsymbol{x}_k, u_k, \boldsymbol{\theta}_k)}{\partial \boldsymbol{x}} = \begin{bmatrix} \frac{\partial V_B(\boldsymbol{x}_k, u_k, \boldsymbol{\theta}_k)}{\partial V_1} & \frac{\partial V_B(\boldsymbol{x}_k, u_k, \boldsymbol{\theta}_k)}{\partial SOC} \end{bmatrix} = \begin{bmatrix} -1 & \frac{\partial OCV(SOC)}{\partial SOC} \end{bmatrix} \tag{3.96}$$

$$\boldsymbol{H}_k^\theta = \frac{\partial \boldsymbol{h}(\hat{\boldsymbol{x}}_{k+1}^-, \boldsymbol{u}_{k+1}, \boldsymbol{\theta}_k)}{\partial \boldsymbol{\theta}}\bigg|_{\boldsymbol{\theta}=\hat{\boldsymbol{\theta}}_{k+1}^-} = \frac{\partial \boldsymbol{h}(\hat{\boldsymbol{x}}_{k+1}^-, \boldsymbol{u}_{k+1}, \boldsymbol{\theta}_k)}{\partial \boldsymbol{\theta}} + \frac{\partial \boldsymbol{h}(\hat{\boldsymbol{x}}_{k+1}^-, \boldsymbol{u}_{k+1}, \boldsymbol{\theta}_k)}{\partial \hat{\boldsymbol{x}}_{k+1}^-} \frac{d\hat{\boldsymbol{x}}_{k+1}^-}{d\boldsymbol{\theta}} \tag{3.97}$$

To calculate this term, it is necessary to evaluate the three differential equations separately.

The partial derivative of the output over the parameters is:

$$\frac{\partial \boldsymbol{h}(\hat{x}_{k+1}^-, u_{k+1}, \boldsymbol{\theta})}{\partial \boldsymbol{\theta}}\bigg|_{\boldsymbol{\theta}=\hat{\boldsymbol{\theta}}_{k+1}^-} = \begin{bmatrix} \frac{\partial V_b}{\partial R_0} & \frac{\partial V_b}{\partial R_1} & \frac{\partial V_b}{\partial \tau_1} \end{bmatrix} = \begin{bmatrix} -i_b & 0 & 0 \end{bmatrix} \tag{3.98}$$

The partial derivative of the output over the parameters states is:

$$\frac{\partial \mathbf{f}(\hat{\boldsymbol{x}}_{k+1}^-, u_{k+1}, \boldsymbol{\theta})}{\partial \hat{\boldsymbol{x}}_{k+1}^-}\bigg|_{\boldsymbol{\theta}=\hat{\boldsymbol{\theta}}_{k+1}^-} = \begin{bmatrix} \frac{\partial V_b}{\partial v_1} & \frac{\partial V_b}{\partial SOC} \end{bmatrix} = \begin{bmatrix} -1 & \frac{\partial OCV(SOC)}{\partial SOC} \end{bmatrix} \tag{3.99}$$

$$\frac{d\hat{\boldsymbol{x}}_{k+1}^-}{d\boldsymbol{\theta}} = \frac{\partial \boldsymbol{f}(\hat{\boldsymbol{x}}_k^+, u_k, \boldsymbol{\theta}_k)}{\partial \boldsymbol{\theta}} + \frac{\partial \boldsymbol{f}(\hat{\boldsymbol{x}}_k^+, u_k, \boldsymbol{\theta}_k)}{\partial \hat{\boldsymbol{x}}_k^+} \frac{d\hat{\boldsymbol{x}}_k^+}{d\boldsymbol{\theta}} \tag{3.100}$$

The eq. (3.100) is divided in two contributes. The derivative of the states over the parameters is:

$$\frac{\partial \boldsymbol{f}(\hat{\boldsymbol{x}}_{k+1}^+, u_{k+1}, \boldsymbol{\theta}_k)}{\partial \boldsymbol{\theta}}\bigg|_{\boldsymbol{\theta}=\hat{\boldsymbol{\theta}}_{k+1}^-} = \begin{bmatrix} \frac{\partial V_1}{\partial R_0} & \frac{\partial V_1}{\partial R_1} & \frac{\partial V_1}{\partial \tau_1} \\ \frac{\partial SOC}{\partial R_0} & \frac{\partial SOC}{\partial R_1} & \frac{\partial SOC}{\partial \tau_1} \end{bmatrix} = \begin{bmatrix} 0 & \frac{i_B \Delta t}{\tau_1} & \frac{V_1 \Delta t}{\tau_1^2} - \frac{i_B \Delta t R_1}{\tau_1^2} \\ 0 & 0 & 0 \end{bmatrix} \tag{3.101}$$

The derivative of the states over the states is:

$$\frac{\partial \boldsymbol{f}(\hat{\boldsymbol{x}}_k^+, u_k, \boldsymbol{\theta}_k)}{\partial \hat{\boldsymbol{x}}_k^+}\bigg|_{\boldsymbol{\theta}=\hat{\boldsymbol{\theta}}_{k+1}^-} = \begin{bmatrix} \frac{\partial V_1}{\partial V_1} & \frac{\partial V_1}{\partial SOC} \\ \frac{\partial SOC}{\partial V_1} & \frac{\partial SOC}{\partial SOC} \end{bmatrix} = \begin{bmatrix} 1 - \frac{\Delta t}{\tau_1} & 0 \\ 0 & 1 \end{bmatrix} \tag{3.102}$$

3.3.3 Experimental Results

To test the Dual Extended Kalman Filter, a power profile was used. The used profile is obtained from a standardized driving cycle for passenger cars (WLTC). As the driving cycle is defined as a speed profile, the reference power was calculated by introducing the vehicle model [42]. In other words, the cycle represents the hypothetical operation of the cell in an automotive application. The reference power profile has been applied to the real cell and the voltage and current were measured throughout the test. The tests begins with fully charged cells, and stops when the discharge cut-off voltage is reached. The three power profiles used are the same as those used to test the EKF, in order to compare the results obtained.

Once the actual cell usage profiles were obtained, they were imported into Matlab environment, where the DEKF algorithms were implemented. The input and output vectors used in the filter are real data, so that also the non-ideality of the measuring instruments, as well as the variation of cell temperature, are considered.

Tests were conducted on cells from different manufacturers. Two cells are considered high energy and one high power. The cells used are LG M50T, Samsung S50E and Molicel P42A, their specifications have been summarized in the table 3.12. In addition, the cells have different SOH values, to verify that the estimate of SOC, and especially of R_0 is accurate for different aging values.

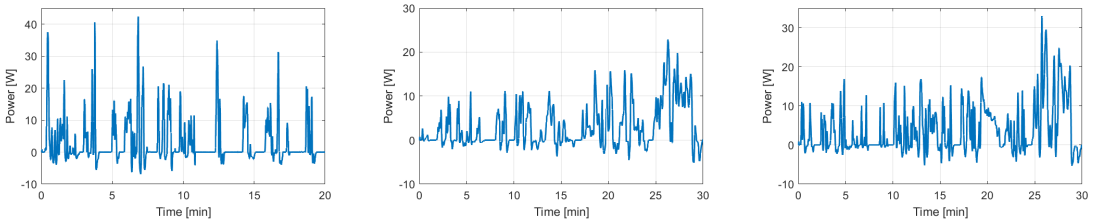

(a) Cycle A (b) Cycle B (c) Cycle C

Figure 3.25: Three used profile, (a) Cycle A: Energy = 0.951 [Wh], Max power = 42.351 [W], Mean Power = 2.853 [W]; (b) Cycle B: Energy = 0.593 [Wh], Max power = 15.847 [W], Mean Power = 1.780 [W]; (c) Cycle C: Energy = 0.869 [Wh], Max power = 17.327 [W], Mean Power = 2.607 [W]

Figure 3.26: Cells examined from left to right: LG M50T, Samsung 50E, Molicel P42A

Table 3.12: Nominal data of the cells selected for the experimental tests

Manufacturer	LG	SAMSUNG	MOLICEL
Model	INR21700 50T	INR21700 50E	INR21700 P42A
Chemistry	NMC	NMC	NMC
Capacity [Ah]	5	4.9	4.2
Energy [Wh]	18.15	17.6	15.1
Weight [g]	70	70	70

R0 - SOC

The voltage error is calculated between the real voltage and the filter estimated one, the value is normalized by the nominal voltage of each cell, as in (3.103) and (3.104), (3.105), (3.105), (3.107) and (3.108).

The *SOC* is not directly measurable. The capacity value measured by the wattmeter was used to determine the *SOC* value, and normalized for the value at the end of discharge. Since all tests end when the voltage cut-off is reached, the cell is considered to have reached $SOC = 0$.

To compare the estimated value of the internal resistance R_0, the cell model described in the previous chapter was used. The model used as a reference to estimate the value of R_0 is considered reliable, and has already been validated previously. The current measured in the laboratory test was used as input in order to obtain the resistance trend in time as a function of *SOC*, for that specific *SOH* value. The interaction between the various systems is shown in Fig. 3.27.

The MAE and RMSE values were calculated for each test for both SOC and R_0, and all results are reported in Tab. 3.13, Tab. 3.14, Tab. 3.15. All trends of SOC, and R_0 with their respective errors are reported below as a function of time.

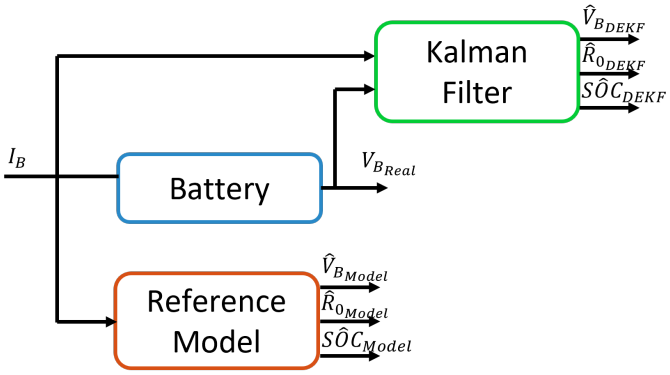

Figure 3.27: Block diagram of the DEKF validation procedure

$$V_{Mean} = \frac{\frac{1}{n}\sum |v_{B_{real}} - \hat{v}_{B_{DEKF}}|}{v_{nom}}. \tag{3.103}$$

$$V_{RMS} = \frac{\sqrt[2]{\frac{1}{n}\sum (v_{B_{real}} - \hat{v}_{B_{DEKF}})^2}}{v_{nom}} \tag{3.104}$$

$$SOC_{Mean} = \frac{1}{n}\sum |SOC_{model} - S\hat{O}C_{DEKF}|. \tag{3.105}$$

$$SOC_{RMS} = \sqrt[2]{\frac{1}{n}\sum (SOC_{model} - S\hat{O}C_{DEKF})^2} \tag{3.106}$$

$$R_{Mean} = \frac{\frac{1}{n}\sum |R_{0_{model}} - \hat{R}_{0_{DEKF}}|}{R_{0_{model}}|_{SOC=50\%}} \tag{3.107}$$

$$R_{RMS} = \frac{\sqrt[2]{\frac{1}{n}\sum (R_{0_{model}} - \hat{R}_{0_{DEKF}})^2}}{R_{0_{model}}|_{SOC=50\%}} \tag{3.108}$$

Table 3.13: LG - M50T DEKF SOC and R0 estimation performance

Test type	SOH	Voltage		SOC		R0	
		MAE	RMSE	MAE	RMSE	MAE	RMSE
A	100 %	17.12 ppm	156.32 ppm	0.64 %	0.81 %	6.35 %	10.27 %
	50 %	7.85 ppm	64.88 ppm	0.62 %	0.82 %	9.90 %	11.52 %
	0 %	12.35 ppm	114.80 ppm	1.10 %	1.25 %	8.62 %	11.23 %
B	100 %	-5.98 ppm	431.73 ppm	1.04 %	1.26 %	7.06 %	10.78 %
C	100 %	0.64 ppm	341.44 ppm	0.66 %	0.78 %	5.29 %	11.34 %

Table 3.14: Samsung - S50E DEKF SOC and R0 estimation performance

Test type	SOH	Voltage		SOC		R0	
		MAE	RMSE	MAE	RMSE	MAE	RMSE
A	100 %	-8.99 ppm	232.00 ppm	0.23 %	0.27 %	5.29 %	10.20 %
	50 %	5.56 ppm	334.21 ppm	0.26 %	0.28 %	8.05 %	15.88 %
	0 %	23.95 ppm	200.32 ppm	0.18 %	0.19 %	16.04 %	17.06 %
B	0 %	9.54 ppm	138.20 ppm	0.08 %	0.09 %	20.80 %	21.57 %
C	0 %	-2.40 ppm	200.74 ppm	0.14 %	0.19 %	19.64 %	20.72 %

Table 3.15: Molicel - P42A DEKF SOC and R0 estimation performance

Test type	SOH	Voltage		SOC		R0	
		MAE	RMSE	MAE	RMSE	MAE	RMSE
A	100 %	-21.05 ppm	562.92 ppm	0.88 %	1.14 %	10.69 %	24.22 %
B	100 %	-20.54 ppm	298.62 ppm	0.94 %	1.15 %	13.13 %	22.00 %
C	100 %	-13.47 ppm	355.48 ppm	0.54 %	0.65 %	12.62 %	21.80 %

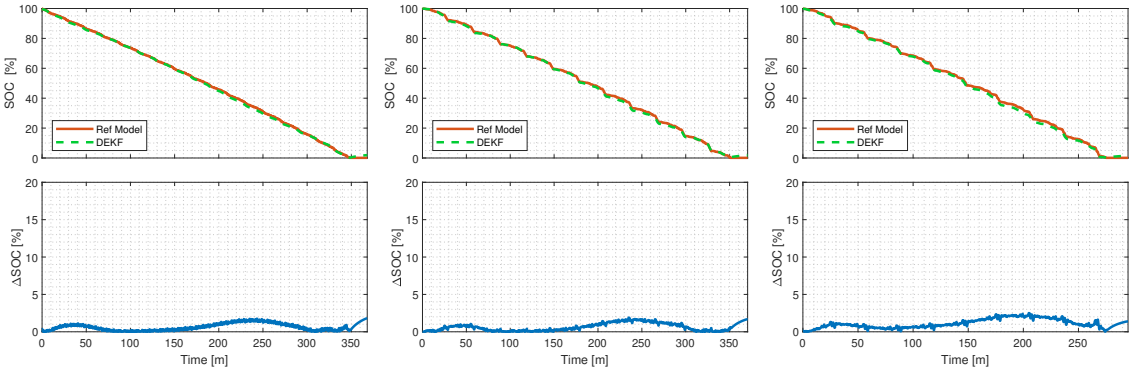

(a) SOH 100% Cycle A (b) SOH 50% Cycle A (c) SOH 0% Cycle A

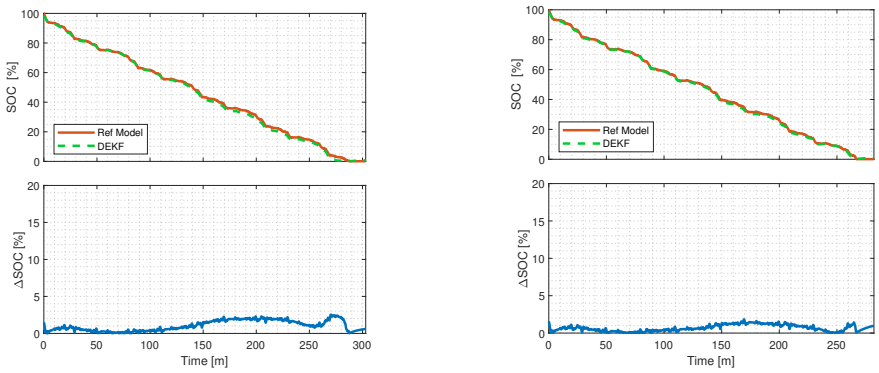

(d) SOH 100% Cycle B (e) SOH 100% Cycle C

Figure 3.28: tests results, LG - M50T DEKF-SOC estimation performance

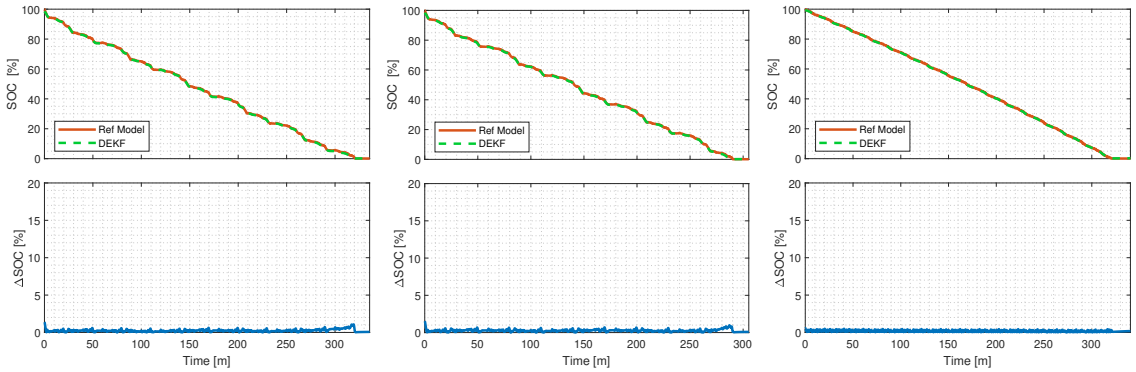

(a) SOH 100% Cycle A (b) SOH 50% Cycle A (c) SOH 0% Cycle A

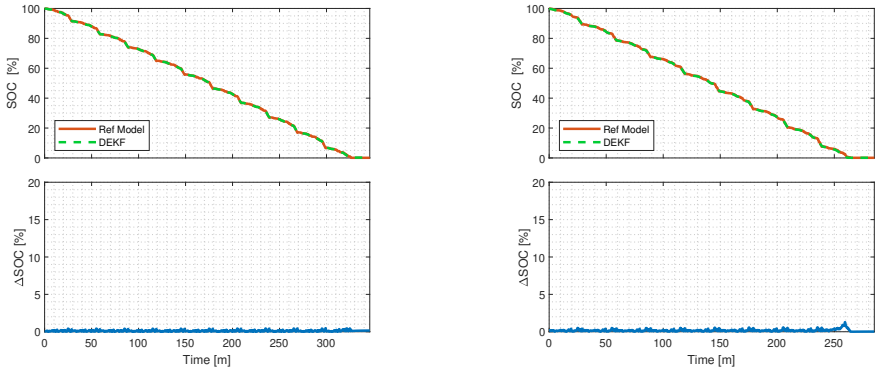

(d) SOH 0% Cycle B (e) SOH 0% Cycle C

Figure 3.29: Tests results, Samsung - S50E DEKF-SOC estimation performance

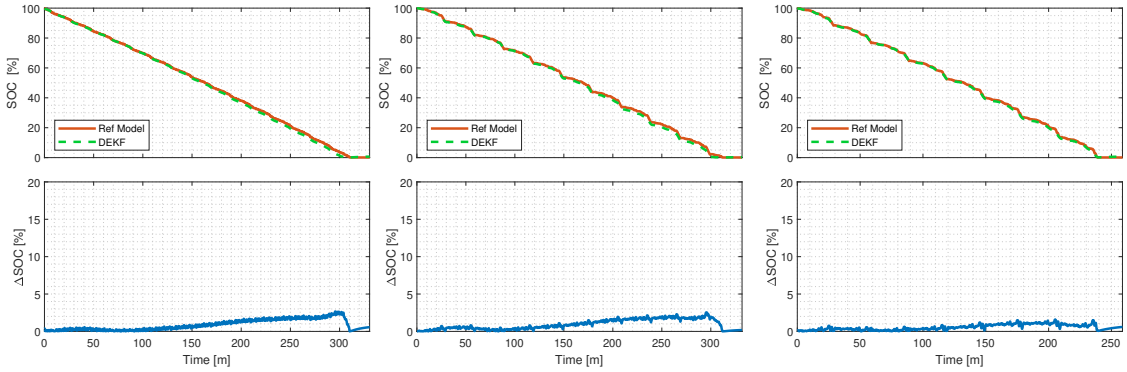

(a) SOH 100% Cycle A (b) SOH 100% Cycle B (c) SOH 100% Cycle C

Figure 3.30: Tests results, Molicel - P42A DEKF-SOC estimation performance

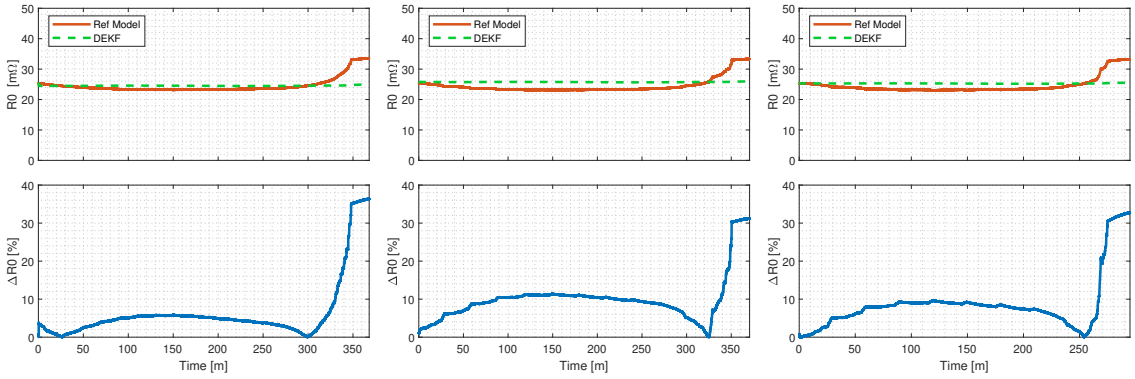

(a) SOH 100% Cycle A (b) SOH 50% Cycle A (c) SOH 0% Cycle A

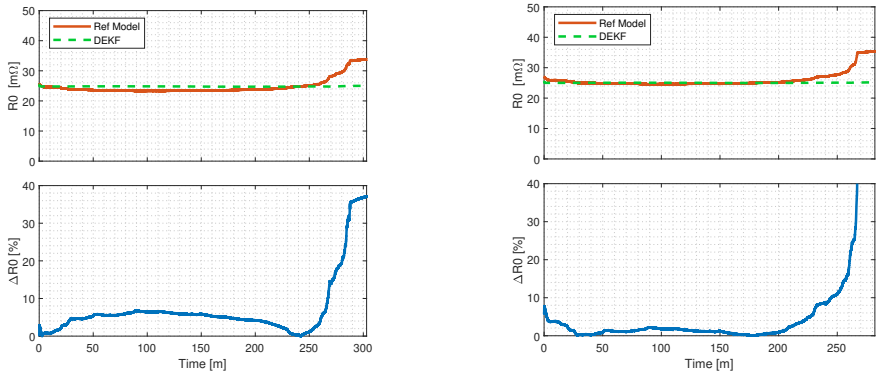

(d) SOH 100% Cycle B (e) SOH 100% Cycle C

Figure 3.31: tests results, LG - M50T DEKF-R_0 estimation performance

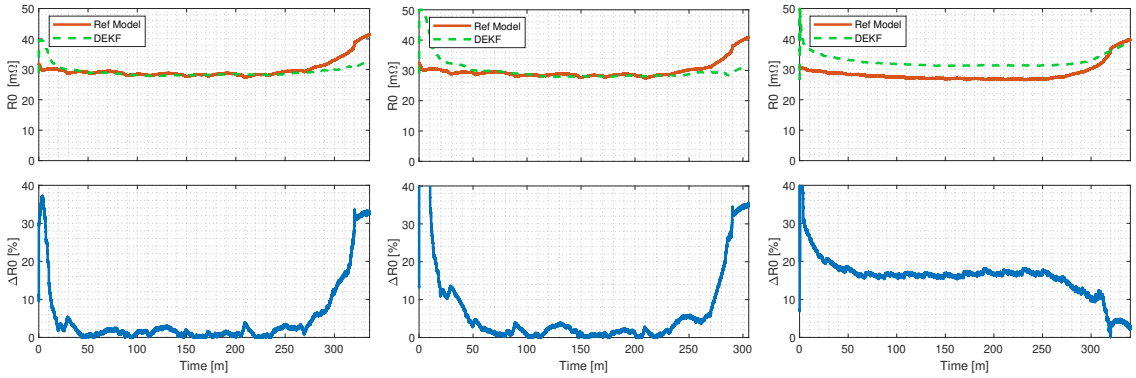

(a) SOH 100% Cycle A (b) SOH 50% Cycle A (c) SOH 0% Cycle A

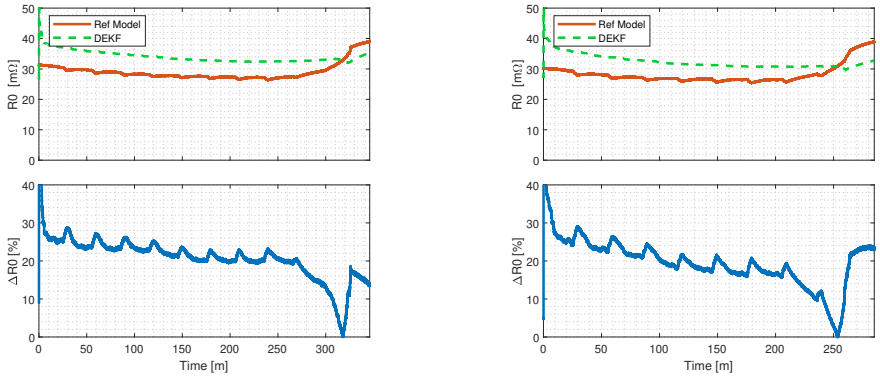

(d) SOH 0% Cycle B (e) SOH 0% Cycle C

Figure 3.32: Tests results, Samsung - S50E DEKF-R_0 estimation performance

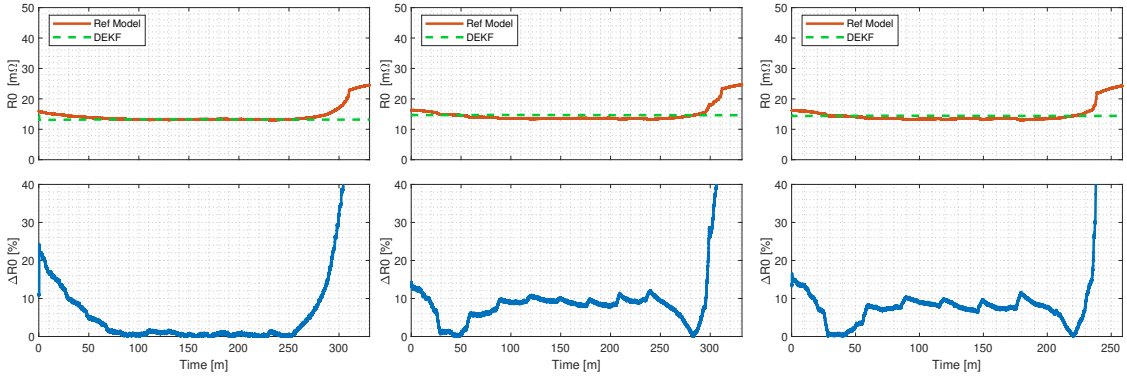

(a) SOH 100% Cycle A (b) SOH 100% Cycle B (c) SOH 100% Cycle C

Figure 3.33: Tests results, Molicel - P42A DEKF-R_0 estimation performance

The Dual Extended Kalman Filter shows very good results on voltage estimation, and on *SOC* estimation, however, the error on R_0 estimation is higher than that obtained with the Extended Kalman Filter.

The accuracy on the *SOC* estimation shows the potential of the DEKF, obtaining an error on the estimate always lower than 1%. Given the result obtained it is natural to think of using this method to indirectly estimate the battery capacity and consequently the *SOH* using the definition based on the residual capacity.

On the other hand this method presents an inadequate accuracy on the estimation of the internal resistance R_0.Such a high error on parameter estimation may be due to the sub-optimal choice of values to be included in the covariance matrices, which with more precise tuning could have a higher accuracy.

Conclusions

This project develops the methodologies for the realization of a battery model and the bases for the estimation of its state.

The first part traces overview of the world of batteries introducing the types and the problems that concern them. An overview of the control system was given by presenting what are the main functions of the BMS. The concept of equivalent electric circuit has been taken into account, describing the most common models in literature. And finally, it has been introduced the problem of battery state determination, defining the possible states reported by in literature.

After a first introductory part, it has been presented one of the two parts of which the project is composed. The realization of a model that has affected a large part of these last years has been essential to understand the phenomena that occur inside the cells, and to to test the various mechanisms of deterioration that occur in batteries. An accurate model was essential to be able to simulate and test the algorithms before using them on the real system. Having developed a battery model has made it possible to generate a large amount of data that will be used to create increasingly accurate machine learning models without requiring hours and hours of real testing.

State estimation is the second topic dealt with end a particular emphasis has been placed on the estimation of the state of charge and on the estimation of the state of health. The state of charge was analysed as a starting point to set targets in line with the literature, as this topic is now well established. Subsequently a lot of time has been spent on the development of algorithms capable of determining the state of health. The methods performing best in terms of accuracy were those based on Kalman filters in this dissertation the results of EKF and DEKF have been shown. The DEKF, has a higher complexity

than the EKF, for this reason the field of application is more oriented to the implementation in the cloud for later processing of data while, on the other hand, the EKF can be implemented on a microcontroller and can be used in real-time.

The possibility of analysing some methods based on particle filters is not excluded. In addition, using the model in combination with data obtained from laboratory tests, the possibility of using algorithms based on neural networks is increasingly feasible.

Bibliography

[1] J. Cong et al. “A state-of-charge estimation method of the power lithium-ion battery in complex conditions based on adaptive square root extended Kalman filter”. en. In: *Energy* 219 (2021), p. 119603. ISSN: 0360-5442. DOI: 10.1016/j.energy.2020.119603. URL: https://www.sciencedirect.com/science/article/pii/S0360544220327109 (visited on 10/08/2021).

[2] Enel. *What Is Electric Mobility and What Are Its Advantages?* 2021. URL: https://www.enel.pe/en/sustainability/what-is-electric-mobility-and-what-are-its-advantages.html.

[3] L. Liuyi and Ying Wei. “State-of-Charge and State-of-Health Estimation for Lithium-Ion Batteries Based on Dual Fractional-Order Extended Kalman Filter and Online Parameter Identification”. In: *IEEE Access* 9 (2021), pp. 47588–47602. DOI: 10.1109/ACCESS.2021.3068813.

[4] Electricity Map. *Electricitymap*. 2021. URL: https://app.electricitymap.org/map.

[5] Regione Emilia Romagna. *Il primo autobus elettrico parla bolognese*. it-IT. 2021. URL: https://ambiente.regione.emilia-romagna.it/it/notizie/attualita/2021/dicembre/il-primo-autobus-elettrico-parla-bolognese.

[6] Claudio Rossi et al. “A Hybrid–Electric Driveline for Agricultural Tractors Based on an e-CVT Power-Split Transmission”. In: *Energies* 14.21 (2021). ISSN:

1996-1073. DOI: 10.3390/en14216912. URL: https://www.mdpi.com/1996-1073/14/21/6912.

[7] Sumukh Surya, Vinicius Marcis, and Sheldon Williamson. “Core Temperature Estimation for a Lithium ion 18650 Cell”. en. In: *Energies* 14.1 (Jan. 2021). Number: 1 Publisher: Multidisciplinary Digital Publishing Institute, p. 87. DOI: 10.3390/en14010087. URL: https://www.mdpi.com/1996-1073/14/1/87 (visited on 11/05/2021).

[8] Wikipedia contributors. *Battery management system — Wikipedia, The Free Encyclopedia*. https://en.wikipedia.org/w/index.php?title=Battery_management_system&oldid=1059435663. [Online; accessed 4-January-2022]. 2021.

[9] Wikipedia contributors. *On-board diagnostics — Wikipedia, The Free Encyclopedia*. [Online; accessed 4-January-2022]. 2021. URL: https://en.wikipedia.org/w/index.php?title=On-board_diagnostics&oldid=1062735241.

[10] Kei Long Wong et al. “Li-Ion Batteries State-of-Charge Estimation Using Deep LSTM at Various Battery Specifications and Discharge Cycles”. In: *Proceedings of the Conference on Information Technology for Social Good*. GoodIT ’21. New York, NY, USA: Association for Computing Machinery, Sept. 2021, pp. 85–90. ISBN: 978-1-4503-8478-0. DOI: 10.1145/3462203.3475878. URL: https://doi.org/10.1145/3462203.3475878 (visited on 10/18/2021).

[11] Phillip Kollmeyer et al. *LG 18650HG2 Li-ion Battery Data and Example Deep Neural Network xEV SOC Estimator Script*. 2020. DOI: 10.17632/cp3473x7xv.3.

[12] Tyler Or et al. “Recycling of mixed cathode lithium-ion batteries for electric vehicles: Current status and future outlook”. en. In: *Carbon Energy* 2.1 (2020). _eprint: https://onlinelibrary.wiley.com/doi/pdf/10.1002/cey2.29, pp. 6–43. ISSN: 2637-9368. DOI: 10.1002/cey2.29. URL:

https://onlinelibrary.wiley.com/doi/abs/10.1002/cey2.29 (visited on 11/24/2021).

[13] Jinhyeong Park et al. “Integrated Approach Based on Dual Extended Kalman Filter and Multivariate Autoregressive Model for Predicting Battery Capacity Using Health Indicator and SOC/SOH”. en. In: *Energies* 13.9 (Jan. 2020). Number: 9 Publisher: Multidisciplinary Digital Publishing Institute, p. 2138. DOI: 10.3390/en13092138. URL: https://www.mdpi.com/1996-1073/13/9/2138 (visited on 01/10/2022).

[14] Claudio Rossi et al. “Simplified Parameters Estimation forthe Dual Polarization Model of Lithium-Ion Cell”. en. In: *ELECTRIMACS 2019*. Ed. by Walter Zamboni and Giovanni Petrone. Lecture Notes in Electrical Engineering. Cham: Springer International Publishing, 2020, pp. 129–144. ISBN: 978-3-030-56970-9. DOI: 10.1007/978-3-030-56970-9_11.

[15] Daoming Sun et al. “State of charge estimation for lithium-ion battery based on an intelligent adaptive unscented Kalman filter”. In: *International Journal of Energy Research* 44.14 (2020), pp. 11199–11218.

[16] Bryn Walton et al. *Electric vehicles Setting a course for 2030*. en-EN. 2020. URL: https://www2.deloitte.com/us/en/insights/focus/future-of-mobility/electric-vehicle-trends-2030.html.

[17] Rui Xiong. *Modeling Theory of Lithium-Ion Batteries*. en. Singapore: Springer, 2020, pp. 63–106. DOI: 10.1007/978-981-15-0248-4_3. URL: https://doi.org/10.1007/978-981-15-0248-4_3 (visited on 12/21/2021).

[18] Xiaosong Hu et al. “State estimation for advanced battery management: Key challenges and future trends”. In: *Renewable and Sustainable Energy Reviews* 114 (2019), p. 109334. ISSN: 1364-0321. DOI: https://doi.org/10.1016/j.rser.2019.109334. URL: https://www.sciencedirect.com/science/article/pii/S1364032119305428.

[19] R. Ramachandran, D. Ganeshaperumal, and B. Subathra. “Parameter Estimation of Battery Pack in EV using Extended Kalman Filters”. In: *2019 IEEE International Conference on Clean Energy and Energy Efficient Electronics Circuit for Sustainable Development (INCCES)*. 2019, pp. 1–5. DOI: 10.1109/INCCES47820.2019.9167740.

[20] Ruoqi Zhang et al. “A Novel Battery Management System Architecture Based on an Isolated Power/Data Multiplexing Transmission Bus”. In: *IEEE Transactions on Industrial Electronics* 66.8 (Aug. 2019). Conference Name: IEEE Transactions on Industrial Electronics, pp. 5979–5991. ISSN: 1557-9948. DOI: 10.1109/TIE.2018.2873143.

[21] Ephrem Chemali et al. “Long Short-Term Memory Networks for Accurate State-of-Charge Estimation of Li-ion Batteries”. In: *IEEE Transactions on Industrial Electronics* 65.8 (Aug. 2018). Conference Name: IEEE Transactions on Industrial Electronics, pp. 6730–6739. ISSN: 1557-9948. DOI: 10.1109/TIE.2017.2787586.

[22] Lin Chen et al. “A new state-of-health estimation method for lithium-ion batteries through the intrinsic relationship between ohmic internal resistance and capacity”. en. In: *Measurement* 116 (Feb. 2018), pp. 586–595. ISSN: 02632241. DOI: 10.1016/j.measurement.2017.11.016. URL: https://linkinghub.elsevier.com/retrieve/pii/S0263224117307248 (visited on 12/15/2021).

[23] Arijit Guha and Amit Patra. “State of Health Estimation of Lithium-Ion Batteries Using Capacity Fade and Internal Resistance Growth Models”. In: *IEEE Transactions on Transportation Electrification* 4.1 (Mar. 2018). Conference Name: IEEE Transactions on Transportation Electrification, pp. 135–146. ISSN: 2332-7782. DOI: 10.1109/TTE.2017.2776558.

[24] Arijit Guha and Amit Patra. “State of Health Estimation of Lithium-Ion Batteries Using Capacity Fade and Internal Resistance Growth Models”. In: *IEEE Transactions on Transportation Electrification* 4.1 (Mar. 2018). Conference Name:

IEEE Transactions on Transportation Electrification, pp. 135–146. ISSN: 2332-7782. DOI: 10.1109/TTE.2017.2776558.

[25] Jinhao Meng et al. “Overview of Lithium-Ion Battery Modeling Methods for State-of-Charge Estimation in Electrical Vehicles”. en. In: *Applied Sciences* 8.5 (May 2018). Number: 5 Publisher: Multidisciplinary Digital Publishing Institute, p. 659. DOI: 10.3390/app8050659. URL: https://www.mdpi.com/2076-3417/8/5/659 (visited on 11/18/2021).

[26] Nikolaos Wassiliadis et al. “Revisiting the dual extended Kalman filter for battery state-of-charge and state-of-health estimation: A use-case life cycle analysis”. en. In: *Journal of Energy Storage* 19 (Oct. 2018), pp. 73–87. ISSN: 2352-152X. DOI: 10.1016/j.est.2018.07.006. URL: https://www.sciencedirect.com/science/article/pii/S2352152X18301786 (visited on 01/10/2022).

[27] Shun Xiang et al. “Lithium-Ion Battery Online Rapid State-of-Power Estimation under Multiple Constraints”. en. In: *Energies* 11.2 (Feb. 2018). Number: 2 Publisher: Multidisciplinary Digital Publishing Institute, p. 283. DOI: 10.3390/en11020283. URL: https://www.mdpi.com/1996-1073/11/2/283 (visited on 12/03/2021).

[28] Fangfang Yang et al. “A study of the relationship between coulombic efficiency and capacity degradation of commercial lithium-ion batteries”. en. In: *Energy* 145 (Feb. 2018), pp. 486–495. ISSN: 0360-5442. DOI: 10.1016/j.energy.2017.12.144. URL: https://www.sciencedirect.com/science/article/pii/S0360544217321874 (visited on 12/17/2021).

[29] Farid Bahiraei, Amir Fartaj, and Gholam-Abbas Nazri. “Electrochemical-thermal Modeling to Evaluate Active Thermal Management of a Lithium-ion Battery Module”. en. In: *Electrochimica Acta* 254 (Nov. 2017), pp. 59–71. ISSN: 0013-4686. DOI: 10.1016/j.electacta.2017.09.084. URL: https:

//www.sciencedirect.com/science/article/pii/S0013468617319552 (visited on 12/13/2021).

[30] Zuchang Gao et al. “Integrated Equivalent Circuit and Thermal Model for Simulation of Temperature-Dependent LiFePO4 Battery in Actual Embedded Application”. en. In: *Energies* 10.1 (Jan. 2017). Number: 1 Publisher: Multidisciplinary Digital Publishing Institute, p. 85. DOI: 10.3390/en10010085. URL: https://www.mdpi.com/1996-1073/10/1/85 (visited on 11/05/2021).

[31] Günter Klambauer et al. “Self-Normalizing Neural Networks”. In: *Proceedings of the 31st International Conference on Neural Information Processing Systems*. NIPS’17. Long Beach, California, USA: Curran Associates Inc., 2017, pp. 972–981. ISBN: 9781510860964.

[32] W. Li et al. “State of Charge Estimation of Lithium-Ion Batteries Using a Discrete-Time Nonlinear Observer”. In: *IEEE Transactions on Industrial Electronics* 64.11 (2017), pp. 8557–8565. DOI: 10.1109/TIE.2017.2703685.

[33] Qian-Kun Wang et al. “A unified modeling framework for lithium-ion batteries: An artificial neural network based thermal coupled equivalent circuit model approach”. en. In: *Energy* 138 (Nov. 2017), pp. 118–132. ISSN: 0360-5442. DOI: 10.1016/j.energy.2017.07.035. URL: https://www.sciencedirect.com/science/article/pii/S0360544217312100 (visited on 11/05/2021).

[34] Quanqing Yu et al. “Lithium-Ion Battery Parameters and State-of-Charge Joint Estimation Based on H-Infinity and Unscented Kalman Filters”. In: *IEEE Transactions on Vehicular Technology* 66.10 (2017), pp. 8693–8701. DOI: 10.1109/TVT.2017.2709326.

[35] Christian Campestrini et al. “A comparative study and review of different Kalman filters by applying an enhanced validation method”. en. In: *Journal of Energy Storage* 8 (Nov. 2016), pp. 142–159. ISSN: 2352-152X. DOI: 10.1016/j.est.2016.10.004. URL: https:

//www.sciencedirect.com/science/article/pii/S2352152X16302031 (visited on 01/05/2022).

[36] Christian Campestrini et al. “A comparative study and review of different Kalman filters by applying an enhanced validation method”. In: *Journal of Energy Storage* 8 (2016), pp. 142–159. ISSN: 2352-152X. DOI: https://doi.org/10.1016/j.est.2016.10.004. URL: https://www.sciencedirect.com/science/article/pii/S2352152X16302031.

[37] Alexander Farmann and Dirk Uwe Sauer. “A comprehensive review of on-board State-of-Available-Power prediction techniques for lithium-ion batteries in electric vehicles”. en. In: *Journal of Power Sources* 329 (Oct. 2016), pp. 123–137. ISSN: 0378-7753. DOI: 10.1016/j.jpowsour.2016.08.031. URL: https://www.sciencedirect.com/science/article/pii/S0378775316310308 (visited on 12/13/2021).

[38] Christian Julien et al. *Lithium Batteries*. en. Cham: Springer International Publishing, 2016. DOI: 10.1007/978-3-319-19108-9. URL: http://link.springer.com/10.1007/978-3-319-19108-9 (visited on 11/15/2021).

[39] Kirill Murashko. *Thermal modelling of commercial lithium-ion batteries*. en. 2016, p. 137.

[40] Gregory L Plett. *Battery management systems, Volume II: Equivalent-circuit methods*. Norwood, MA: Artech House, 2016.

[41] François Chollet et al. *Keras*. https://keras.io. 2015.

[42] A. Damiano, C. Musio, and I. Marongiu. “Experimental validation of a dynamic energy model of a battery electric vehicle”. In: *2015 International Conference on Renewable Energy Research and Applications (ICRERA)*. 2015, pp. 803–808. DOI: 10.1109/ICRERA.2015.7418523.

[43] Zuchang Gao et al. “Lithium-ion battery modeling and validation for smart power system”. In: *2015 International Conference on Computer, Communications, and Control Technology (I4CT)*. Apr. 2015, pp. 269–274. DOI: 10.1109/I4CT.2015.7219579.

[44] Diederik P. Kingma and Jimmy Ba. “Adam: A Method for Stochastic Optimization”. In: *3rd International Conference on Learning Representations*. Ed. by Yoshua Bengio and Yann LeCun. San Diego: ICLR, 2015, pp. 1–15. URL: http://arxiv.org/abs/1412.6980.

[45] Joaquín Klee Barillas et al. “A comparative study and validation of state estimation algorithms for Li-ion batteries in battery management systems”. In: *Applied Energy* 155 (2015), pp. 455–462. ISSN: 0306-2619. DOI: https://doi.org/10.1016/j.apenergy.2015.05.102. URL: https://www.sciencedirect.com/science/article/pii/S0306261915007357.

[46] Gregory L Plett. *Battery Management Systems, Volume I: Battery Modeling*. Norwood, MA: Artech House, 2015.

[47] Kandler Smith, Ying Shi, and Shriram Santhanagopalan. “Degradation mechanisms and lifetime prediction for lithium-ion batteries — A control perspective”. In: *2015 American Control Conference (ACC)*. ISSN: 2378-5861. July 2015, pp. 728–730. DOI: 10.1109/ACC.2015.7170820.

[48] Johnny Wehbe and Nabil Karami. “Battery equivalent circuits and brief summary of components value determination of lithium ion: A review”. In: *2015 Third International Conference on Technological Advances in Electrical, Electronics and Computer Engineering (TAEECE)*. Apr. 2015, pp. 45–49. DOI: 10.1109/TAEECE.2015.7113598.

[49] Bizhong Xia et al. “State of Charge Estimation of Lithium-Ion Batteries Using an Adaptive Cubature Kalman Filter”. In: *Energies* 8.6 (2015), pp. 5916–5936. ISSN: 1996-1073. DOI: 10.3390/en8065916. URL: https://www.mdpi.com/1996-1073/8/6/5916.

[50] Hancheng Dong et al. “Lithium-ion battery state of health monitoring and remaining useful life prediction based on support vector regression-particle filter”. en. In: *Journal of Power Sources* 271 (Dec. 2014), pp. 114–123. ISSN: 0378-7753. DOI: 10.1016/j.jpowsour.2014.07.176. URL: https://www.sciencedirect.com/science/article/pii/S0378775314012324 (visited on 06/04/2021).

[51] Habiballah Rahimi-Eichi, Federico Baronti, and Mo-Yuen Chow. “Online Adaptive Parameter Identification and State-of-Charge Coestimation for Lithium-Polymer Battery Cells”. In: *IEEE Transactions on Industrial Electronics* 61.4 (Apr. 2014). Conference Name: IEEE Transactions on Industrial Electronics, pp. 2053–2061. ISSN: 1557-9948. DOI: 10.1109/TIE.2013.2263774.

[52] F. Baronti et al. “Experimental analysis of open-circuit voltage hysteresis in lithium-iron-phosphate batteries”. In: *IECON 2013 - 39th Annual Conference of the IEEE Industrial Electronics Society*. ISSN: 1553-572X. Nov. 2013, pp. 6728–6733. DOI: 10.1109/IECON.2013.6700246.

[53] Anthony Barré et al. “A review on lithium-ion battery ageing mechanisms and estimations for automotive applications”. en. In: *Journal of Power Sources* 241 (Nov. 2013), pp. 680–689. ISSN: 0378-7753. DOI: 10.1016/j.jpowsour.2013.05.040. URL: https://www.sciencedirect.com/science/article/pii/S0378775313008185 (visited on 12/14/2021).

[54] Robyn Jackey et al. “Battery Model Parameter Estimation Using a Layered Technique: An Example Using a Lithium Iron Phosphate Cell”. en. In: Apr. 2013, pp. 2013–01–1547. DOI: 10.4271/2013-01-1547. URL: https://www.sae.org/content/2013-01-1547/ (visited on 12/13/2021).

[55] Languang Lu et al. “A review on the key issues for lithium-ion battery management in electric vehicles”. en. In: *Journal of Power Sources* 226 (Mar. 2013), pp. 272–288. ISSN: 0378-7753. DOI: 10.1016/j.jpowsour.2012.10.060. URL: https:

//www.sciencedirect.com/science/article/pii/S0378775312016163 (visited on 11/17/2021).

[56] Wladislaw Waag, Christian Fleischer, and Dirk Uwe Sauer. "On-line estimation of lithium-ion battery impedance parameters using a novel varied-parameters approach". en. In: *Journal of Power Sources* 237 (Sept. 2013), pp. 260–269. ISSN: 03787753. DOI: 10.1016/j.jpowsour.2013.03.034. URL: https://linkinghub.elsevier.com/retrieve/pii/S0378775313004254 (visited on 12/22/2021).

[57] Georg Walder et al. "Functionality and Behaviour of an Dual Kalman Filter implemented on a Modular Battery-Management-System". en. In: (2013), p. 9.

[58] Xiaosong Hu, Shengbo Li, and Huei Peng. "A comparative study of equivalent circuit models for Li-ion batteries". en. In: *Journal of Power Sources* 198 (Jan. 2012), pp. 359–367. ISSN: 0378-7753. DOI: 10.1016/j.jpowsour.2011.10.013. URL: https://www.sciencedirect.com/science/article/pii/S0378775311019628 (visited on 12/03/2021).

[59] H. Rahimi-Eichi, F. Baronti, and M.-Y. Chow. "Modeling and online parameter identification of Li-Polymer battery cells for SOC estimation". In: *2012 IEEE International Symposium on Industrial Electronics*. ISSN: 2163-5145. May 2012, pp. 1336–1341. DOI: 10.1109/ISIE.2012.6237284.

[60] Karthik Somasundaram, Erik Birgersson, and Arun Sadashiv Mujumdar. "Thermal–electrochemical model for passive thermal management of a spiral-wound lithium-ion battery". en. In: *Journal of Power Sources* 203 (Apr. 2012), pp. 84–96. ISSN: 0378-7753. DOI: 10.1016/j.jpowsour.2011.11.075. URL: https://www.sciencedirect.com/science/article/pii/S0378775311023639 (visited on 12/13/2021).

[61] Gregory L. Plett. "Recursive approximate weighted total least squares estimation of battery cell total capacity". en. In: *Journal of Power Sources* 196.4 (Feb. 2011),

pp. 2319–2331. ISSN: 0378-7753. DOI: 10.1016/j.jpowsour.2010.09.048. URL: https://www.sciencedirect.com/science/article/pii/S037877531001654X (visited on 01/05/2022).

[62] Jürgen Remmlinger et al. “State-of-health monitoring of lithium-ion batteries in electric vehicles by on-board internal resistance estimation”. en. In: *Journal of Power Sources*. Selected papers presented at the 12th Ulm ElectroChemical Talks (UECT):2015 Technologies on Batteries and Fuel Cells 196.12 (June 2011), pp. 5357–5363. ISSN: 0378-7753. DOI: 10.1016/j.jpowsour.2010.08.035. URL: https://www.sciencedirect.com/science/article/pii/S0378775310013534 (visited on 12/13/2021).

[63] Davide Andrea. *Battery management systems for large lithium-ion battery packs*. en. Boston: Artech House, 2010. ISBN: 978-1-60807-104-3.

[64] F. Baronti et al. “Enhanced model for Lithium-Polymer cells including temperature effects”. In: *IECON 2010 - 36th Annual Conference on IEEE Industrial Electronics Society*. ISSN: 1553-572X. Nov. 2010, pp. 2329–2333. DOI: 10.1109/IECON.2010.5675134.

[65] Christophe Forgez et al. “Thermal modeling of a cylindrical LiFePO4/graphite lithium-ion battery”. en. In: *Journal of Power Sources* 195.9 (May 2010), pp. 2961–2968. ISSN: 0378-7753. DOI: 10.1016/j.jpowsour.2009.10.105. URL: https://www.sciencedirect.com/science/article/pii/S037877530901982X (visited on 11/05/2021).

[66] A. J. Smith, J. C. Burns, and J. R. Dahn. “A High Precision Study of the Coulombic Efficiency of Li-Ion Batteries”. en. In: *Electrochemical and Solid-State Letters* 13.12 (Sept. 2010). Publisher: IOP Publishing, A177. ISSN: 1944-8775. DOI: 10.1149/1.3487637. URL: https://iopscience-iop-

org.ezproxy.unibo.it/article/10.1149/1.3487637/meta (visited on 12/17/2021).

[67] O. Erdinc, B. Vural, and M. Uzunoglu. “A dynamic lithium-ion battery model considering the effects of temperature and capacity fading”. In: *2009 International Conference on Clean Electrical Power*. June 2009, pp. 383–386. DOI: 10.1109/ICCEP.2009.5212025.

[68] Martin Coleman, William Gerard Hurley, and Chin Kwan Lee. “An Improved Battery Characterization Method Using a Two-Pulse Load Test”. In: *IEEE Transactions on Energy Conversion* 23.2 (June 2008). Conference Name: IEEE Transactions on Energy Conversion, pp. 708–713. ISSN: 1558-0059. DOI: 10.1109/TEC.2007.914329.

[69] Fei Zhang, Guangjun Liu, and Lijin Fang. “A battery State of Charge estimation method with extended Kalman filter”. In: *2008 IEEE/ASME International Conference on Advanced Intelligent Mechatronics*. 2008, pp. 1008–1013. DOI: 10.1109/AIM.2008.4601799.

[70] Min Chen and G.A. Rincon-Mora. “Accurate electrical battery model capable of predicting runtime and I-V performance”. In: *IEEE Transactions on Energy Conversion* 21.2 (June 2006). Conference Name: IEEE Transactions on Energy Conversion, pp. 504–511. ISSN: 1558-0059. DOI: 10.1109/TEC.2006.874229.

[71] Gregory L. Plett. “Extended Kalman filtering for battery management systems of LiPB-based HEV battery packs Part 1. Background”. In: *Journal of Power Sources* 134.2 (2004), pp. 252–261. ISSN: 0378-7753. DOI: https://doi.org/10.1016/j.jpowsour.2004.02.031.

[72] Gregory L. Plett. “Extended Kalman filtering for battery management systems of LiPB-based HEV battery packs: Part 2. Modeling and identification”. In: *Journal of Power Sources* 134.2 (2004), pp. 262–276. ISSN: 0378-7753. DOI: https://doi.org/10.1016/j.jpowsour.2004.02.032. URL: https://www.sciencedirect.com/science/article/pii/S037877530400360X.

[73] Gregory L. Plett. “Extended Kalman filtering for battery management systems of LiPB-based HEV battery packs: Part 3. State and parameter estimation”. In: *Journal of Power Sources* 134.2 (2004), pp. 277–292. ISSN: 0378-7753. DOI: https://doi.org/10.1016/j.jpowsour.2004.02.033. URL: https://www.sciencedirect.com/science/article/pii/S0378775304003611.

[74] A.H. Zimmerman. “Self-discharge losses in lithium-ion cells”. In: *IEEE Aerospace and Electronic Systems Magazine* 19.2 (Feb. 2004). Conference Name: IEEE Aerospace and Electronic Systems Magazine, pp. 19–24. ISSN: 1557-959X. DOI: 10.1109/MAES.2004.1269687.

[75] Lijun Gao, Shengyi Liu, and R.A. Dougal. “Dynamic lithium-ion battery model for system simulation”. In: *IEEE Transactions on Components and Packaging Technologies* 25.3 (Sept. 2002). Conference Name: IEEE Transactions on Components and Packaging Technologies, pp. 495–505. ISSN: 1557-9972. DOI: 10.1109/TCAPT.2002.803653.

[76] I Bloom et al. “An accelerated calendar and cycle life study of Li-ion cells”. en. In: *Journal of Power Sources* 101.2 (Oct. 2001), pp. 238–247. ISSN: 0378-7753. DOI: 10.1016/S0378-7753(01)00783-2. URL: https://www.sciencedirect.com/science/article/pii/S0378775301007832 (visited on 01/12/2022).

[77] Simon Haykin. *KALMAN FILTERING AND NEURAL NETWORKS*. New York, NYC : Wiley, 2001.

[78] Peter J. Huber. “Robust Estimation of a Location Parameter”. In: *Breakthroughs in Statistics: Methodology and Distribution*. New York, NY: Springer New York, 1992, pp. 492–518. ISBN: 978-1-4612-4380-9. DOI: 10.1007/978-1-4612-4380-9_35. URL: https://doi.org/10.1007/978-1-4612-4380-9_35.

[79] R. E. Kalman. “A New Approach to Linear Filtering and Prediction Problems”. In: *Journal of Basic Engineering* 82.1 (Mar. 1960), pp. 35–45. ISSN: 0021-9223. DOI: 10.1115/1.3662552. URL: https://doi.org/10.1115/1.3662552.